Global Optimization Studies in Clusters

Dissertation
zur Erlangung des Grades
des Doktors der Naturwissenschaften
der Naturwissenschaftlich-Technischen Fakultät III
Chemie, Pharmazie, Bio- und Werkstoffwissenschaften
der Universität des Saarlandes

von

Stephan Kohaut

Saarbrücken
2017

Tag des Kolloquiums:	31.03.2017
Dekan:	Prof. Dr. G.Kickelbick
Berichterstatter:	Prof. Dr. M. Springborg
	Prof. Dr. H.P. Beck
Vorsitz:	Prof. Dr. G. Jung
Akad. Mitarbeiter:	Dr. R. Haberkorn

Contents

1 Acknowledgements **3**

2 Kurzzusammenfassung **4**

3 Abstract **5**

4 Preface **6**

5 Introduction **6**

5.1 Clusters 11

5.2 Nanoalloys 11

I Global Optimization **13**

6 The Global Optimization Problem **14**

6.1 Introduction 14

6.2 Evolutionary Algorithms 14

7 Implementation of a genetic algorithm **19**

7.1 Local relaxations 20

7.2 Start routine 20

7.3 Crossover routine 21

7.4 Mutation routine 21

7.5 Selection routine 22

7.6 Convergence 22

8 Testing the implemented genetic algorithm **23**

8.1 The Lennard-Jones Potential 23

II Total-Energy Methods **25**

9 Theoretical models **26**

10 The Born-Oppenheimer Approximation **26**

11 Density functional theory **28**

11.1 The Theorems of Hohenberg and Kohn 28

11.2 The Kohn-Sham equations 29

11.3 The exchange-correlation Problem 31
11.3.1 The Local Density Approximation LDA 31

12 Density functional tight-binding **33**
12.1 The tight-binding approximation 35
12.2 Parametrization of the DFTB method 36

13 The RGL potential **38**
13.1 Parametrization of the RGL parameters 39

References **43**

III Results and Discussion 55

14 Summary **110**

List of Publications **113**

1 Acknowledgements

This work would not have been possible without the help of several people. First I would like to express my deepest gratefulness to my supervisor, Prof. Dr. Michael Springborg for his guidance and support throughout my time at his group in Saarbrücken. I want to thank him that his door was always open, not only in the case of scientific related questions, but also for any non-scientific problems that i had to solve. I am also thankful that i was allowed to have a view to the left and to the right along my scientific path and whenever i got lost he led me back and showed me the way.

I would also like to acknowledge the help of Dr. Valeri G. Grygorian, not only for his support, but also for many fruitful discussions that we had together about anything related to clusters and global optimization procedures in general. To Dr. Mohammad Molayem, i want to say thank you for an endless number of scientific and non-scientific discussions and for giving me the oppurtunity to learn how a physicist sees the world.

I am also thankful to Philipp Thiel for his help in solving various mathematical problems that i had to face during my time in Saarbrücken and especially for his help with the similarity code.

Another thank you goes to Dr. Yi Dong for various fruitful discussions, several lessons she gave me about tea and especially for her support during our visit to Shanghai.

I want to thank my colleagues Jihene, Yong, Kai and ChenChen for a pleasant work atmosphere and for lots of interesting discussions. I am grateful to Silvia Nagel for her help with lots of administrative things. To Prof. Dr. Horst P. Beck i would like to express my appreciation for several interesting discussions and his explanations regarding all sorts of crystallographic problems. I am also thankful to Svenja Meyer for the proof-reading of this thesis. I want to thank Anne Clasen for helping me to organize a lot of things, especially at the end of my time in Saarbrücken. I want to thank Isabel Filbrich for lots of funny and interesting coffee breaks that often cheered up my day.

Then there are some persons left: A big thank you goes to our administrator Nicolas Louis who did and still does a nice job and who was available almost 24 hours and seven days per week to help me with several computational problems.

For many hours of coffee and tea tasting, many cheerful words and for the great time we spent together i want to say thank you to Jonas Sander. I would like to express my deepest gratitude to Dr. Nathalie Kunkel for her endless and continuing support in my life, in and outside of the academic world. At last i want to thank my family for their support and encouragement over all the years.

2 Kurzzusammenfassung

Die vorliegende Arbeit untersucht das Wachstum von kleinen bis mittelgroßen Metall- und Halbleiterclustern. Kandidaten für globale Minima wurden mit einem genetischen Algorithmus optimiert und mit Dichtefunktionalmethoden untersucht. Cadmium Cluster mit bis zu 60 Atomen bilden unverzerrte, symmetrische Cluster mit einem Strukturmotiv, das als "Leary-Tetraeder" bekannt ist. Relative Stabilitäten ergeben sich aus geometrischen Effekten und dem Schließen von Elektronenschalen. Die Bindungsverhältnisse sind ähnlich zum Bulk. Anschließend wurde das Wachstum von Silizium-Germanium Cluster mit bis zu 30 Atomen untersucht. Relative Stabilitäten der Cluster hängen von deren Form und Zusammensetzung ab. Die stabilsten Cluster sind länglich und besitzen einen mittleren Siliziumgehalt von 32 Atom-%. Gemischte Cluster besitzen keine strukturelle Ähnlichkeit mit reinen Clustern und deren Segregationstyp ist von der Zusammensetzung abhängig. Es konnte kein Zusammenhang zwischen strukturellen und elektronischen Eigenschaften gefunden werden. Zuletzt wurden strukturelle und magnetische Eigenschaften von $AgRh_{n-1}$ und $Ag_{n-1}Rh$ Clustern mit einer Größe bis zu 20 Atomen untersucht. In den polyikosaedrischen Clustern $Ag_{n-1}Rh$ besetzt ein Rhodiumatom eine Position im Clusterinneren. Im umgekehrten Fall migriert das Silberatom an die Oberfläche. Lokale magnetischen Momente in den $Ag_{n-1}Rh$ Clustern sind auf dem Rhodiumatom lokalisiert und von dessen Koordinationszahl abhängig. In rhodiumreichen Clustern trägt ein einzelnes Silberatom nicht zum Gesamt-magnetischen Moment bei.

3 Abstract

In this work, we have studied the growth of several cluster systems including metallic and semiconductor clusters with our genetic algorithm coupled to the density functional tight-binding method followed by a re-optimization with density functional theory methods. Cadmium clusters with sizes up to 60 atoms form undistorted and symmetric clusters with a structural motif known as "Leary-Tetrahedron". Their stabilities correlate with their atomic configuration and the closing of electronic shells at certain sizes while their chemical bonds are quite similar to hcp-cadmium. Afterwards we studied the growth of mixed Si-Ge clusters with up to 30 atoms. The most stable clusters were found to be prolate with an average silicon content of 32-atom%. We found no structural similarities between pure and mixed clusters and the type of segregation depends on their individual composition. A correlation analysis showed no simple relations between structural features and electronic properties. At last we studied structural and magnetic properties of mixed $AgRh_{n-1}$ and $Ag_{n-1}Rh$ clusters with up to 20 atoms. Rhodium atoms within the polyicosahedral clusters were found to occupy positions in the center of the clusters. On the other side a silver atom migrates to the surface of rhodium-rich clusters. Local magnetic moments in the $Ag_{n-1}Rh$ clusters are mainly localized on the single rhodium atom and depend upon its coordination number. A single foreign silver atom in rhodium clusters on the other side does not contribute to the total magnetic moment.

4 Preface

The work described in this thesis was published in three articles that can be found in part III under Results and Discussion. The genetic algorithm for the global optimizations in all of the three publications was implemented in Python2.6 by S. Kohaut and attached to the Atomic Simulation Environment (ASE) [1]. Parallelization of the genetic algorithm was achieved by using the ParallelPython program [2]. All of the used DFTB parametrizations (Cd, Ag, Rh, Si and Ge) have been created and adapted by S. Kohaut to work with the Hotbit program [3]. The program (ASAP3) for the calculation of the total energies at the RGL level was downloaded from [4] and the fits for the potential were created with the help of several optimization routines as found in python-numpy [5]. Calculation of the similarity indices were done with a fortran program that was written by P. Thiel. All numerical basis sets and pseudopotentials for Ag, Rh, Si and Ge were created by S. Kohaut and tested to work with the Siesta program [6]. Structural analyses with the bond-angle analyses method were done with the ovito program [7, 8].

5 Introduction

Clusters form are a special field of chemistry and physics in between molecules and crystals. As a consequence of their finite size, their properties are often unpredictable and completely different to the same material in the bulk size regime. However up to now, there is no final consensus on the question whether a given material belongs to the class of the so-called nanomaterials or not. Nanoscience typically deals with materials with sizes of a few atoms to thousands of atoms with dimensions between 1nm and 100nm, depending on the material under investigation. They behave not like simple cuts from a macroscopic crystal but represent a class on their own, where the specific properties show an explicit dependence upon size, morphology and composition. In a macroscopic crystal the free Gibbs energy G is defined as the sum of a volume-based energy contribution and a term that arises due to the presence of the surface.

$$G = NG^V + A\gamma^S \tag{1}$$

with N being the number of atoms, the bulk free energy G_V, the surface area A and the specific surface energy γ^s. As most of the atoms for a cluster are on the surface, the contribution of the second term will dominate the total energy and the shapes and morphologies that the cluster adopts for a given size leading to structures that are unknown or uncommon for crystals (e.g. icosahedral or decahedral structures in metal clusters).

Beside the effects caused by the large surface-area-to-volume ratio, the quantum confinement effects are the second characteristic feature of nano-sized objects. An impressive illustration of the effect of a spatial confinement on the optical properties is realized in the semi-conductor nanoclusters of CdSe and CdTe [9] (also known as quantum dots). When the size of the quantum dot drops below the natural length of the electron-hole pair (the exciton bohr radius), the wavefunctions of both, the electron and the hole will be confined due to the walls of the particle. A confinement then induces a quantization in such a way that the electronic bands from the bulk will be transformed to discrete electronic states. Electronic excitations in the quantum dot are consequently a function of the size and noticeably blue-shifted in smaller sized dots. This is qualitatively in agreement with the results that one obtains from solving the Schrödinger equation for the particle-in-a-spherical-well example where there is an indirect relation found between the length of the box and the gaps between the energy levels. The fact that materials can nowadays be manipulated at the nano scale to get tailor-made properties has lead to an enormous number of applications of such particles ranging from medicinal [10, 11] to optical [12] usages, to applications in renewable energy [13] and especially in the field of catalysis [14]. In all these cases it is necessary to study the structures and growth patterns to understand the correlation between morphology, size and the resulting properties. However, it is often very difficult to obtain exact information about the structures and morphologies as well as their relation to their size. Especially in case of the prediction of an unknown structural type, theoretical simulations are an invaluable tool to back up experimental procedures in which the synthesis, the characterization or a screening for special properties are too laborious. Therefore, this work focuses on the identification of the growth patterns in three different cluster systems that were previously unknown. This work is carried through with the help of a global optimization procedure and various potentials that have earlier been checked for reliability in the description of the studied systems.

This thesis is organized as follows: Part I deals with the global optimization problem in cluster science and gives details about the implemented evolutionary based algorithm. It also includes results of the global optimization of several sizes on the Lennard-Jones potential energy surface to demonstrate that the implementation works correctly. The second part provides an introduction to the theoretical models that have been used during this work, starting with the density functional theory and followed by two semiempirical methods, the RGL and the density functional tight-binding method (DFTB). It is explained how the two semiempirical methods that were used have been parametrized and fitted to reproduce structural and mechanic properties in various bulk phases (in the case of the RGL potential) and clusters (for DFTB). The third part presents the obtained results from the global optimizations and characterizations in different systems including

pure and mixed metal clusters (Cd, Rh, Ag and mixed Ag-Rh clusters) and pure and mixed semiconductor structures (Si, Ge and mixed SiGe clusters).

In the first section, we propose a new growth pattern in small to medium sized cadmium clusters with up to 60 atoms and compare it to the former route that was not able to satisfyingly explain the few experimental results. Earlier studies predicted disordered clusters of decahedral symmetry to be the putative global minimum energy structures [15] which however could not explain the abundance spectra in mass spectroscopic measurements. Therefore we parametrized the density functional tight-binding approach and coupled it to a genetic algorithm to get the putative global minimum energy structures for a subsequent re-optimization with ab-initio density functional theory methods (DFT). In addition we also re-optimized those clusters with DFT that were proposed by Doye *et al.* from a combination of the semi empirical Gupta potential and the Basin-Hopping algorithm of Wales and Doye [16]. To analyze structural changes as a function of size we calculated a similarity index to identify possible similarities between clusters during the growth and used the bond-angle analysis method from Ackland *et al.* [17] that classifies atoms according to structural motifs that are known from the bulk (e.g. fcc, hcp, bcc,..). We also studied the evolution of the electronic properties during the growth process and compared the calculated HOMO-LUMO gaps with the so-called Kubo-criterion to check for a possible metallic behavior of small to medium sized cadmium clusters. Finally we tried to relate our calculated cluster stabilities to experimental results and results from a spherical jellium model to explain why clusters of some sizes are more stable than others.

The second section analyses the influence of the composition on the stability and electronic properties of mixed silicon-germanium clusters. All putative global minimum energy structures for all compositions Si_nGe_m with $n+m \leq 30$ have been optimized with our genetic algorithm in combination with the DFTB method and were later re-optimized with DFT methods to address several questions that have not been investigated earlier. For the DFT optimizations we optimized and tested for both elements a pseudopotential in combination with a polarized pseudo-numerical basis set of double-zeta quality in several bulk and cluster structures. Earlier it was shown by other authors [18] that for pure clusters of both elements it gets difficult to identify the correct structural ground state in an experiment as several clusters are energetically very close and all of them will compete for the global minimum on the potential energy surface; therefore we used a method known from polymer chemistry to characterize the shapes of all clusters as it is possible to measure this attribute by an analysis of the ion-mobilities [19]. We then compare these shapes and the structural similarities of the mixed clusters with the pure clusters of equal size to study the influence of the composition and the size on the growth process. These two properties are of special interest as silicon and germanium do not follow the same

growth pattern. While experimental studies proved that silicon clusters become spherical already at smaller sizes, the same behavior was not reported for germanium clusters which were essentially prolate up to around 60 atoms. Thus, it also makes sense to study which element dominates the structural property as this may influence the electronic properties. Possible demixing effects are analyzed by using two descriptors that will give information about the type of segregation in mixed silicon-germanium clusters. Based on earlier studies in mixed clusters with sizes up to 44 atoms that proved a tendency for silicon to occupy higher coordinated sites we could expect the formation of a core-shell system [20]. However the authors in this study fixed the Si:Ge ratio to 1 which does therefore not allow for a detailed analysis of the type of segregation in dependence of the composition. The bond order and the average radial distances of the silicon to the germanium atoms were then used to do an in-depth analysis of the segregation process for all compositions and sizes. To look for the most stable and unstable clusters we used two stability criteria and compared the outcome of both. The first criterion, the excess energy was biased as it traces the stability of each cluster back to the stability of the pure clusters whereas the second criterion was unbiased and would give the relative stabilities without any relation to the bulk or the pure clusters. We then considered mixed clusters highly stable or unstable if both criteria for stability or instability predicted the same outcome for a given size and composition. At last we searched for correlations between the electronic properties, namely the HOMO-LUMO gaps and the energies of the HOMO's and the LUMO's to several structural descriptors including the shape, the effective coordination numbers, the average bond lengths for the two species and the composition by calculating the Pearson correlation coefficient from the corresponding covariance matrix.

The third section discusses the effect of a single foreign atom on the structures and electronic properties of pure silver and rhodium clusters. The two metals show completely different growth mechanisms and whereas silver tends to form compact structures, often with an icosahedral shape [21, 22, 23], rhodium clusters were predicted to form simple cubes up to a size of at least 27 atoms [24, 25, 26, 27, 28]. Both metals are almost immiscible with a positive heat of formation over the whole composition range [29]. The Ag-Rh system also behaves differently to the Ag-Pd system, which is well studied and for which it was found that both elements will readily form alloys [30, 31]. However it is also known from other silver containing clusters that stable nanoalloys can be formed if there are other reasons for an enhanced stability of those, e.g. the formation of a core-shell system with the element with the greater binding energy/atom in the core and the other element with the lower overall specific surface energy at the surface. The smaller atoms will also occupy the higher coordinated sites within the core to minimize strain effects, typical examples are Ag-Ni [32, 33], Ag-Cu [34] and Ag-Co [35]. To study the effects of a

single foreign atom on the structures of silver and rhodium clusters we used our genetic algorithm in combination with the RGL potential and the DFTB method to identify the global minimum energy structures for the pure clusters and the mixed clusters with a single rhodium or silver atom as a dopant. To this end, we fitted the RGL potential to reproduce several structural and elastic properties in hypothetical Ag-Rh alloys in comparison to ab-inito DFT calculations as there are no experimentally known alloys. The DFTB method was parametrized to reproduce the structural properties from DFT calculations that were reported by other authors for small rhodium and silver clusters. As there were also no pseudopotentials and no numerical basis sets available with the desired accuracy we optimized them for both elements and tested them to work in the bulk and for smaller Ag and Rh clusters. All clusters were subsequently re-optimized with DFT methods and the optimized basis sets after the global optimization process. To verify the validity of our approach we first analysed the structural properties, the binding energy/atom and the magnetic moments/atom for every cluster up to a size of 20 atoms and compared the results with available results from experiments and other theoretical studies [24, 25, 36, 37, 38, 39]. Silver atoms are in general slightly larger than their rhodium counterparts and in combination with a much larger cohesive energy/atom in the bulk for fcc rhodium we expect that a core shell system will form for silver clusters that contain a single rhodium atom. Such an effect was also reported by other authors in the bulk, where a rhodium atom tends to migrate away from a (111) Ag-surface [40]. We used the simple Lennard-Jones pair potential to predict if the formation of such a core-shell system can be explained solely on the basis of the different atomic sizes. For rhodium-rich clusters on the other side we then expected a migration of a silver atom to the surface of the clusters and we studied if a single silver atom can be incorporated into a given structural motif (the cube-based rhodium clusters) to replace a rhodium atom. Cluster stabilities as a function of the composition and the size have been studied using two approaches that have already been mentioned in the case of mixed Si-Ge clusters. Doping of silver or rhodium clusters with a single foreign atom of the other kind will also have an effect on the magnetic properties of each cluster. In other systems it was shown that silver could do both, a quenching of the total magnetic moment (Ag_nCo)[41] or contribute to it (Ag_nNi) [33]. Thus, we also studied the evolution of the magnetic moment in singly doped silver and rhodium clusters with their size as the effective coordination number of the involved atoms may play a role like it was observed in Ag_nFe [42]. For that purpose we studied the results of Mulliken population analyses and calculated differences in the spin densities for electrons with opposing spins for all studied mixed clusters. Both approaches will then allow it to make predictions on which atoms the magnetic moments are localized within a given cluster. At last we discuss possible reasons for a ferromagnetic

contribution of silver atoms to the total magnetic moment by an analysis of the calculated density of states and partial density of states.

5.1 Clusters

Since ancient times clusters have been used by humans to create effects in materials that have otherwise not been possible with other methods during that time. Among the first methods where nanoclusters played an important role was the coloring of silicate glasses due to incorporated gold clusters. The typical red-colored glasses are the result of an excitation of a collective oscillation of gold valence electrons (so-called surface plasmons)[43]. Nowadays a large toolbox of methods are known to synthesize clusters in solution and gas phase, depending on the type of the material. Metal clusters, especially of metals that are immiscible in bulk (e.g. Ag-Rh or Pd-Rh), are synthesized by co-precipitation in solution [44] or microwave-based methods [45], whereas mono-metallic clusters can be obtained from laser evaporation or ion sputtering sources [46, 47]. Analyses of the sizes and stabilities of the synthesized clusters are typically done with mass spectroscopic methods. However, these methods do not give structural information for a given size. Optical spectroscopy or diffraction based methods [23, 48, 49] are coupled to a mass spectrometer to study the corresponding structures then. For systems with a very flat potential energy surface (e.g. Si, Ge and mixed Si-Ge clusters that were also studied in this thesis) this may be not possible, but even then ion mobility measurements could give information about the shapes of the synthesized clusters [19]. Whenever additional flexibility is needed to tune the properties of clusters to get a specific effect (e.g. in catalysis) then a second, different type of atom can be added to a given cluster system. In addition such nanoalloys may also display behaviors that are unknown from macroscopic alloys e.g. miscibility at nanosize of two elements that are otherwise immiscible [47].

5.2 Nanoalloys

Addition of a second, different type of atom to an existing mono-elemental cluster adds additional complexity to the global optimization problem. Homotops are clusters with the same size, same configuration and same composition, but with different occupations of the positions within the structure. The number of homotops $P_{m,n}$ for an A_mB_n cluster is given by

$$P_{m,n} = \frac{(n+m)!}{n!m!} \tag{2}$$

To tackle the homotop problem, a permutation operator is typically added to the

mutation routine in a genetic algorithm. However, especially in the case of a flat potential energy surface with very small differences in the total energy between different homotops, it remains difficult to obtain the correct global minimum energy structure. An additional problem consists in the identification of the correct type of segregation within a given nanoalloy. Figure 1 shows the different types of segregation that can occur in a nanoalloyed cluster. The type of segregation depends on several factors and is an interplay between the specific surface and interface energies, the binding energies in the bulk of the pure elements, the binding energies and the size-ratio between different types of atoms [50]. In addition to all other other factors it was shown by Hume-Rothery that a lattice mismatch of about 15% alone makes it unfavorable for two elements to form an alloy in the bulk, simply because of geometric considerations. A positive heat of formation and mixing enthalpy indicates that such an alloy is not formed from the pure clusters. However, if the size of these alloys is reduced to the nano-size regime, different rules apply and a negative heat of formation and mixing enthalpy compared to the pure clusters of equal size can be found. Typical examples for such a behavior occur for silver alloys where negative mixing enthalpies were predicted for example for the pairs Ag-Ni [32] and Ag-Cu [34]. Whereas these two first examples are clearly influenced by the different ratios of the atomic sizes between silver and its alloying partner, it is more complicated for the Ag-Rh case where there is only a small difference between the size of the atoms. Large differences in the sizes will lead to a core-shell system where the smaller atoms are found in the center of the cluster to minimize the geometric strain. A larger cohesive energy in one of the involved elemental crystals is an additional driving force to form a core-shell system as these atoms tend to maximize the number of bonds to atoms of the same kind, which is best realized in the core of the cluster. This will generally lead to a polyicosahedral, decahedral or cuboctahedral growth and an enhanced stability of the clusters at certain sizes. These so called magic sizes are related to a beneficial closing of geometrical shells in closed packed structures and can be found for icosahedral clusters with k concentric shells at sizes N equal to [51]

$$N(k) = \frac{10}{3}k^3 + 5k^2 + \frac{11}{3}k - 1. \tag{3}$$

Clusters with non-truncated decahedral motifs are in general less stable compared to the icosahedral ones as their surface area is much larger. Geometric shell closing in decahedral clusters are seen for sizes with N atoms at (again, k is an integer)

$$N(k) = \frac{5}{6}k^3 + \frac{1}{6}k. \tag{4}$$

However, truncation will make the cluster more spherical and indeed in the case of silver

such a truncated decahedron was reported to be the global minimum in silver clusters for $N = 75$ [52]. Highly symmetric and closed packed clusters with other symmetry elements rather than a fivefold axis can be realized in the form of an octahedron with shell closing at size N at

$$N(k) = \frac{2}{3}k^3 + \frac{1}{3}k. \tag{5}$$

This structural motif that can be derived from an fcc-packing of hard spheres does not only occur in Lennard-Jones clusters [53], but has also been found in several other transition metal clusters [54].

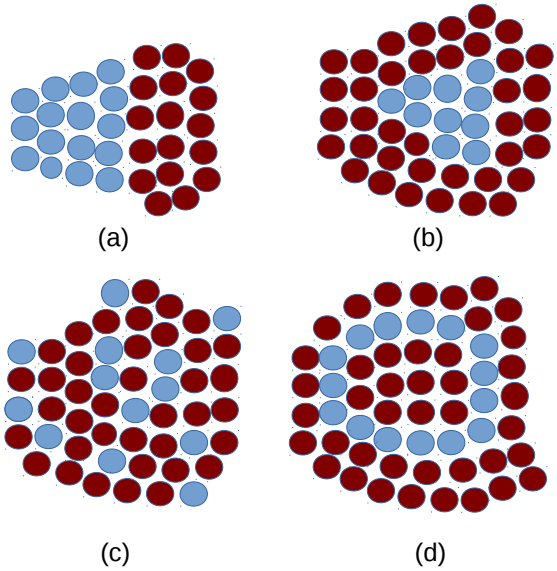

Figure 1: Different types of segregation that can be found in a nanoalloyed cluster. (a) Janus-like (b) core-shell (c) mixed (d) onion-like.

Enhanced stability can also result from the closing of electronic shells. This effect can be seen in calculations on the spherical jellium model (=homogeneous positive background charges from the nuclei plus the core electrons) assuming an infinite deep spherical or harmonical well as the potential in which the electrons move. Clusters with magic sizes with greater stability compared to neighbouring sizes are then found for structures with $n = 2, 8, 20, 40, 70, 92, ...$ electrons. However, the reason for enhanced stability is often a mixture of both, a beneficial geometric arrangement of the atoms, and the closing of electronic shells at certain sizes. Which aspect then finally determines the stability and shape is non-trivial to answer and depends always on the system under investigation.

Part I
Global Optimization

6 The Global Optimization Problem

6.1 Introduction

The problem of identifying a global extremum on a complicated multidimensional function space is not trivial and due to the fact that the whole function space is unknown, there is also no proof that a found extremum is indeed a global minimum or maximum. A typical issue in chemistry where such problems occur is the identification for the most stable configuration of a given number and type of atoms in space. The complexity of the potential energy surface (pes) whose dimensionality grows exponentially with the number of atoms making it impossible to calculate all points on the pes even with the most powerful computers available today. Restricting the search space on the pes to structures that follow certain rules, one may for instance identify 217 structures that obey the octet rule for the sum formula C_6H_6 [55]. The hyperspace in such a small system with twelve atoms has already a dimensionality of 3N-6 = 30 making it a laborious task to identify the most stable configuration without prior limitation of the search space. Several algorithms have been proposed to effectively locate isomers on a pes with most of them mimic principles inherent to processes in nature [56, 57, 58]. Essential to the success of all these algorithms is their ability to leave local minima and efficiently jump over barriers to sample the pes and eventually end up in the global minimum of the function space. Two of the most popular and successful variants are Basin-hopping, introduced by Wales et al. [16] and the larger class of evolutionary algorithms that were first proposed by Deaven and Ho [59] to tackle the problem of the C_{60} pes. In the vast majority of cases, the pes is calculated by a classical force-field or a semi-empirical method, although several publications used a first-principles approach like Hartree-Fock or Density functional theory, for an overview see [60].

6.2 Evolutionary Algorithms

Evolutionary algorithms used in cluster chemistry adopt principles from nature to identify optimal solutions for unknown cluster structures. As well as in nature, where the phenotype of each individual is encoded in its genome and consequently determines its properties, the configuration of the atoms in a cluster has to be translated into some kind

of genetic information. Deaven and Ho [59] proposed to use the position of each atom in the 3-dimensional space directly as a genome instead of encoding genetic information in a binary string. Genetic information between individuals can then be exchanged by a "cut-and-splice" operation similar to the recombination process known from reproduction biology. Such a cut can be defined by a random plane that intersects two parts of a cluster to provide two halves that are available for a following crossover process. The recombination procedure is done by combining the two pieces in such a way that the atoms of each part can interact, typically at a distance close to the bond length of the involved atoms followed by a local relaxation as it can be seen schematically in figure 2.

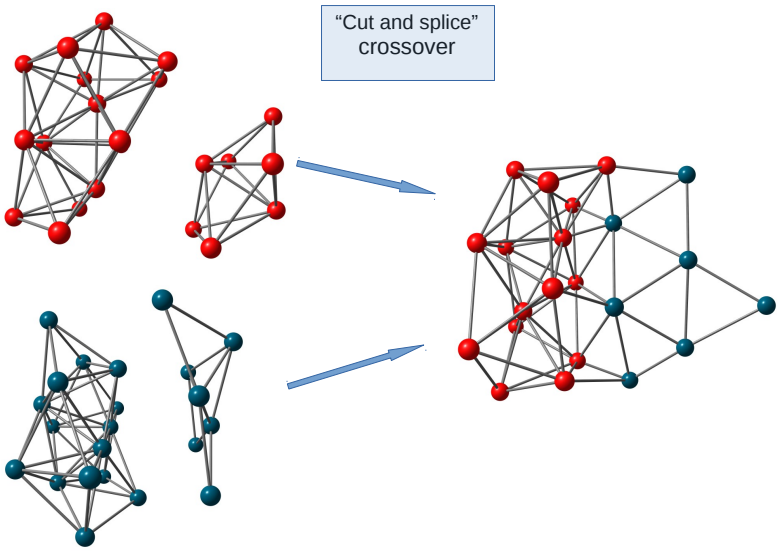

Figure 2: The cut-and-splice crossover operation as proposed by Deaven and Ho [59].

This transforms the process of movements on continuous points in the structure space to discrete jumps between local minima on the pes comparable to the procedure applied in the Basin hopping algorithm and greatly improves the performance of a genetic algorithm (= lamarckian approach) [61, 62]. Starting with a small population of clusters that have been created by placing N atoms randomly in a cubic box, a local relaxation of all population members follows. Before being subjected to a crossover process, the clusters have to go through a certain selection process. Which cluster finally is allowed to mate and pass at least parts of its genome to the following generation is decided by a fitness value assigned to each population member. Several schemes have been suggested to determine a fitness by either using its total energy directly or transformations of this energy to a function of the total energy [63]. The selection process may not rely on only a simple yes or no argument which cluster is allowed to form offspring, but should also give structures with a lower fitness the chance to be chosen for mating after the selection process, thus

having the chance of being selected proportionally to their fitness. A variable selection pressure is like in nature crucial to stabilize a population of individuals and whereas a too small pressure increases the number of generations to find an optimal solution, a too large one leads to a loss of genetic diversity and ultimately to a premature convergence to a non-optimal result. Three of the most widely used algorithms for selection are roulette wheel, rank-based and tournament methods [64]. Roulette wheel selection works by first summing up the fitness of all N population members to a value $\mathrm{S} = \sum_{i=1}^{N} s_i$. A random number R from the interval [0,S] is chosen and the fitness s of the population members summed up until $\sum_{i=1}^{n \leq N} s_i \geq R$ giving a probability of $\frac{s_i}{S}$ for a cluster i to be selected. However, it is not easily possible to change the selection pressure in fitness proportionate selection schemes and one therefore may modify the assigned fitness values to avoid that a single solution with a large fitness starts to dominate the gene pool. An easy way of introducing variable selection pressures is to use a tournament based method in which all offspring clusters are put in a selection pool first. Then a tournament is carried out by randomly choosing n clusters from the pool, comparing their fitness and allowing the cluster with the best fitness to be parent for the next generation. The selection pressure is then simply adjusted by varying the size of the tournament. While smaller tournaments allow clusters with a lower fitness to survive the selection process a larger tournament prefers structures with a higher fitness while making it more unlikely for clusters with a lower fitness to be selected. A rank-based selection process on the other hand ignores the relative fitness of all population members and bases the decision of allowing to cross-breed with other clusters upon a ranked list of the fitness of all members. This overcomes the problem in fitness proportionate schemes in which a structure with a fitness value much greater compared to the other clusters dominates the selection pool and prohibits a selection of weaker clusters in most of the selection rounds. All population members now obtain a fitness value proportional to their rank, while the selection pressure can be adjusted by using for example linear or exponential functions for this transformational assignment [65, 66]. These reallocation of fitness values can then be combined with a roulette wheel selection to receive a pool of clusters that have been chosen for mating. A very small part of each population finally undergoes a spontaneous mutation that locally modifies small features of the structural motif or changes the whole structure itself. Principally, every kind of mutation that introduces new genetic material helps to avoid premature convergence and keeps the genetic diversity but some of these operations have been found to be of higher value than others. At this point it is worth the effort to use insights originally achieved for the Basin-hopping method, as both approaches share the same problems. Wolf and Landmann [67] introduced several mutation operators beside simple random movements

in space to improve the efficiency of locating the global minimum energy structure including twinning, adding-etching of atoms and seeding operations. Oakley *et al.* [68] showed that a symmetrization scheme in which biased movements of atoms in a cluster towards more symmetrical structures reduced the energy evaluations necessary for a first visit of the global minimum energy structure in Lennard-Jones (LJ) clusters of various sizes. Rondina and Da Silva [69] demonstrated that the combination of both local and non-local operators in a dynamical scheme within the Basin-hopping approach is a universal tool that can be used in various systems in which interactions between atoms are not only described by model potentials like the LJ potential or semi-empirical Sutton-Chen potentials [70], but also simulations with ab-initio methods are feasible. Later however, it was shown that standard non-deterministic global optimization procedures including evolutionary algorithms suffer from several problems on complicated potential energy surfaces (e.g. multi-funnel landscapes) [71]. To avoid premature or slow convergence several authors introduced a niching scheme that ensures genetic diversity with an increased performance compared to the standard algorithm that is typically measured as the number of generations that have to be visited before the global minimum has been found or the number of times the global minimum was hit within a series of several individual runs (=the success rate). All these schemes have in common that they use structural information to lead the algorithm out of regions on the pes that are not promising or that have already been visited during an optimization run. Hartke proposed a method in which decahedral and icosahedral motifs that are found for example in LJ clusters were differentiated by first rotating two clusters into a position in which a plane projection of its atomic positions were least dense followed by a calculation of this density as the fraction of occupied squares in a discretization of this plane [72]. It is easy then to differentiate between icosahedral and decahedral structures as the icosahedral ones have a larger projected density than their decahedral counterparts. Cheng et al. used a connectivity table (ct) to compare two clusters for their similarity and they were able to show that the topological information in their ct is able to differentiate between certain structural motifs [73]. However, the crucial step within this procedure is to define a proper cutoff criterion to achieve the correct number of nearest neighbors for every atom. From the nearest neighbor contacts and the ct, it is then possible to define a distance measure that represents the similarity or dissimilarity between two clusters. Cheng *et al.* used this distance measure in LJ clusters and were able to effectively distinguish between several different motifs in LJ clusters up to a size of 110 particles including the Leary tetrahedron, Mackay and anti-Mackay icosahedra, the Mark's decahedron and closed packed structures. Using these niching schemes, they reported a huge improvement in the success rate in combination with a decreased number of local minimizations that were needed to hit the global minimum for

a given size for the first time. Another approach, described by Rossi and Ferrando, used the common neighbor analysis (CNA) to categorize the local environment around each atom into one of the earlier mentioned structural motifs. Originally proposed to identify phase transitions or to detect structural faults in clusters and bulk structures [74], this method works by assigning to each atomic pair an integer triple (m, n, k) with m being the number of nearest neighbors that are common to both atoms with n bonds between them and k bonds of them forming the longest connected chain of bonded atoms. Rossi and Ferrando now showed that it is possible to effectively sample the pes of the complicated multi-funnel cases of LJ_{38} and LJ_{75} by keeping track of only three integer triples $(5, 5, 5)$, $(4, 2, 2)$ and $(4, 2, 1)$. These three triples were sufficient to distinguish between clusters with icosahedral-, decahedral- and fcc-structures with up to 98 particles. Hartke *et al.* later stated that all evolutionary based algorithms benefit from niching schemes and they introduced another approach that can be set-up in an ad-hoc without special tuning or supervision during a global optimization run [75]. This scheme analyses the number of right angles and the longest distances among the atoms that surround a central atom yielding characteristic numbers for every structural motif that is typically found within clusters. An algorithm that applies such a niching scheme is able to easily differentiate between T_d, icosahedral, decahedral and closed-packed clusters in LJ clusters and shows an enhanced performance compared to the standard approach. Beside the introduction of niching schemes several other authors worked on improvements to the traditional Deaven and Ho algorithm. Bandow and Hartke *et al.* [76] and later Shayeghi *et al.* [77] discarded the generation-based approach in favor of a highly efficient parallel working pool-based approach that is universal and showed a better scalability compared to the standard approach. Instead of using an alternating series of serial and parallel operations that in general will lead to a highly fluctuating workload balance among the used CPU's, Hartke suggested a pool with asynchronous optimizations to perform the global optimizations. Therein a population of constant size with a certain number of individuals is held by a master process that also decides with a certain probability which pool members are subjected to crossover and mutation operations. The designated candidates are then send to designated sub-processes to perform the actual operation. Afterwards, the candidates are reported back to the master that decides via a niching scheme if a candidate is allowed to enter the pool by randomly replacing another structure, except for the best one currently in the pool (=elitism).

7 Implementation of a genetic algorithm

Throughout this work a slightly modified version of the traditional Deaven and Ho algorithm [59] was implemented in Python 2.6 and coupled to the atomic simulation environment (ASE) [1]. To make the best use of our available computational resources, we typically used population sizes that could be handled in reasonable times by our computational cluster without testing if such large populations are necessary to solve the given global optimization problem. Therefore, the size of a generation was fixed to 10 members while the number of children and mutants before the selection process is variable and was adjusted to the system under investigation. In figure 3 a flowchart is shown to highlight the different routines and the overall process of a typical global optimization run.

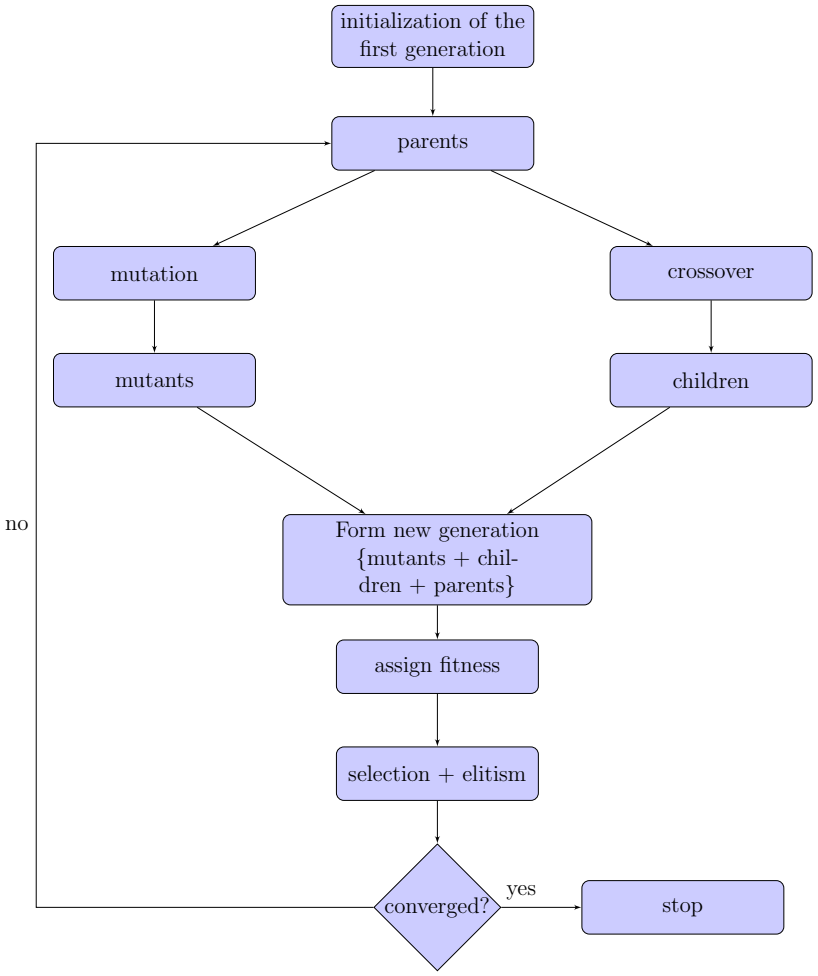

Figure 3: A simple flowchart of the implemented genetic algorithm.

As the flowchart already suggests, there are several branches that would allow an easy parallelization as there is no communication necessary between the single steps. Most of the CPU time is spent in the local optimization routine and therefore it makes perfectly

sense to distribute the task of all the local relaxations to different sub-processes to do the local optimizations. At the beginning of each calculation the algorithm creates a job server with a user-defined number of CPUS that the code is allowed to use. A master process then handles the distribution of the created structures to the slaves and the subsequent selection process that determines the candidates for the following generation. In addition, the master process also keeps track of the number of generations and the number of times that the same structure was repeatedly found to be the fittest one within a generation. Either of those values can be used by the master process to define a stopping criterion to end the global optimization procedure.

7.1 Local relaxations

Each candidate that has been created by any of the routines presented here was relaxed to its next local minimum with the FIRE algorithm [78] before a structure was considered for the next step. In contrast to the standard conjugate-gradient method or more sophisticated quasi-newton methods, the FIRE algorithm that is actually based on a molecular dynamics procedure shows a better performance, especially when the next local minimum on the pes is far away from the actual atomic configuration before the relaxation. In contrast to algorithms that used a Darwinistic approach (=no local relaxations), it was shown that Lamarckian based algorithms (=local relaxations, comparable to an adaptation to the environment known from biology) are superior in terms of the success rate and ability to efficiently sample the pes).

7.2 Start routine

Except for the cases when seeds were used to explore certain areas of the potential energy surface, all global optimization runs have been started from randomly created structures. Taking the $A_m\mathrm{B}_n$, cluster as an example, the first generation was created by placing the $m+n$ atoms randomly within a cubic box of volume V_{box} that scaled with the number of atoms as

$$V_{box} = m \cdot \frac{a_A^3}{4} + n \cdot \frac{a_B^3}{4} \ . \tag{6}$$

Thereby, the volume V_{box} results from the sum of the volumes that a single atom would occupy in a given fcc-lattice with a_A and a_B being the corresponding experimental lattice constants of the bulk structures of the elements A and B.

7.3 Crossover routine

The mating process between two structures is one of the methods that effectively introduces new genetic material (=new structural motifs) into the algorithm. A cut-and-splice procedure as shown in figure 2 was used for the crossover and the creation of offsprings. In contrast to the original recipe that defined a plane through the center of mass, we used arbitrarily defined planes that work better in cases when more than a single element is present within a system, especially if the stoichiometry has to be constrained during a search. Both halves are then rearranged, randomly rotated and combined in a way that a minimum distance between the two parts is maintained (typically the bonding distance of the dimer). The number of offsprings that should be created by the program is left to the user without a special selection scheme and should be tested in advance to any production runs. Offspring clusters do not replace any clusters yet and they will be added to the pool of possible candidates for the next generation.

7.4 Mutation routine

As mentioned for the crossover routine, there was no selection rule used to decide if a given cluster undergoes a mutation or not. Instead, the user controls the number of times that all clusters will be subjected to a mutation. The mutants will not replace any clusters at that step and they will all be added to the pool of possible candidates for the next generation. Several mutation operations are available during a global optimization run in the algorithm:

- Random displacements of all atoms with a Gaussian-distributed step-size [79].
- Permutation of two atomic species to explicitly include homotops of the same structural motif in the search process.
- A twinning mutation in which two halves of a cluster are rotated by a small random angle in opposite directions [67].
- An etch-add process in which randomly picked atoms are removed and placed next to other atoms at the typical bond length of the dimer [67].
- The "Onepar" routine as described by Joswig et al. that interchanges two halves of a cluster through a randomly defined plane [80].

The algorithm chooses one of the described operations with equal probability, however it is also possible to change the weights of the mutation operations if it is beneficial for a

given system (e.g. twinning mutations to explicitly remove stacking faults). In addition, an energy criterion can be defined which ensures that only mutants are created with a certain difference in energy compared to the structure with the lowest energy that has been found so far during a run.

7.5 Selection routine

To decide which clusters are allowed to be passed on to the next generation a selection scheme was used on a combined pool consisting of the parent clusters, the offspring structures and the mutants. The selection is done with the total energy as the fitness criterion but later improvements of the algorithm will also include several arbitrarily defined fitness definitions that are not based upon the total energy of a cluster. The user can choose between two methods, a simple tournament or the roulette wheel selection [81]. Throughout this work a tournament was used as the selection process and therefore we refer the interested reader to the work of Lipowski *et al.* for further details [81]. Before the tournament starts, any structural duplicates will be removed by applying a simple criterion that is based upon the interatomic distances [79]. We consider two clusters A and B to be structural equivalent if Δ calculated from

$$\Delta = \frac{\sum_i (d_{A,\{i\}} - d_{B,\{i\}})^2}{\sum_i (d_{A,\{i\}}^2 + d_{B,\{i\}}^2)} \tag{7}$$

with $d_{A,\{i\}}$ and $d_{B,\{i\}}$ being a sorted list of interatomic distances in cluster A and cluster B is smaller than 10^{-4}. For the tournament, the algorithm chooses a predefined number of individuals (=the tournament size) $n_{Selection}$ from the pool, compares their fitness and passes the cluster with the best fitness to the next generation. This process is repeated until the next generation has the same size as the preceding one. The parameter $n_{Selection}$ can be changed to tune the selection pressure towards convergence of the algorithm. A too small value of $n_{Selection}$ will make the algorithm work inefficient, as it will not effectively sample regions with low energy on the potential energy surface, whereas a too large value will in general lead to premature convergence. Furthermore it is possible to use the elitism concept to pass the lowest or any other cluster unmodified to the next generation to avoid a loss of a beneficial genome.

7.6 Convergence

In general, it is not possible to define a simple stopping criterion for any global optimization algorithm due to the fact that the whole potential energy surface is unknown. Thus,

there is also no proof known that an identified candidate for the global minimum is really the global minimum. However, we define a simple criterion and consider the algorithm to be converged if there was no fitter candidate found within n consecutive steps. This parameter should be chosen according to the size of the cluster under investigation and typically lies between 100 and 300 generations.

8 Testing the implemented genetic algorithm

8.1 The Lennard-Jones Potential

To demonstrate that the implemented genetic algorithm works, we show the results of a global optimization run for the three cases of Leonard-Jones (LJ) [82] systems with 38, 55 and 75 particles. The Lennard-Jones potential is a pairwise defined function and is typically used to describe clusters with weakly interacting atoms (e.g. clusters made of noble gases) [83] or as a test potential for newly proposed global optimization algorithms. It is of the form

$$E = 4\varepsilon \sum_{i<j} \left[\left(\frac{\sigma}{r_{ij}}\right)^{12} - \left(\frac{\sigma}{r_{ij}}\right)^{6} \right] \tag{8}$$

where ε is the pair potential well depth, σ is the length scale of the potential function and r_{ij} represents the distance between the two particles i and j. To allow a comparison, ε and σ are usually set equal to 1 [84]. The two systems LJ_{38} and LJ_{75} have been chosen because of their complicated energetic landscapes that consists of a double-funnel with a large attractive basin for the icosahedral motif. Both cases offer a high chance that the algorithm will be trapped within the icosahedral basin having little chance to leave that part of the hyperspace again. Additionally, it was shown that these multi-funnels are separated by a liquid-like structure space that every algorithm would have to overcome to be able to efficiently sample the whole potential energy surface [53]. In figure 4, we show the result of an exemplary optimization of LJ_{38} to demonstrate that the implemented code is able to effectively sample the potential energy surface. The global minimum energy structure of LJ_{38} is believed to be a piece of an fcc crystal with point group O_h as shown in figure 4, whereas the second and third lowest isomer correspond to incomplete Mackay-icosahedra. The large attraction of the icosahedral basin can immediately be seen in figure 4, the third lowest isomer is already encountered after a few generations, closely followed by the second lowest isomer that was first found after about 10 generations. To locate the actual global minimum, the algorithm had to run for another 250 generations which illustrates the problem of identifying the correct global minimum energy structure of

point group (pg) O_h in that system. However, it also demonstrates that the implemented algorithm is capable of leaving a deep funnel which is one of the main criteria for a global optimization procedure. LJ_{55} on the other side has a much simpler pes with a single funnel only that leads to a highly symmetric icosahedral structure of pg I_h. The implemented algorithm locates the ideal Mackay icosahedron from unbiased start structures quite fast after about 15 generations as one can see from figure 5. At last, the same results are shown for LJ_{75} in figure 6, a system that was described as being exceptionally complicated [85].

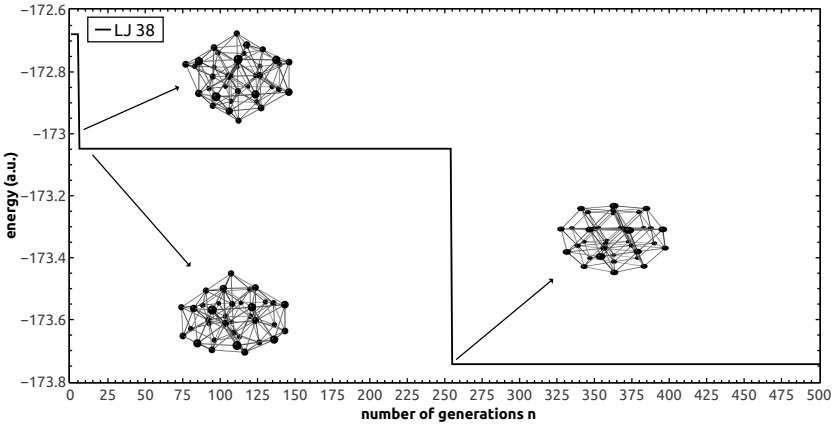

Figure 4: The change in energy of the fittest population member in a global optimization search in the LJ_{38} system. The population size P was set to 10 and we allowed the three lowest isomers in a generation to form offsprings with all other clusters. Different mutants were created for three times from all current population members. The resulting 66 candidates were subjected to the selection process (tournament of size 10) to form the subsequent generation (the remaining fittest cluster was passed unmodified to the next generation).

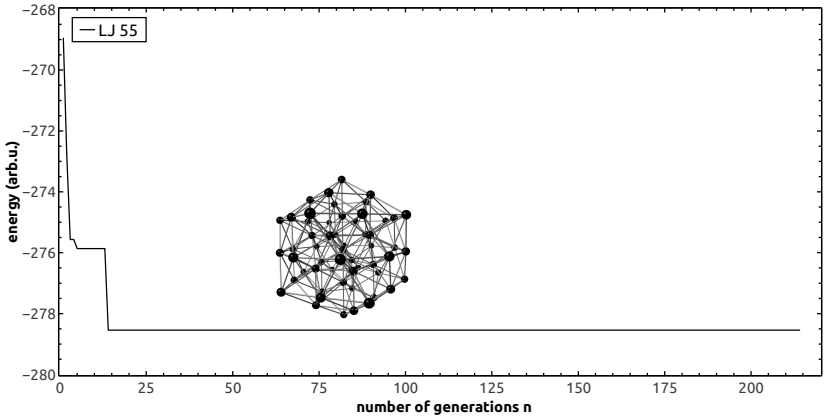

Figure 5: The change in energy of the fittest population member in a global optimization search in the LJ_{55} system with the same parameters used that were described in figure 4.

Several other unbiased algorithms including Basin-hopping [16] failed to locate the

global minimum without the use of seeds or niching schemes. Even some of the more sophisticated and previously proposed global optimization methods were not able to converge to the correct decahedral global minimum energy structure for the series LJ_{75-77}. Laykhov et al. used a local order parameter to quantify the local symmetry around every atom in a cluster together with a clustering method that is based on the fingerprint theory [86] to keep the structural diversity within a population as large as possible [85]. Without this additional information and the classification of every structure into one of the main motifs (fcc, hcp, bcc, sc and ico), the algorithm had to sample many more structures before it would be able to converge to the decahedral global minimum energy structure. Rogan et al. also failed to locate the decahedral global minimum with their approach consisting of coupling of an efficient and robust local minimizer [78] with a similarity index as described by Grigoryan and Springborg et al. [87] to discriminate certain structural motifs during their optimizations of randomly created seeds [88]. Also other nature-inspired and newer methods like the artificial bee colony and the Firefly algorithm (based on swarm intelligence) were incapable to locate the decahedral structures for LJ_{75-77} [89, 90].

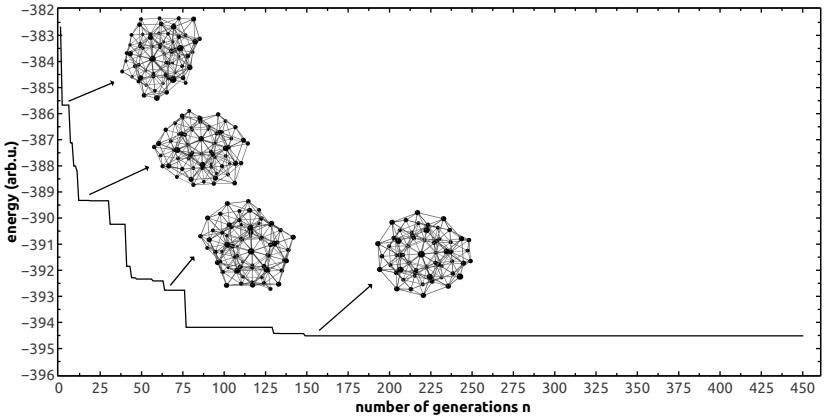

Figure 6: The change in energy of the fittest population member in a global optimization search in the LJ_{75} system with the same parameters used that were described in figure 4. All clusters shown have been rotated to give a view along the longest chain of atoms to illustrate the local fivefold symmetries within the clusters.

This chapter showed that a parallel working genetic algorithm has been successfully implemented as well as tests on several examples of the Lennard-Jones system have been presented. We also gave an introduction of problematic cases and how they could be solved in the future by further changes to the code.

Part II

Total-Energy Methods

9 Theoretical models

The genetic algorithm that was introduced in the last chapter is a universal tool for global optimization procedures and therefore not restricted to a special kind of potential. Recently, several authors coupled a genetic algorithm to the ab-initio density functional theory, but such an approach is typically restricted to smaller systems with only a few number of atoms due to computational demands [91, 92, 93, 94, 95, 96, 97]. A more feasible approach that is regularly used consists in coupling a global optimization algorithm to a semi empirical method that first creates candidates for the global minimum which are afterwards treated with more accurate ab-initio methods. Depending on the type of system, several methods have been proposed to efficiently treat not only metals (e.g. the RGL potential [98], the Sutton-Chen potential [70] or the Embedded-atom method and its modification of Daw and Baskes [99] and finally the effective medium theory [100]), but also semiconductors (e.g. the Brenner potential [101] and the Tersoff potential [102]). A more general approach that is not restricted to a special class of materials and that gives good results for various properties compared to ab-initio methods is the density functional tight-binding (DFTB) approximation [103] that was used during this work for most of the global optimization procedures. All of the potentials that were used and their theoretical foundations are introduced in the next sections.

10 The Born-Oppenheimer Approximation

Finding appropriate solutions to the Schrödinger equation is the main problem of quantum chemistry since the beginning of its development. At the early stages of its formulation in 1926, all approaches were based on the complicated calculation of a wavefunction, which is not observable and therefore not accessible to measurement. In its time-independent form the Schrödinger equation for a many-body system reads as

$$\hat{H}\Psi = E\Psi \ , \tag{9}$$

with the general Hamilton operator being the sum of several terms

$$\hat{H} = T_c + T_e + V_{cc} + V_{ee} + V_{ec} \ , \tag{10}$$

where T_e and T_c represent the kinetic energy of the electrons and the nuclei respectively and V_{cc}, V_{ee} and V_{ec} describe the nucleus-nucleus, electron-electron and electron-nuclei interactions. In both of the two commonly used electronic structure methods, wavefunction based approaches and the density functional theory (DFT), the Born-Oppenheimer (BO) approximation is used to greatly simplify the Schrödinger equation as the Hamiltonian $\hat{H}$ of a system can be separated into a sum of two Hamiltonians with the first Hamiltonian $\hat{H}_c$ being dependent on nucleus-nucleus interactions and the kinetic energies of the nuclei. The second Hamiltonian $\hat{H}_e$ depends on electron-electron and electron-nuclei interactions as well as the kinetic energy of the electrons and therefore we can write

$$\hat{H} = \hat{H}_c + \hat{H}_e \ , \tag{11}$$

$$\hat{H}_c = T_c + V_{cc} \ , \tag{12}$$

$$\hat{H}_e = T_e + V_{ee} + V_{ec} \ . \tag{13}$$

By using that the nuclei are much heavier than the electrons so that the movements of the two sets of particles, electrons and nuclei, become decoupled, it is possible to factorize the wavefunction

$$\Psi(\vec{r}, \vec{R}) = \Psi_e(\vec{r}, \vec{R})\Psi_c(\vec{R}). \tag{14}$$

Of the same reasons, the positions of the nuclei may be held fixed ($T_c = 0$) and therefore a constant nucleus-nucleus potential V_{cc} in eq.10 can be assumed, so that the Schrödinger equation can be written as

$$(\hat{H}_e + V_{cc})\Psi_e(\vec{r}, \vec{R})\Psi_c(\vec{R}) = E\Psi_e(\vec{r}, \vec{R})\Psi_c(\vec{R}) \ , \tag{15}$$

which yields after division with eq.14

$$\hat{H}_e\Psi_e = (E - V_{cc})\Psi_e \ , \tag{16}$$

and finally the so-called electronic Schrödinger equation

$$\hat{H}_e\Psi_e(\vec{r}, \vec{R}) = E_e(\vec{R})\Psi_e(\vec{r}, \vec{R}) \ , \tag{17}$$

in which the eigenvalues $E_e = (E - V_{cc})$ depend parametrically on the positions $\vec{R}$ of the nuclei. For most of the questions in theoretical chemistry, it is sufficient to solve the electronic Schrödinger equation under the assumption that the BO approximation is valid for the system under investigation. Certain dynamical problems (e.g. molecular dynamics), systems in which several potential energy surfaces cross each other, or in cases

where a system leaves the electronic ground state after a change in the positions of the nuclei cannot be treated by the BO approximation and other methods have to be used which however are beyond the scope of this work.

11 Density functional theory

11.1 The Theorems of Hohenberg and Kohn

Based on the work of Thomas and Fermi, Hohenberg and Kohn demonstrated that the external potential $V_{ext}(\vec{r})$ and the thereof resulting total electronic energy E_e is a unique functional of the ground-state electron density $\rho(\vec{r})$ (known as the first Hohenberg-Kohn theorem) [104]. This energy $E_e[\rho]$ can be written in the following way,

$$E[\rho(\vec{r})] = F[\rho(\vec{r})] + \int V_{ext}(\vec{r})\rho(\vec{r})d\vec{r} \; . \tag{18}$$

where $F[\rho(\vec{r})]$ is an universal functional of the electron density $\rho(\vec{r})$ of the form

$$F[\rho(\vec{r})] = T[\rho] + V_c[\rho] \; , \tag{19}$$

with the kinetic energy of the electrons $T[\rho]$ and the potential energy due to the electron-electron interactions $V_c[\rho]$, both as a functional of the electron density $\rho(\vec{r})$. The external potential $V_{ext}(\vec{r})$ is generated by the nuclei and of Coulomb-type, but may also contain additional potentials (i.e. external electrostatic potentials). Now the electron density $\rho(\vec{r})$ should also define the total number of electrons N:

$$N = \int \rho(\vec{r})d\vec{r} \; . \tag{20}$$

Not only is the electron density accessible through experiments (e.g. X-ray diffraction), it can also be handled much easier computationally as it depends only on a single space coordinate $\vec{r} = (x, y, z)$, whereas in wavefunction-based approaches the $3N$ ($4N$ if spin is included) coordinates of all interacting particles have to be taken into account. The second theorem of Hohenberg and Kohn states that for any trial density function $\rho'(\vec{r})$ that satisfies eq.20, the expectation value of $E_e[\rho]$ is equal to or larger than the true electronic ground-state energy of the system

$$E_e[\rho'(\vec{r})] \geq E_e[\rho(\vec{r})] \; , \tag{21}$$

which is the density functional counterpart to the Rayleigh-Ritz variation principle in wavefunction based approaches. Unfortunately, the functional of the kinetic energy of the

electrons $T[\rho]$ and the potential $V_{ee}[\rho]$ of the electron-electron interaction as a functional of the density are unknown, thus making it impossible to formulate an exact Hamiltonian. Long before the theorems of Hohenberg and Kohn, Thomas and Fermi proposed approximations to both, for the kinetic energy $T[\rho]$ and for $V_{ee}[\rho]$, though their approach still has several shortcomings if used for calculations in molecules (e.g. the method fails in the description of the chemical bond) [105, 106].

11.2 The Kohn-Sham equations

Since we know from the second Hohenberg-Kohn theorem that $E_e[\rho^{'}(\vec{r})]$ has a minimum for the true ground state density $\rho(\vec{r})$ eq. (21) we can obtain this minimum by the variation

$$\delta E_e[\rho] \equiv E_e[\rho + \delta\rho] - E_e[\rho] = 0, \tag{22}$$

under the constraint that the total number of electrons is conserved as defined from eq. (20). By using a Lagrange multiplier (μ) eqs. (22) and (20) can be combined and rewritten as a functional derivative

$$\frac{\delta}{\delta\rho(\vec{r})}\left\{E_e[\rho(\vec{r})] - \mu[\int \rho(\vec{r})]d\vec{r} - N\right\} = 0\ . \tag{23}$$

However, up to now $E_e[\rho(\vec{r})]$ is still unknown, but contains several terms including the kinetic energy of the electrons as a functional of the density $T[\rho(\vec{r})]$, the classical Coulomb interaction energy V_c between the electrons defined from

$$\frac{1}{2}\int\int \frac{\rho(\vec{r_1})\rho(\vec{r_2})}{|\vec{r_1} - \vec{r_2}|}d\vec{r_1}d\vec{r_2} = \frac{1}{2}\int V_c(\vec{r})\rho(\vec{r})d\vec{r}\ , \tag{24}$$

and another term due to the external potential of the nuclei,

$$\int V_{ext}(\vec{r})\rho(\vec{r})d\vec{r}\ . \tag{25}$$

In total we have for $E_e[\rho(\vec{r})$ the expression

$$E_e[\rho(\vec{r})] = T[\rho(\vec{r})] + \int V_{ext}(\vec{r})\rho(\vec{r})d\vec{r} + \frac{1}{2}\int V_c(\vec{r})\rho(\vec{r})d\vec{r} + E^{'}_{xc}[\rho(\vec{r})]\ , \tag{26}$$

and the term $E^{'}_{xc}[\rho(\vec{r})]$ has been introduced to hide all of the other additional complications that arise due to the many-body effects including exchange and correlation interactions. After application of eq. (23) we obtain

$$\frac{\delta T}{\delta \rho} + V_{ext}(\vec{r}) + V_c(\vec{r}) + \frac{\delta E'_{xc}}{\delta \rho} = \mu \ . \tag{27}$$

To overcome the problem of having to find an accurate formulation for the kinetic energy $T[\rho(\vec{r})]$, Kohn and Sham introduced a method that makes use of the orbital concept known from Hartree-Fock theory. To get a solvable set of equations Kohn and Sham replaced the unknown $T[\rho]$ in DFT with the kinetic energy that one obtains from a fictitious system of non-interacting quasi-particles that move in a selected, single-particle external potential $V_{ref}(\vec{r})$. $V_{ref}(\vec{r})$ is chosen as such, so that the reference system has the same density and energy as the true electron density. Since the particles in that fictive system are non-interacting, it is possible to calculate $E_e[\rho(\vec{r})]$ from a much simpler expression,

$$E_e[\rho(\vec{r})] = T_0[\rho(\vec{r})] + \int V_{eff}(\vec{r})\rho(\vec{r})d\vec{r} \ . \tag{28}$$

Analogous to eq. (27) we can calculate

$$\frac{\delta T_0}{\delta \rho} + V_{eff}(\vec{r}) = \mu \tag{29}$$

and from a comparison of the eqs. (28) and (27) we can identify the effective potential $V_{eff}(\vec{r})$ for the fictitious system as

$$V_{eff}(\vec{r}) = \frac{\delta T}{\delta \rho} - \frac{\delta T_0}{\delta \rho} + V_{ext}(\vec{r}) + V_c(\vec{r}) + \frac{\delta E'_{xc}}{\delta \rho} \ . \tag{30}$$

The Hamiltonian for such a system of non-interacting particles then reads

$$\hat{H}_{ref} = \sum_{i=1}^{N} \left[-\frac{1}{2}\nabla^2_{\vec{r_i}} + V_{eff}(\vec{r_i}) \right] , \tag{31}$$

and the ground-state density can be obtained from solving the one-electron Schrödinger equations $\hat{H}_{ref}\Psi = E\Psi$ where the solutions can be written as a single Slater determinant

$$\Psi = |\phi_1, \phi_2, ..., \phi_N| \ , \tag{32}$$

with the single-particle orbitals ϕ_N. The ground-state density can then be constructed from the equation

$$\rho(\vec{r}) = \sum_{i=1}^{N} |\phi_i(\vec{r})|^2 \ . \tag{33}$$

However, there is still the problem that the exact form of the effective potential $V_{eff}(\vec{r})$ is not known. The unknown exchange-correlation potential V_{xc} defined as

$$V_{xc} = \frac{\delta E_{xc}}{\delta \rho} = \frac{\delta T}{\delta \rho} - \frac{\delta T_0}{\delta \rho} + \frac{\delta E'_{xc}}{\delta \rho}, \tag{34}$$

must be approximated and there are several approximations that work well for certain properties while they may fail in the description of others. Originally Kohn and Sham had the intention to make the contribution of the unknown exchange-correlation energy to the total energy as small as possible, but it turned out that an accurate description is still crucial for the description of binding properties in molecules and solids. An introduction to the exchange-correlation problem is given in the following section.

11.3 The exchange-correlation Problem

11.3.1 The Local Density Approximation LDA

Finding a reliable functional for $E_{xc}[\rho]$ is one of the main problems in DFT. All functionals currently used are still approximations to the true exchange-correlation functional in DFT resulting in the fact that no functional is accurate for all systems and all properties. This fact has been pictorized through the DFT Jacobs ladder to heaven on which every rung represents a different and more complex approximation, that should have the features of former rungs with additional wider applicability to new problems [107]. Starting from local density approximation functionals (LDA) that are rather useless for calculations with chemical accuracy due to strong tendency for overbinding to generalized gradient approximations (GGA) that partially correct this fault, to meta-GGAs and hybrid functionals that are at present the most widely used functionals for molecular DFT calculations. It should also be kept in mind that functionals do not perform equally well for molecular systems and crystals with their translational symmetry properties [108]. In general it is possible to write the exchange correlation functional E_{xc} as

$$E_{xc}[\rho] = \int \varepsilon_{xc}(\vec{r})\rho(\vec{r})dr \ , \tag{35}$$

where ε_{xc} often is approximated by the relation

$$\varepsilon_{xc}(\vec{r}) = \varepsilon_{xc}[\rho(\vec{r}), |\nabla\rho(\vec{r})|, |\nabla^2\rho(\vec{r})|, ...] \ . \tag{36}$$

It is also beneficial to separate the exchange-correlation functional into two parts and to treat them independently afterwards according to

$$E_{xc}[\rho] = E_x[\rho] + E_c[\rho] \ . \tag{37}$$

At the lowest level of approximation (the local density approximation LDA) E_x was calculated by Dirac for a homogeneous electron gas [109] yielding the expression

$$E_x^{LDA}[\rho] = A \int \rho(\vec{r})^{\frac{4}{3}} dr \ , \tag{38}$$

with the exchange potential

$$V_x(\vec{r}) = \frac{4}{3} A \rho(\vec{r})^{\frac{1}{3}} \ . \tag{39}$$

Obtaining an analytic expression for the correlation effects in an homogeneous electron gas is much more difficult and approximations have been formulated only for the cases of an infinitely weak and infinitely strong correlated electron gas (the so-called high density and low density limits). The electron correlation effects are typically represented as a function of the density parameter r_s and the relative spin polarization ζ, both defined from

$$r_s = \left(\frac{3}{4\pi(n\downarrow + n\uparrow)} \right)^{\frac{1}{3}} \ , \tag{40}$$

$$\zeta = \frac{n\uparrow - n\downarrow}{n\uparrow + n\downarrow} \ . \tag{41}$$

and where $n\downarrow\uparrow$ corresponds to the spin-up $n\uparrow$ and spin-down $n\downarrow$ electrons. In the case of the high-density limit (= small r_s [110]) the correlation energy ε_c per electron can be expanded as

$$\varepsilon_c(r_s, \zeta) = c_0(\zeta) \ln(r_s) - c_1(\zeta) + c_2(\zeta) r_s \ln(r_s) - c_3(\zeta) r_s + ... \ , \tag{42}$$

whereas in the case of the low-density limit [110] the expansion reads

$$\varepsilon_c(r_s, \zeta) = \frac{-d_0(\zeta)}{r_s^p} + \frac{-d_0(\zeta)}{r_s^{2p-1/2}} + ... \ , \tag{43}$$

with p being equal to $\frac{3}{4}$. The coefficients for both cases are fitted to reproduce highly accurate results from quantum Monte Carlo methods (e.g. the VWN correlation functional of Vosko-Wilk-Nusair [111] and the ones by Ceperley-Alder CA [112] and Perdew-Wang PW92 [110]. Parameters for the intermediate case are not calculated and are interpolated between the high- and low-density case. The local functional LDA typically performs well for the prediction of for example lattice constants in crystals due to their slowly varying

electron density (e.g. in metals). However, it often fails in inhomogeneous systems that are present for example in molecular structures, especially in the prediction of their binding energies. The next rung on the Jacobs DFT ladder would be to include the gradient of the density at a given point as shown in eq. (36). These GGA's in general improve most of the properties for which LDA's give a poor description including atomization and binding energies, energy barriers and structural energy differences. In addition they also reduce the tendency to overbinding and favor density inhomogeneities in comparison to LDA's [113].

12 Density functional tight-binding

The density functional tight-binding method was introduced by Porezag et al. [114] and later improved by Elstner et al. [115] as an approximate semiempirical method to ab-initio DFT. Originally proposed to treat covalent systems, the method has been proven to be reliable also for metals [116] and ionic materials [117]. It shares the same strengths and weaknesses as DFT at only a fraction of the computational cost of full DFT calculations which makes it not only possible to study large systems (e.g. proteins), also larger timescales are accessible in molecular dynamic simulations. Likewise as for all semiempirical approaches the performance of DFTB depends critically on its parametrization process which means that excessive testing is always necessary to ensure maximum transferability for a given set of parameters. Starting from DFT where the Kohn-Sham energy for a system of non-interacting electrons as a functional of the density ρ was given as

$$E_e[\rho] = \sum_a f_i \left\langle \Psi_i \right| \left(-\frac{1}{2}\nabla^2 + V_{ext}(\vec{r}) \right) \left| \Psi_i \right\rangle + \frac{1}{2} \int\int \frac{\rho(\vec{r_1})\rho(\vec{r_2})}{|\vec{r_1} - \vec{r_2}|} dr_1 dr_2 + E_{xc}[\rho] + V_{cc} \ , \quad (44)$$

with $f_i \in [0, 2]$ being a function that accounts for different occupations in the single-particle state Ψ_i and usually being taken from the Fermi function

$$f_i = 2[\exp(\varepsilon_i - \mu)/k_B T + 1]^{-1} \quad (45)$$

and V_{cc} being the repulsive ion-ion interaction for all N nuclei with the valence numbers Z_α and Z_β, calculated from

$$V_{cc} = \frac{1}{2} \sum_{\alpha \neq \beta} \frac{Z_\alpha Z_\beta}{|\vec{R_\alpha} - \vec{R_\beta}|} \ . \quad (46)$$

The chemical potential μ is chosen so that $\sum f_i = N$ with N being the number of electrons in the system. Equation 44 is exact and the DFTB method now assumes the following scenario as an approximation to it: A neutral system with density ρ_0 is considered that is composed of atomic densities with no charge transfer between the atoms. While the density ρ_0 does not minimize 44, it differs only by a small amount $\delta\rho(\vec{r})$

$$\rho(\vec{r}) = \rho_0(\vec{r}) + \delta\rho_0(\vec{r}) \tag{47}$$

The change in energy for small fluctuations $\delta\rho(\vec{r})$ can then be approximated by an expansion of 44 up to second order in $\delta\rho$:

$$\begin{aligned} E_e[\delta\rho] \approx \sum_i f_i \left\langle \Psi_i \right| -\frac{1}{2}\nabla^2 + V_{ext}(\vec{r}) + V_H[\rho_0] + V_{xc}[\rho_0] \left| \Psi_i \right\rangle \\ + \frac{1}{2}\int\int \left(\frac{\delta^2 E_{xc}[\rho_0]}{\delta\rho(\vec{r_1})\delta\rho(\vec{r_2})} + \frac{1}{|\vec{r_1} - \vec{r_2}|} \right) \delta\rho(\vec{r_1})\delta\rho(\vec{r_2}) d\vec{r_1} d\vec{r_2} \\ - \left[\frac{1}{2}\int V_H[\rho_0]\rho_0(\vec{r}) d\vec{r} + E_{xc}[\rho_0] - \int V_{xc}[\rho_0]\rho_0(\vec{r}) d\vec{r} + V_{cc} \right]. \end{aligned} \tag{48}$$

Now these terms represent the single particle band structure energy E_{BS} for a small change in ρ (the first-order term)

$$E_{BS}[\delta\rho] = \sum_i f_i \left\langle \Psi_i \right| \hat{H}_0 \left| \Psi_i \right\rangle \ , \tag{49}$$

the energy that arises due to charge fluctuations between neighboring atoms (the second-order term)

$$E_{coulomb}[\partial\rho] = \frac{1}{2}\int\int \left(\frac{\partial^2 E_{xc}[\rho_0]}{\partial\rho(\vec{r_1})\partial\rho(\vec{r_2})} + \frac{1}{|\vec{r_1} - \vec{r_2}|} \right) \partial\rho(\vec{r_1})\partial\rho(\vec{r_2}) d\vec{r_1} d\vec{r_2} \ , \tag{50}$$

and the repulsive energy that is the sum of all the remaining terms including a contribution due to the ion-ion repulsive interactions V_{cc}

$$E_{rep} = -\left[\frac{1}{2}\int V_H[\rho_0]\rho_0(\vec{r}) d\vec{r} + E_{xc}[\rho_0] - \int V_{xc}[\rho_0]\rho_0(\vec{r}) d\vec{r} + V_{cc} \right] . \tag{51}$$

In the so-called non-self consistent charge (non-SCC) approach one neglects the second-order term in $\delta\rho$ $E_{coulomb}$, which should work in cases where the chemical bonds within a system are dominated by covalent interactions with almost no charge transfer between the atoms. Highly ionic systems with polar bonds should be treated by including the second-order terms because the influence of larger charge transfers between atoms on the total energies can not be corrected in the parametrization process. The pairwise defined

repulsive function E_{rep} for an atom pair i, j can be considered as the counterpart of the complicated exchange-correlation functional from full DFT and is typically fitted to high-level ab-initio calculations or experimental results as

$$E_{rep} = \sum_{i<j} V_{rep}^{ij}(\vec{r}) \ . \tag{52}$$

12.1 The tight-binding approximation

The DFTB method uses a linear combination of atomic orbitals (LCAO) based approach with the orbitals expanded in terms of a minimal set of atomic-centred, non-orthogonal basis functions to solve the Kohn-Sham eigenvalue equations for an effective potential v_{eff}. Thus, the ith orbital is written as

$$\Psi_i(\vec{r}) = \sum_v c_{vi}\phi_v(\vec{r}) \ , \tag{53}$$

with ϕ_ν being the ν-th basis function. The band structure energy E_{BS} for an effective potential is thereby calculated as the sum over the eigenvalues of all occupied orbitals. Substitution of the Hamiltonian $\hat{H} = \hat{T} + V_{eff}$ with the kinetic energy operator $\hat{T}$ and the effective potential V_{eff} into the time independent Schrödinger equation $\hat{H_{eff}}\Psi_i(\vec{r}) = \varepsilon_i\Psi_i(\vec{r})$ gives in analogy to the DFT method with the single particle energy $E_{BS} = \sum_i f_i\varepsilon_i$ for the total energy the expression

$$E = \sum_i f_i\varepsilon_i + \sum_{i<j} V_{rep}^{ij}(\vec{r}) \ . \tag{54}$$

with f_i and ε_i being the occupation and energy of the i-th orbital, respectively. The minimum of this expression can again be found by using the variational principle with the undetermined Lagrange multipliers ε_i, constraining the norm of the wavefunctions

$$\partial\left(E - \sum_i \varepsilon_i \left\langle\Psi_i|\Psi_i\right\rangle\right) \ , \tag{55}$$

to finally obtain the eigenvalue equation

$$\sum_v c_{vi}^a(H_{vi} - \varepsilon_a S_{vi}) = 0 \ , \tag{56}$$

with

$$H_{vi} = \left\langle\phi_v\right| \hat{H} \left|\phi_i\right\rangle \qquad \text{and} \qquad S_{vi} = \left\langle\phi_v|\phi_i\right\rangle \ , \tag{57}$$

and the assumption that

$$\langle\phi_v|\hat{T}+V_{\text{eff}}|\phi_i\rangle = \begin{cases} \langle\phi_v|\hat{T}+V_n|\phi_i\rangle & \text{for } \phi_v,\ \phi_i \text{ both on atom } n \\ \langle\phi_v|\hat{T}+V_n+V_m|\phi_i\rangle & \text{for } \phi_v,\ \phi_i \text{ on atoms } n \neq m \\ 0 & \text{otherwise.} \end{cases} \tag{58}$$

The elements H_{vi} and S_{vi} are pre-calculated as a function of the distance $\vec{r}$ in diatomic molecules using the Slater-Koster rules [118]. In addition it is also assumed that the effective potential V_{eff} can be written as a superposition of atomic potentials like

$$V_{eff}(\vec{r}) = \sum_n V_n(|\vec{r}-\vec{R}|)\ , \tag{59}$$

with $\vec{R_n}$ being the position of the n-th atom. The potential $V_n(r)$ is the potential of the free, and isolated n-th atom $V_n^0(\vec{r})$ that is augmented by a short-ranged confining potential $V_{conf}(r)$ that leads to a contraction of the orbitals on the n-th atom

$$V_n(r) = V_n^0(r) + V_{conf}(r) \qquad \text{with} \qquad \mathrm{V_{conf}(r)} = \left(\frac{\mathrm{r}}{\mathrm{r_0}}\right)^2. \tag{60}$$

for $r < r_0$ and zero otherwise.

12.2 Parametrization of the DFTB method

Calculation of the total energy for a given molecule or crystal requires an optimization of both, an ideal value for r_0 in the confining potential and an appropriate repulsion potential $V_{rep}(r)$. The electronic part of DFTB is typically fitted by varying r_0 to get the best agreement between ab-initio calculated bandstructures and the ones obtained by DFTB (an example of such a fit for hcp-cadmium can be seen in figure 7).

The repulsion potential $V_{rep}(r)$ can be determined by minimizing the force differences $|F^{DFT} - F^{DFTB}|$ as proposed by Koskinen and Mäkinen [3]. In the case of highly symmetric molecules, clusters or crystal where all bond lengths are equal, the derivative of the repulsion energy for N bonds can be calculated from

$$V_{rep}^{'}(r) = \frac{E_{DFT}^{'} - E_{BS}^{'}}{N}. \tag{61}$$

Additionally for local extrema on the potential energy surface it is clear that $E_{DFT}^{'} = 0$ so that

$$V_{rep}^{'}(r) = \frac{-E_{BS}^{'}}{N}. \tag{62}$$

In cases when there are different bond lengths for a system at equilibrium it is possible to construct V_{rep} from the minimization of

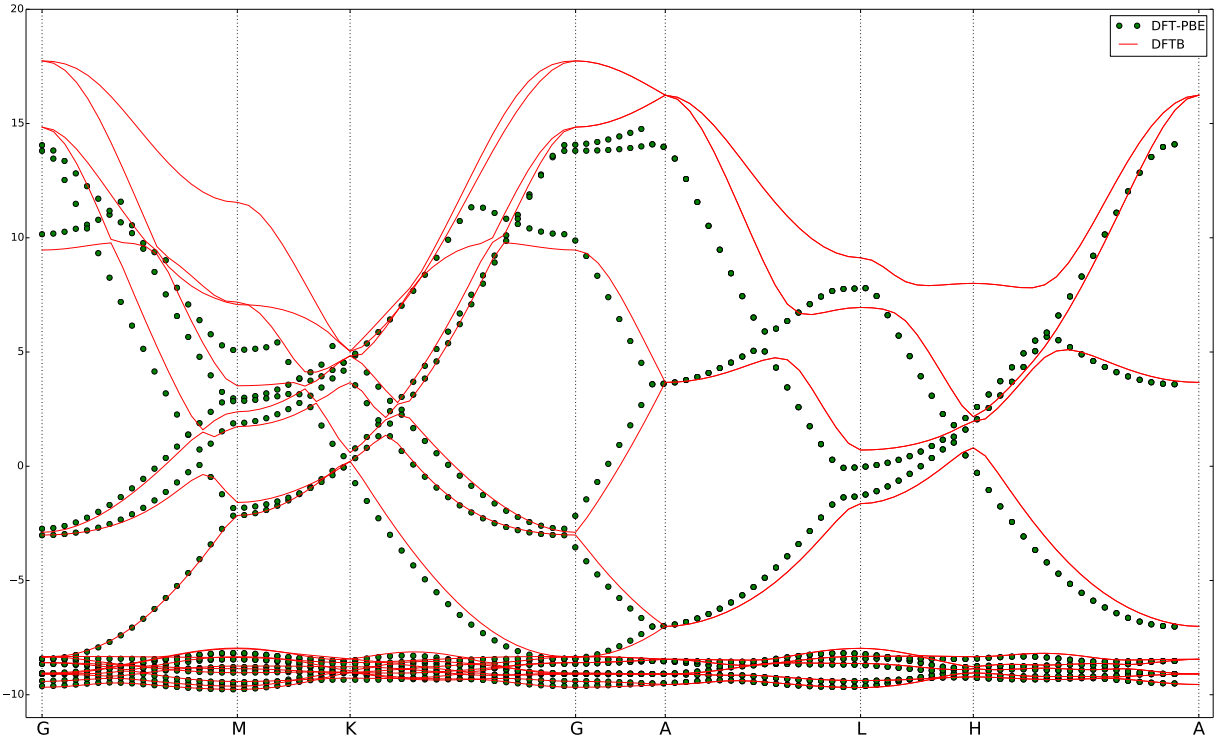

Figure 7: A comparison between a DFTB obtained band structure (with a value r_0=5.4 Bohr) and an ab-initio calculated one (DFT-PBE) for hcp-Cd along the high symmetry lines in the irreducible part of the first brillouin zone. All bands are shifted to give E_f a value of zero eV.

$$\min\left\{\sum_i |E'_{DFT,i} - E'_{BS,i} - E'_{rep,i}|^2\right\}, \tag{63}$$

with respect to a and b where $V'_{i,rep}(r) = a + b(r_i - r_{cut})$. These additional i points $V'_{i,rep}(r)$ can then be used as well in the fitting of $V'_{rep}(r)$. It is assumed, that $V'_{rep}(r)$ changes linearly as a function of the bond lengths, which is valid only for small changes in the bonding distances. Calculation of all the derivatives is done numerically by first calculating the energy curves by stretching/compressing all equal bonds with DFT and DFTB and then use finite differences for the derivatives. The M data points as a function of r were then used in a fitting process with a standard smoothing spline [3] by minimizing the quantity

$$S[V_{rep}(r)] = \sum_{i=1}^{M}\left(\frac{V'_{rep,i} - U(r_i)}{\sigma_i}\right)^2 + \lambda\int^{R_{cut}} U''(r)^2 dr\ , \tag{64}$$

where $U(r)$ is a cubic spline with its smoothness determined by the parameter λ and the weights for every data point σ_i. In addition one has to choose an R_{cut} at which V'_{rep} is set

equal to zero. The final repulsion potential E_{rep} is obtained by numerical integration of $V'_{rep}(r)$ up to R_{cut}

$$V_{rep}(r) = -\int_{R}^{R_{cut}} V'_{rep}(r)dr \ , \tag{65}$$

as it can be seen in figure 8 again for the case of cadmium.

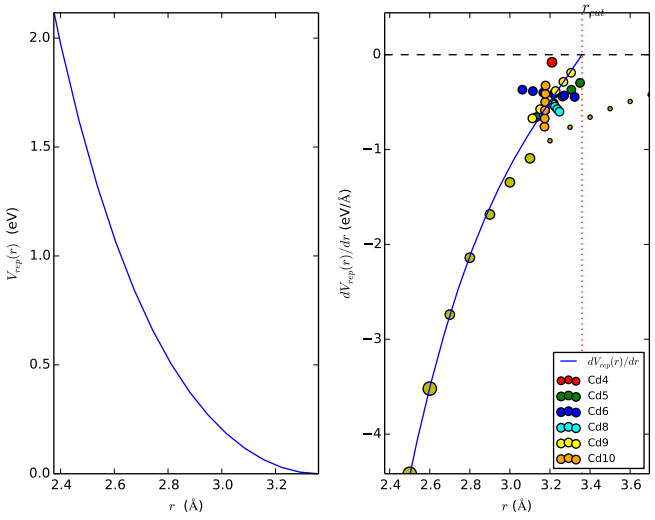

Figure 8: Calculation of the repulsion potential $V_{rep}(r)$ by minimizing the force differences between ab-initio DFT (PBE,Def2TZP basis set) and DFTB calculations for various cadmium clusters of different sizes (right plot). On the left side the resulting repulsive potential $V_{rep}(r)$ is shown. The size of every data point in the right plot i represents its weight in the fit with $\sigma \in [0,1]$.

13 The RGL potential

The empirical many-body potential introduced by Rosato, Guillope and Legrand [98] was developed to simulate thermodynamic properties of fcc metals and is based on the second moment approximation to the tight binding theory. Based on the work of Finnis and Sinclair [119] who proposed that the total energy of a many body system with N atoms can be written in the from

$$E_{tot} = E_m + E_R \ , \tag{66}$$

as the sum of a repulsive pair potential E_R and an attractive many-body potential E_m for all atoms N in a system. E_m is chosen to be of the form

$$E_m = -\sum_{i \neq j}^{N} \sqrt{\rho(r_{ij})} \ , \tag{67}$$

with the function ρ that depends only on the interatomic distance r_{ij} between two atoms i and j. It is assumed now, that the cohesive energy does not depend on the details of the density of states, but only on its effective width (= the second moment) [120, 121]. For an atom i with the neighboring atoms j in a lattice $\alpha\beta$ the bond energy E_m is then expressed as proposed by Gupta and Tomanek *et al.* as [122, 123]

$$E_m^i = -\left[\sum_j \xi_{\alpha\beta}^2 e^{-2q_{\alpha\beta}(r_{ij}/r_0^{\alpha\beta}-1)}\right]^{1/2} \ , \tag{68}$$

with r_{ij} being the distance between atoms i and j, $r_0^{\alpha\beta}$ being the first-neighbours distance in lattice $\alpha\beta$, ξ an effective hopping integral, while q describes its dependency on the interatomic distance. The second term E_R^i in eq.66 represents a repulsive pairwise interaction of Born-Mayer type to stabilize the system [98]

$$E_r^i = \sum_j A_{\alpha\beta} e^{-p_{\alpha\beta}(r_{ij}/r_0^{\alpha\beta}-1)} \ , \tag{69}$$

with p being related to the compressibility of the metal and A representing a repulsion. The summation over i and j in 68 and 69 is restricted to the Z next nearest neighbours only and then the following relations for $p_{\alpha\beta}$, $q_{\alpha\beta}$, $A_{\alpha\beta}$ and $\xi_{\alpha\beta}$ hold [120, 121]

$$\xi_{\alpha\beta} = \frac{p_{\alpha\beta}}{p_{\alpha\beta} - q_{\alpha\beta}} \frac{E_{tot}}{\sqrt{Z}} \ , \tag{70}$$

$$A_{\alpha\beta} = \frac{p_{\alpha\beta}}{p_{\alpha\beta} - q_{\alpha\beta}} \frac{E_{tot}}{Z} \ . \tag{71}$$

The parameters $p_{\alpha\beta}$, $q_{\alpha\beta}$, $A_{\alpha\beta}$ and $\xi_{\alpha\beta}$ are fitted to reproduce experimental values of cohesive energies, lattice parameters, bulk moduli and shear elastic constants. Fitting of these parameters to heteroatomic phases is more complicated as the optimum parameters are not simple equally weighted averages of the corresponding homoatomic parameters [124]. In general the RGL parameters are therefore fitted to several phases with different ratios of the elements (e.g. AB_2, AB_3) to ensure maximum transferability.

13.1 Parametrization of the RGL parameters

In case of non available experimental data the RGL parameters can also be fitted to ab-inito derived structural and mechanical properties. The density functional theory together

with the for solids re-parametrized version of the PBE functional (PBEsol) is a good choice as it gives in general a good agreement for structural and mechanical properties between experimental and theoretically predicted results [125]. For the later presented study in the Ag-Rh system the two $C1$ (Ag_2Rh, $AgRh_2$) and $L1_2$ phases (Ag_3Rh,$AgRh_3$) and the $B2$ phase ($AgRh$) were used during the fitting process. As there are no stable phases known from experiment because of positive heats of formations and mixing enthalpies over the whole Ag:Rh ratio all related values had to be extracted from DFT calculations. Accurate lattice constants for all phases were obtained by fitting the Murnaghan equation [126] to a plot of the total energy E versus the volume V as

$$E(V) = E_0 + \frac{B_0 V}{B_0^{'}}\left[\left(\frac{V_0}{V}\right)^{B_0^{'}}\frac{1}{B_0^{'}-1}+1\right] - \frac{B_0 V_0}{B_0^{'}-1}\ , \tag{72}$$

where E_0 is the total energy at the equilibrium Volume V_0, B_0 the bulk modulus at zero pressure and $B_0^{'}$ the derivative of the bulk modulus with respect to pressure. In principle it is possible to extract the bulk modulus B_0 from eq.72. However, there is a better way that will yield the elastic constants C_{11}, C_{12}, C_{44} at the same time. The internal energy of an elastic solid can be expanded in a Taylor series up to the second order about the unstrained cell for small deformations [127, 128]

$$E(V,\varepsilon_k) = E_0 + V_0\left(\sum_{i=1}^{6}\sigma_i\varepsilon_i + \frac{1}{2}\sum_{i,j=1}^{6}C_{ij}\varepsilon_i\varepsilon_j\right) \tag{73}$$

where $\{\varepsilon_k\}$ denotes $\{\varepsilon_1, \varepsilon_2, ...\varepsilon_6\}$, V_0 and E_0 are the volume and the energy of the unstrained cell. Elastic constants are then calculated by taking the second-order partial derivative of eq.73 for both volumetric and distortional deformations with respect to strains, evaluated at zero strain:

$$C_{ij} = \frac{1}{V_0}\left[\frac{\partial^2 E}{\partial\varepsilon_i\partial\varepsilon_j}\right]_{\{\varepsilon_k\}=0} \tag{74}$$

Three distortion matrices D_{ortho}, D_{cubic}, D_{monoc} are used to distort the unstrained cell with the basis vectors R_{fcc} to give the distorted basis vectors $R^{'}$ from $R \rightarrow R^{'}_{dist} = RD_{dist}$ with

$$R_{fcc} = \frac{a}{2}\begin{pmatrix}0 & 1 & 1\\ 1 & 0 & 1\\ 1 & 1 & 0\end{pmatrix}\ \text{, and}$$

$$D_{ortho} = \begin{bmatrix} 1+\varepsilon & 1 & 1 \\ 1 & 1-\varepsilon & 1 \\ 0 & 0 & \frac{1}{1-\varepsilon^2} \end{bmatrix} \quad , D_{cubic} = \begin{bmatrix} 1+\varepsilon & 1 & 1 \\ 1 & 1+\varepsilon & 1 \\ 0 & 0 & 1+\varepsilon \end{bmatrix} \quad ,$$

$$D_{monoc} = \begin{bmatrix} 1 & \varepsilon & 1 \\ \varepsilon & 1 & 1 \\ 0 & 0 & \frac{1}{1-\varepsilon^2} \end{bmatrix} \quad .$$

The change in energy due to the deformations of the cell can be described with the following equations:

$$E_{ortho}(V,\varepsilon) = E_0 + V_0\Big\{(C_{11}-C_{12})\varepsilon^2 + O(\varepsilon^4)\Big\} \ , \tag{75}$$

$$E_{cubic}(V,\varepsilon) = E_0 + V_0\varepsilon(\sigma_1+\sigma_2+\sigma_3) + V_0\Big\{\frac{3}{2}(C_{11}-2C_{12})\varepsilon^2 + O(\varepsilon^3)\Big\} \ , \tag{76}$$

and

$$E_{monoc}(V,\varepsilon) = E_0 + V_0\Big\{(2C_{44})\varepsilon^2 + O(\varepsilon^4)\Big\} \ . \tag{77}$$

which gives the second-order derivatives of the energy evaluated at zero strain as

$$\frac{d^2E}{d\varepsilon^2} = 2V_0(C_{11}-C_{12}) = \eta_1 \ , \tag{78}$$

$$\frac{d^2E}{d\varepsilon^2} = 3V_0(C_{11}-2C_{12}) = \eta_2 \ , \tag{79}$$

$$\frac{d^2E}{d\varepsilon^2} = 4V_0C_{44} \ . \tag{80}$$

Equations 75 to 77 were fitted with a polynomial of third order and the numerical second derivative with respect to zero strain was calculated and afterwards the resulting two linear equations solved to calculate C_{11} and C_{12}. The bulk modulus B_0 can finally be calculated from the relation

$$B_0 = \frac{1}{3}\big(C_{11}+2C_{12}\big) \ . \tag{81}$$

To get the optimum RGL parameters we now minimize the difference between the DFT calculated properties and the ones obtained from using the RGL approach for all phases k described by the following equation with the weights w_k, the elastic constants C_{ij} and

the lattice constants a_k:

$$\min\Bigg\{ \sum_k \sum_{ij} w_{C_{ij,k}} \frac{|C_{ij,k}^{DFT} - C_{ij,k}^{RGL}|}{C_{ij,k}^{DFT}} + \sum_k w_{a,k} \frac{|a_k^{DFT} - a_k^{RGL}|}{a_k^{DFT}} + \sum_k w_{B_0 k} \frac{|B_{0,k}^{DFT} - B_{0,k}^{RGL}|}{B_{0,k}^{DFT}} \Bigg\} . \quad (82)$$

For the minimization of that equation the simplex algorithm was used starting from RGL parameters $\{p, q, A, \xi\}$ that where calculated as fractions from the parameters of the pure clusters as

$$RGL_{start} = xRGL_{Rh} + (1-x)RGL_{Ag} \quad x \in \{0.1, 0.2, 0.3, ..., 0.9\} . \quad (83)$$

The set of parameters, that gave the lowest error for all the elastic and structural properties in comparison to the DFT calculated ones were then used in the first study on the "Structural, energetic, and magnetic properties of $Ag_{n-m}Rh_m$ and Ag_mRh_{n-m} clusters with $n \leq 20$ and $m = 0, 1$"

References

[1] S. R. Bahn and K. W. Jacobsen. An object-oriented scripting interface to a legacy electronic structure code. Comput. Sci. Eng., 4(3):56–66, MAY-JUN 2002.

[2] V. Vanovschi. Parallelpython. http://www.parallelpython.com/.

[3] Pekka Koskinen and Ville Mäkinen. Density-functional tight-binding for beginners. Computational Materials Science, 47(1):237 – 253, 2009.

[4] J. Schiøtz. Asap3. https://wiki.fysik.dtu.dk/asap/asap.

[5] Paul F. Dubois, Konrad Hinsen, and James Hugunin. Numerical python. Computers in Physics, 10(3), May/June 1996.

[6] José M Soler, Emilio Artacho, Julian D Gale, Alberto García, Javier Junquera, Pablo Ordejón, and Daniel SÃ¡nchez-Portal. The SIESTA method for ab-initio order-N materials simulation. Journal of Physics: Condensed Matter, 14(11):2745, 2002.

[7] Alexander Stukowski. Visualization and analysis of atomistic simulation data with ovito the open visualization tool. Modelling and Simulation in Materials Science and Engineering, 18(1):015012, 2010.

[8] Alexander Stukowski. Structure identification methods for atomistic simulations of crystalline materials. Modelling and Simulation in Materials Science and Engineering, 20(4):045021, 2012.

[9] D. J. Norris and M. G. Bawendi. Measurement and assignment of the size-dependent optical spectrum in CdSe quantum dots. Phys. Rev. B, 53:16338–16346, Jun 1996.

[10] Aneta J. Mieszawska, Willem J. M. Mulder, Zahi A. Fayad, and David P. Cormode. Multifunctional gold nanoparticles for diagnosis and therapy of disease. Molecular Pharmaceutics, 10(3):831–847, 2013. PMID: 23360440.

[11] Minakshi Das, Kyu Hwan Shim, Seong Soo A. An, and Dong Kee Yi. Review on gold nanoparticles and their applications. Toxicol. Environ. Health Sci., 3:193, 2011.

[12] K. Lance Kelly, Eduardo Coronado, Lin Lin Zhao, and George C. Schatz. The Optical Properties of Metal Nanoparticles: The Influence of Size, Shape, and Dielectric Environment. The Journal of Physical Chemistry B, 107(3):668–677, 2003.

[13] Jia-Wei Shiu, Zih-Jian Lan, Chien-Yi Chan, Hui-Ping Wu, and Eric Wei-Guang Diau. Construction of a photoanode with varied TiO_2 nanostructures for a z907-sensitized solar cell with efficiency exceeding 10%. J. Mater. Chem. A, 2:8749–8757, 2014.

[14] John D. Aiken III and Richard G. Finke. A review of modern transition-metal nanoclusters: Their synthesis, Characterization, and applications in Catalysis. Journal of Molecular Catalysis A: Chemical, 145(12):1 – 44, 1999.

[15] Jonathan P. K. Doye. Identifying structural patterns in disordered metal clusters. Phys. Rev. B, 68:195418, Nov 2003.

[16] David J. Wales and Jonathan P. K. Doye. Global optimization by Basin-Hopping and the Lowest Energy Structures of Lennard-Jones Clusters Containing up to 110 Atoms. The Journal of Physical Chemistry A, 101(28):5111–5116, 1997.

[17] G. J. Ackland and A. P. Jones. Applications of local crystal structure measures in experiment and simulation. Phys. Rev. B, 73:054104, Feb 2006.

[18] Waldemar Hellmann, R. G. Hennig, Stefan Goedecker, C. J. Umrigar, Bernard Delley, and T. Lenosky. Questioning the existence of a unique ground-state structure for Si clusters. Phys. Rev. B, 75:085411, Feb 2007.

[19] Ho, Kai-Ming, Shvartsburg, Alexandre A., Pan, Bicai, Lu, Zhong-Yi, Wang, Cai-Zhuang, Wacker, Jacob G., Fye, James L., and Jarrold, Martin F. Structures of medium-sized silicon clusters. Nature, 392(6676):582–585, apr 1998. 10.1038/33369.

[20] Habib ur Rehman, Michael Springborg, and Yi Dong. Structural and electronic properties of Si_n, Ge_n, and Si_nGe_n clusters. The Journal of Physical Chemistry A, 115(10):2005–2015, 2011. PMID: 21338159.

[21] MiguelAngel Gracia-Pinilla, Domingo Ferrer, Sergio Mejia-Rosales, and Eduardo Perez-Tijerina. Size-selected Ag nanoparticles with Five-Fold Symmetry. Nanoscale Res. Lett., 4:896–902, 2009.

[22] Martine N. Blom, Detlef Schooss, Jason Stairs, and Manfred M. Kappes. Experimental structure determination of silver cluster ions (Ag_n^+,$19 \leq n \leq 79$). J. Chem. Phys., 124, 2006.

[23] Detlef Schooss, Martine N. Blom, Joel H. Parks, Bernd v. Issendorff, Hellmut Haberland, and Manfred M. Kappes. The structures of Ag_{55}^+ and Ag_{55}^-: trapped ion

electron diffraction and density functional theory. Nano Letters, 5(10):1972–1977, 2005. PMID: 16218720.

[24] Young-Cho Bae, Hiroki Osanai, Vijay Kumar, and Yoshiyuki Kawazoe. Nonicosahedral growth and magnetic behavior of rhodium clusters. Phys. Rev. B, 70:195413, 2004.

[25] Young-Cho Bae, Vijay Kumar, Hiroki Osanai, and Yoshiyuki Kawazoe. Cubic magic clusters of rhodium stabilized with eight-center bonding: Magnetism and growth. Phys. Rev. B, 72:125427, 2005.

[26] J. P. Chou, H. Y. T. Chen, C. R. Hsing, C. M. Chang, C. Cheng, and C. M. Wei. 13-atom metallic clusters studied by density functional theory: Dependence on exchange-correlation approximations and pseudopotentials. Phys. Rev. B, 80:165412, 2009.

[27] Maurício J. Piotrowski, Paulo Piquini, and Juarez L. F. Da Silva. Density functional theory investigation of 3d, 4d, and 5d 13-atom metal clusters. Phys. Rev. B, 81:155446, Apr 2010.

[28] J P Chou, C R Hsing, C M Wei, C Cheng, and C M Chang. Ab initio random structure search for 13-atom clusters of fcc elements. J. Phys. Cond. Matt., 25:125305, 2013.

[29] A. Debski, R. Debski, and W. Gasior. New features of entall database: Comparison of experimental and model formation enthalpies. Arch. Metal. Mater., 59:1337–1343, 2014.

[30] Fabio R. Negreiros, Zdenka Kuntová, Giovanni Barcaro, Giulia Rossi, Riccardo Ferrando, and Alessandro Fortunelli. Structures of gas-phase Ag-Pd nanoclusters: A computational study. The Journal of Chemical Physics, 132(23):234703, 2010.

[31] Giulia Rossi, Riccardo Ferrando, Arnaldo Rapallo, Alessandro Fortunelli, Benjamin C. Curley, Lesley D. Lloyd, and Roy L. Johnston. Global optimization of bimetallic cluster structures. ii. size-matched Ag-Pd, Ag-Au, and Pd-Pt systems. The Journal of Chemical Physics, 122(19), 2005.

[32] Mohammad Molayem, Valeri G. Grigoryan, and Michael Springborg. Theoretical determination of the most stable structures of Ni_mAg_n bimetallic nanoalloys. The Journal of Physical Chemistry C, 115(15):7179–7192, 2011.

[33] M. Harb, F. Rabilloud, and D. Simon. Density Functional Study of Structural and Electronic Properties of Small Bimetallic Silver-Nickel Clusters. The Journal of Physical Chemistry A, 111(32):7726–7731, 2007. PMID: 17637046.

[34] Mohammad Molayem, Valeri G. Grigoryan, and Michael Springborg. Global minimum structures and magic clusters of Cu_mAg_n nanoalloys. The Journal of Physical Chemistry C, 115(45):22148–22162, 2011.

[35] Ewald Janssens, Thibaut Van Hoof, Nele Veldeman, Sven Neukermans, Marc Hou, and Peter Lievens. Mass spectrometric and modeling investigations of bimetallic Silver-Cobalt clusters. International Journal of Mass Spectrometry, 252(1):38 – 46, 2006.

[36] F. Aguilera-Granja, J. L. Rodríguez-López, K. Michaelian, E. O. Berlanga-Ramírez, and A. Vega. Structure and magnetism of small rhodium clusters. Phys. Rev. B, 66:224410, 2002.

[37] Yuanyuan Jin, Yonghong Tian, Xiaoyu Kuang, Chuanzhao Zhang, Cheng Lu, Jingjing Wang, Jian Lv, Liping Ding, and Meng Ju. Ab Initio Search for Global Minimum Structures of Pure and Boron Doped Silver Clusters. J. Phys. Chem. A, 119:6738–6745, 2015.

[38] René Fournier. Theoretical study of the structure of silver clusters. J. Chem. Phys., 115:21652177, 2001.

[39] Gabriel U. Gamboa, Arthur C. Reber, and Shiv N. Khanna. Electronic subshell splitting controls the atomic structure of charged and neutral silver clusters. New J. Chem., 37:39283935, 2013.

[40] A. Christensen, A. V. Ruban, P. Stoltze, K. W. Jacobsen, H. L. Skriver, J. K. Nørskov, and F. Besenbacher. Phase diagrams for surface alloys. Phys. Rev. B, 56:5822–5834, 1997.

[41] E. Janssens, S. Neukermans, H. M. T. Nguyen, M. T. Nguyen, and P. Lievens. Quenching of the magnetic moment of a transition metal dopant in silver clusters. Phys. Rev. Lett., 94:113401, Mar 2005.

[42] Ruibin Dong, Xiaoshuang Chen, Huxian Zhao, Xiaofang Wang, Haibo Shu, Zonglin Ding, and Lu Wei. Structural, electronic and magnetic properties of Ag_nFe clusters ($n \leq 15$): local magnetic moment interacting with delocalized electrons. J. Phys. B, 44:035102, 2011.

[43] Maik Eichelbaum, Klaus Rademann, Ralf Müller, Martin Radtke, Heinrich Riesemeier, and Wolf Grner. On the chemistry of gold in silicate glasses: Studies on a non-thermally activated growth of gold nanoparticles. Angewandte Chemie International Edition, 44(48):7905–7909, 2005.

[44] Kohei Kusada, Miho Yamauchi, Hirokazu Kobayashi, Hiroshi Kitagawa, and Yoshiki Kubota. Hydrogen-storage properties of Solid-Solution Alloys of Immiscible Neighboring Elements with Pd. J. Am. Chem. Soc., 132:15896–15898, 2010.

[45] Stephany Garcia, Liang Zhang, Graham W. Piburn, Graeme Henkelman, and Simon M. Humphrey. Microwave Synthesis of Classically Immiscible Rhodium-Silver and Rhodium-Gold Alloy Nanoparticles: Highly Active Hydrogenation Catalysts. ACS Nano, 8:11512–11521, 2014.

[46] Walt A. de Heer. The physics of simple metal clusters: experimental aspects and simple models. Rev. Mod. Phys., 65:611–676, Jul 1993.

[47] Riccardo Ferrando, Julius Jellinek, and Roy L. Johnston. Nanoalloys: From theory to applications of alloy clusters and nanoparticles. Chemical Reviews, 108(3):845–910, 2008. PMID: 18335972.

[48] Anne Lechtken, Christian Neiss, Manfred M. Kappes, and Detlef Schooss. Structure determination of gold clusters by trapped ion electron diffraction: Au_{14}^--Au_{19}^-. Phys. Chem. Chem. Phys., 11:4344–4350, 2009.

[49] Christian Neiss and Detlef Schooss. Accelerated cluster structure search using electron diffraction data in a genetic algorithm. Chemical Physics Letters, 532:119 – 123, 2012.

[50] Lingxuan Peng, Emilie Ringe, Richard P. Van Duyne, and Laurence D. Marks. Segregation in bimetallic nanoparticles. Phys. Chem. Chem. Phys., 17:27940–27951, 2015.

[51] T.P. Martin. Shells of atoms. Physics Reports, 273(4):199 – 241, 1996.

[52] F. Baletto, C. Mottet, and R. Ferrando. Microscopic mechanisms of the growth of metastable silver icosahedra. Phys. Rev. B, 63:155408, Mar 2001.

[53] Jonathan P. K. Doye, Mark A. Miller, and David J. Wales. The double-funnel energy landscape of the 38-atom Lennard-Jones cluster. The Journal of Chemical Physics, 110(14):6896–6906, 1999.

[54] Amendra Fernando, K. L. Dimuthu M. Weerawardene, Natalia V. Karimova, and Christine M. Aikens. Quantum mechanical studies of large metal, metal oxide, and metal chalcogenide nanoparticles and clusters. Chemical Reviews, 115(12):6112–6216, 2015. PMID: 25898274.

[55] Hans Bock. Fundamentals of silicon chemistry: Molecular states of silicon-containing compounds. Angewandte Chemie International Edition in English, 28(12):1627–1650, 1989.

[56] Kennedy Eberhart. A new optimizer using particle swarm theory. In Proceedings of the sixth international symposium on micro machine and human science, pages 39–43, 1995.

[57] Dervis Karaboga and Bahriye Basturk. A powerful and efficient algorithm for numerical function optimization: artificial bee colony (abc) algorithm. Journal of Global Optimization, 39(3):459–471, 2007.

[58] Scott Kirkpatrick. Optimization by simulated annealing: Quantitative studies. Journal of Statistical Physics, 34(5-6):975–986, 1984.

[59] D. M. Deaven and K. M. Ho. Molecular geometry optimization with a genetic algorithm. Phys. Rev. Lett., 75:288–291, Jul 1995.

[60] Sven Heiles and Roy L. Johnston. Global optimization of clusters using electronic structure methods. International Journal of Quantum Chemistry, 113(18):2091–2109, 2013.

[61] S.M. Woodley and C.R.A. Catlow. Structure prediction of titania phases: Implementation of darwinian versus lamarckian concepts in an evolutionary algorithm. Computational Materials Science, 45(1):84–95, 2009. Selected papers from the E-MRS 2007 Fall Meeting Symposium G: Genetic Algorithms in Materials Science and EngineeringGAMS-2007.

[62] G.W. Turner, E. Tedesco, K.D.M. Harris, R.L. Johnston, and B.M. Kariuki. Implementation of lamarckian concepts in a genetic algorithm for structure solution from powder diffraction data. Chemical Physics Letters, 321(3-4):183–190, 2000. cited By 85.

[63] Roy L. Johnston. Evolving better nanoparticles: Genetic algorithms for optimising cluster geometries. Dalton Trans., pages 4193–4207, 2003.

[64] David E. Goldberg and Kalyanmoy Deb. A comparative analysis of selection schemes used in genetic algorithms. In Foundations of Genetic Algorithms, pages 69–93. Morgan Kaufmann, 1991.

[65] Thomas Baeck and Frank Hoffmeister. Extended selection mechanisms in genetic algorithms. 1991.

[66] Tobias Blickle and Lothar Thiele. A comparison of selection schemes used in genetic algorithms. Technical report, Gloriastrasse 35, CH-8092 Zurich: Swiss Federal Institute of Technology (ETH) Zurich, Computer Engineering and Communications Networks Lab (TIK, 1995.

[67] Matthew D. Wolf and Uzi Landman. Genetic algorithms for structural cluster optimization. The Journal of Physical Chemistry A, 102(30):6129–6137, 1998.

[68] Mark T. Oakley, Roy L. Johnston, and David J. Wales. Symmetrisation schemes for global optimisation of atomic clusters. Phys. Chem. Chem. Phys., 15:3965–3976, 2013.

[69] Gustavo G. Rondina and Juarez L. F. Da Silva. Revised basin-hopping Monte Carlo algorithm for structure optimization of clusters and nanoparticles. Journal of Chemical Information and Modeling, 53(9):2282–2298, 2013. PMID: 23957311.

[70] AP. Sutton and J. Chen. Long-range Finnis-Sinclair potentials. Philosophical Magazine Letters, 61(3):139–146, 1990.

[71] Thomas Weise, Raymond Chiong, and Ke Tang. Evolutionary optimization: Pitfalls and booby traps. Journal of Computer Science and Technology, 27(5):907–936, 2012.

[72] Bernd Hartke. Global cluster geometry optimization by a phenotype algorithm with niches: Location of elusive minima, and low-order scaling with cluster size. Journal of Computational Chemistry, 20(16):1752–1759, 1999.

[73] Longjiu Cheng, Wensheng Cai, and Xueguang Shao. A connectivity table for cluster similarity checking in the evolutionary optimization method. Chemical Physics Letters, 389(46):309 – 314, 2004.

[74] J. Dana Honeycutt and Hans C. Andersen. Molecular dynamics study of melting and freezing of small Lennard-Jones clusters. The Journal of Physical Chemistry, 91(19):4950–4963, 1987.

[75] Mark Dittner and Bernd Hartke. Conquering the hard cases of Lennard-Jones clusters with simple recipes. Computational and Theoretical Chemistry, pages –, 2016. http://dx.doi.org/10.1016/j.comptc.2016.09.032.

[76] Bernhard Bandow and Bernd Hartke. Larger Water Clusters with Edges and Corners on Their Way to Ice: Structural Trends Elucidated with an Improved Parallel Evolutionary Algorithm. The Journal of Physical Chemistry A, 110(17):5809–5822, 2006. PMID: 16640376.

[77] A. Shayeghi, D. Götz, J. B. A. Davis, R. Schäfer, and R. L. Johnston. Pool-BCGA: A parallelised generation-free genetic algorithm for the ab–initio global optimisation of nanoalloy clusters. Phys. Chem. Chem. Phys., 17:2104–2112, 2015.

[78] Erik Bitzek, Pekka Koskinen, Franz Gähler, Michael Moseler, and Peter Gumbsch. Structural relaxation made simple. Phys. Rev. Lett., 97:170201, Oct 2006.

[79] Ralf Gehrke and Karsten Reuter. Assessing the efficiency of first-principles Basin-Hopping sampling. Phys. Rev. B, 79:085412, 2009.

[80] Jan-Ole Joswig. Theoretical Studies of Properties of Clusters. PhD thesis, 2003.

[81] Adam Lipowski and Dorota Lipowska. Roulette-wheel selection via stochastic acceptance. Physica A: Statistical Mechanics and its Applications, 391(6):2193 – 2196, 2012.

[82] J. E. Jones. On the Atomic Fields of Helium and Neon. Proceedings of the Royal Society of London A: Mathematical, Physical and Engineering Sciences, 107(741):157–170, 1925.

[83] Johannes M. Dieterich and Bernd Hartke. Composition-induced structural transitions in mixed Lennard-Jones clusters: Global reparametrization and optimization. Journal of Computational Chemistry, 32(7):1377–1385, 2011.

[84] D. J. Wales, J. P. K. Doye, and A. Dullweber. The Cambridge Cluster Database. http://www-wales.ch.cam.ac.uk/CCD.html.

[85] Andriy O. Lyakhov, Artem R. Oganov, Harold T. Stokes, and Qiang Zhu. New developments in evolutionary structure prediction algorithm {USPEX}. Computer Physics Communications, 184(4):1172 – 1182, 2013.

[86] Artem R. Oganov and Mario Valle. How to quantify energy landscapes of solids. The Journal of Chemical Physics, 130(10):104504, 2009.

[87] Valeri G Grigoryan and Michael Springborg. Structure and energetics of Ni clusters with up to 150 atoms. Chemical Physics Letters, 375(12):219 – 226, 2003.

[88] José Rogan, Alejandro Varas, Juan Alejandro Valdivia, and Miguel Kiwi. A strategy to find minimal energy nanocluster structures. Journal of Computational Chemistry, 34(29):2548–2556, 2013.

[89] Guillermo Avendao-Franco and Aldo H. Romero. Firefly algorithm for structural search. Journal of Chemical Theory and Computation, 12(7):3416–3428, 2016. PMID: 27232694.

[90] Jun Zhang and Michael Dolg. ABCluster: The artificial bee colony algorithm for cluster global optimization. Phys. Chem. Chem. Phys., 17:24173–24181, 2015.

[91] Mikail Aslan, Jack B. A. Davis, and Roy L. Johnston. Global optimization of small bimetallic Pd-Co binary nanoalloy clusters: A genetic algorithm approach at the DFT level. Phys. Chem. Chem. Phys., 18:6676–6682, 2016.

[92] Jack B. A. Davis, Sarah L. Horswell, and Roy L. Johnston. Application of a parallel genetic algorithm to the global optimization of gas-phase and supported goldiridium sub-nanoalloys. The Journal of Physical Chemistry C, 120(7):3759–3765, 2016.

[93] Jack B. A. Davis, Armin Shayeghi, Sarah L. Horswell, and Roy L. Johnston. The birmingham parallel genetic algorithm and its application to the direct DFT global optimisation of irn (n = 10-20) clusters. Nanoscale, 7:14032–14038, 2015.

[94] Heider A. Hussein, Jack B. A. Davis, and Roy L. Johnston. DFT global optimisation of gas-phase and MgO-supported sub-nanometre AuPd clusters. Phys. Chem. Chem. Phys., 18:26133–26143, 2016.

[95] Fernando Buendia, Jorge A. Vargas, Marcela R. Beltran, Jack B. A. Davis, and Roy L. Johnston. A comparative study of Au_mRh_n ($4 \leq m + n \leq 6$) clusters in the gas phase versus those deposited on (100) MgO. Phys. Chem. Chem. Phys., 18:22122–22128, 2016.

[96] Christopher J. Heard, Sven Heiles, Stefan Vajda, and Roy L. Johnston. $Pd_nAg_{(4-n)}$ and $pd_npt_{(4-n)}$ clusters on MgO (100): A Density Functional surface genetic algorithm investigation. Nanoscale, 6:11777–11788, 2014.

[97] Jack B. A. Davis, Sarah L. Horswell, and Roy L. Johnston. Global optimization of 8-10 atom Palladium-Iridium nanoalloys at the DFT level. The Journal of Physical Chemistry A, 118(1):208–214, 2014. PMID: 24328270.

[98] V. Rosato, M. Guillope, and B. Legrand. Thermodynamical and structural properties of f.c.c. transition metals using a simple tight-binding model. Phil. Mag. A, 59:321–336, 1989.

[99] Murray S. Daw and M. I. Baskes. Embedded-atom method: Derivation and application to impurities, surfaces, and other defects in metals. Phys. Rev. B, 29:6443–6453, Jun 1984.

[100] K.W. Jacobsen, P. Stoltze, and J.K. Nørskov. A semi-empirical effective medium theory for metals and alloys. Surface Science, 366(2):394 – 402, 1996.

[101] Donald W. Brenner. Empirical potential for hydrocarbons for use in simulating the chemical vapor deposition of diamond films. Phys. Rev. B, 42:9458–9471, Nov 1990.

[102] J. Tersoff. New empirical approach for the structure and energy of covalent systems. Phys. Rev. B, 37:6991–7000, Apr 1988.

[103] G. Seifert, D. Porezag, and Th. Frauenheim. Calculations of molecules, clusters, and solids with a simplified LCAO-DFT-LDA scheme. Int. J. Quant. Chem., 58:185–192, 1996.

[104] P. Hohenberg and W. Kohn. Inhomogeneous electron gas. Phys. Rev., 136:B864–B871, Nov 1964.

[105] Elliott H. Lieb. Thomas-fermi and related theories of atoms and molecules. Rev. Mod. Phys., 53:603–641, Oct 1981.

[106] Edward Teller. On the stability of molecules in the Thomas-Fermi theory. Rev. Mod. Phys., 34:627–631, Oct 1962.

[107] John P. Perdew and Karla Schmidt. Jacobs ladder of density functional approximations for the exchange-correlation energy. AIP Conference Proceedings, 577(1):1–20, 2001.

[108] Dmitrij Rappoport, Nathan R. M. Crawford, Filipp Furche, and Kieron Burke. Approximate Density Functionals: Which Should I Choose? John Wiley & Sons, Ltd, 2006.

[109] P. A. M. Dirac. Note on Exchange Phenomena in the Thomas Atom. 26(3):376–385, 007 1930.

[110] John P. Perdew and Yue Wang. Accurate and simple analytic representation of the electron-gas correlation energy. Phys. Rev. B, 45:13244–13249, Jun 1992.

[111] S. H. Vosko, L. Wilk, and M. Nusair. Accurate spin-dependent electron liquid correlation energies for local spin density calculations: a critical analysis. Canadian Journal of Physics, 58(8):1200–1211, 1980.

[112] D. M. Ceperley and B. J. Alder. Ground state of the electron gas by a stochastic method. Phys. Rev. Lett., 45:566–569, Aug 1980.

[113] Paul Ziesche, Stefan Kurth, and John P. Perdew. Density functionals from LDA to GGA. Computational Materials Science, 11(2):122 – 127, 1998.

[114] D. Porezag, Th. Frauenheim, Th. Köhler, G. Seifert, and R. Kaschner. Construction of tight-binding-like potentials on the basis of density-functional theory: Application to carbon. Phys. Rev. B, 51:12947–12957, May 1995.

[115] M. Elstner, D. Porezag, G. Jungnickel, J. Elsner, M. Haugk, Th. Frauenheim, S. Suhai, and G. Seifert. Self-consistent-charge density-functional tight-binding method for simulations of complex materials properties. Phys. Rev. B, 58:7260–7268, Sep 1998.

[116] Guishan Zheng, Henryk A. Witek, Petia Bobadova-Parvanova, Stephan Irle, Djamaladdin G. Musaev, Rajeev Prabhakar, Keiji Morokuma, Marcus Lundberg, Marcus Elstner, Christof Köhler, and Thomas Frauenheim. Parameter Calibration of Transition-Metal Elements for the Spin-Polarized Self-Consistent-Charge Density-Functional Tight-Binding (DFTB) method: Sc, Ti, Fe, Co, and Ni. Journal of Chemical Theory and Computation, 3(4):1349–1367, 2007. PMID: 26633208.

[117] H. Fox, K. E. Newman, W. F. Schneider, and S. A. Corcelli. Bulk and surface properties of rutile TiO_2 from Self-Consistent-Charge Density Functional Tight Binding. Journal of Chemical Theory and Computation, 6(2):499–507, 2010. PMID: 26617305.

[118] J. C. Slater and G. F. Koster. Simplified LCAO method for the Periodic Potential Problem. Phys. Rev., 94:1498–1524, Jun 1954.

[119] M. W. Finnis and J. E. Sinclair. A simple empirical n-body potential for transition metals. Philosophical Magazine A, 50(1):45–55, 1984.

[120] F. Ducastelle and F. Cyrot-Lackmann. Moments developments. Journal of Physics and Chemistry of Solids, 32(1):285 – 301, 1971.

[121] G. Allan. Relaxation and force constants near fcc transition metal surfaces. Surface Science, 89(1):142 – 150, 1979.

[122] Raju P. Gupta. Lattice relaxation at a metal surface. Phys. Rev. B, 23:6265–6270, 1981.

[123] D. Tománek, A. A. Aligia, and C. A. Balseiro. Calculation of elastic strain and electronic effects on surface segregation. Phys. Rev. B, 32:5051–5056, Oct 1985.

[124] Ramli Ismail and Roy L. Johnston. Investigation of the structures and chemical ordering of small Pd-Au clusters as a function of composition and potential parameterisation. Phys. Chem. Chem. Phys., 12:8607–8619, 2010.

[125] John P. Perdew, Adrienn Ruzsinszky, Gábor I. Csonka, Oleg A. Vydrov, Gustavo E. Scuseria, Lucian A. Constantin, Xiaolan Zhou, and Kieron Burke. Restoring the density-gradient expansion for exchange in solids and surfaces. Phys. Rev. Lett., 100:136406, Apr 2008.

[126] F. D. Murnaghan. The compressibility of media under extreme pressures. PNAS, 30(9):244–247, 1944.

[127] R. Stadler, W. Wolf, R. Podloucky, G. Kresse, J. Furthmüller, and J. Hafner. *Ab-initio* calculations of the cohesive, elastic, and dynamical properties of $CoSi_2$ by pseudopotential and all-electron techniques. Phys. Rev. B, 54:1729–1734, Jul 1996.

[128] M. Jamal, S. Jalali Asadabadi, Iftikhar Ahmad, and H. A. Rahnamaye Aliabad. Elastic constants of cubic crystals. Comp. Mat. Sci., 95:592 – 599, 2014.

Part III

Results and Discussion

The results and discussion are published in the following articles and are in the order:

1. S. Kohaut and M. Springborg: *"Growth patterns and structural motifs of cadmium clusters with up to 60 atoms: disordered or not?"*, Phys. Chem. Chem. Phys. (2016) **18**:28524 - **"Reproduced by permission of the PCCP Owner Societies"**

2. S. Kohaut, P. Thiel, M. Springborg: *"Growth patterns, shapes, and electronic properties of mixed Si_mGe_n clusters with $n + m = 30$"* Computational & Theoretical Chemistry (2016), Accepted,**"Reprinted with permission of Elsevier"**

3. S. Kohaut and M. Springborg:*"Structural, Energetic, and Magnetic Properties of $Ag_{n-m}Rh_m$ and Ag_mRh_{n-m} Clusters with $n \leq 20$ and $m = 0, 1$"*, J. Clust. Sci. (2016) **27**:913933 - **"With permission of Springer"**

PCCP

PAPER

View Article Online
View Journal | View Issue

Published on 13 September 2016. Downloaded by Universitat des Saarlandes on 17/12/2016 20:46:23.

Cite this: *Phys. Chem. Chem. Phys.*, 2016, **18**, 28524

Growth patterns and structural motifs of cadmium clusters with up to 60 atoms: disordered or not?†

Stephan Kohaut[a] and Michael Springborg*[ab]

Received 15th July 2016,
Accepted 13th September 2016

DOI: 10.1039/c6cp04948f

www.rsc.org/pccp

Using two different approaches, the structures of Cd_n clusters are optimized. At first, parameterized density-functional calculations using the DFTB method in combination with evolutionary algorithms provide one set of candidate structures. Second, earlier proposed structures based on the Gupta potential provide a second set. Subsequently, all structures of each set are re-optimized using parameter-free density-functional calculations. It turned out that those based on the DFTB calculations in almost all cases were those of the lowest total energy. By analysing the structural properties as a function of cluster size information on growth patterns can be extracted. Thereby, the results show a certain preference that the atoms of the inner parts have surroundings as found in bulk hcp Cd. Furthermore, for larger size ranges, we could identify a specific growth pattern, implying that most of these clusters cannot be classified as being disordered. The results show also that the 4d electrons have only a weak influence on the properties of the clusters that, however, is so strong that a jellium-like model occasionally becomes inaccurate in describing the properties. In particular, the question at which size the clusters can be considered to be metallic becomes non-trivial to answer. Further arguments based on a comparison of the HOMO–LUMO gaps with the Kubo gap, however, suggested the non-metallic properties in the studied size range.

1 Introduction

Small to medium-sized clusters, especially of metals, are known to acquire structural motifs that do not only show local ordering but also have some kind of high overall symmetry. However, for several elements of the first, second, and third period of the transition metal groups it has been shown that maximizing the number of next-nearest neighbours is not always the driving force behind the formation of a particularly stable structural motifs. The highly symmetric, undistorted icosahedron with a size of 13 atoms was found to be the global minimum merely in clusters of the early transition metals while the later elements prefer structures that are more open with lower average coordination numbers.[1,2] Zinc and cadmium are both special as they are found to form distorted and amorphous-like structures with low symmetry or no symmetry elements at all. Disordered in this context usually means that such structures have no overall order except a certain local ordering. In addition, several structures with small differences in their total energies compete for the global minimum making it difficult to identify a certain structural motif as the ground state structure. Interestingly, a different result was obtained for mercury where an icosahedron was found to be the most stable structure, a result that was ascribed to relativistic effects that also play an important role in the formation of small gold and platinum clusters. Disordered structures in small to medium-sized Zn and Cd clusters were reported in several other studies,[2–4] but also the experimental results supported these theoretical findings[5–7] despite the fact that already the bond length in the dimers was a source of some debate.[8–10] Studies on larger disordered Zn and Cd clusters are, however, rare and are typically based on a combination of a global optimization procedure and a semi-empirical method to sample the potential energy surface (pes). Among the used semi-empirical methods are the RGL potential of Cleri *et al.*[11] for instance coupled to an evolutionary-based algorithm or the Basin-hopping method. Thus, Michaelian *et al.* determined the putative global-minimum-energy structures for zinc and cadmium clusters with up to 192 atoms. They used the Gupta potential in combination with a genetic algorithm to sample the pes and after a re-optimization with density-functional-theory (DFT) calculations based on a local-density approximation (LDA) as well as a generalized-gradient approximation (GGA) they identified magic sizes (*i.e.*, particularly stable clusters) with 12,

[a] *Physical and Theoretical Chemistry, University of Saarland, 66123, Saarbrücken, Germany. E-mail: s.kohaut@mx.uni-saarland.de, m.springborg@mx.uni-saarland.de*
[b] *School of Materials Science and Engineering, Tianjin University, Tianjin 300072, China*

† Electronic supplementary information (ESI) available: The Cartesian coordinates of the relaxed lowest minimum energy structures and of the re-optimized Gupta clusters. A table that summarizes the properties of the re-optimized Gupta clusters. See DOI: 10.1039/c6cp04948f

This journal is © the Owner Societies 2016

Published on 13 September 2016. Downloaded by Universitat des Saarlandes on 17/12/2016 20:46:23.

38, 55, 75, and 147 atoms and showed that these clusters were not based on the usual symmetric structures that would result from a close packing of the atoms.[3] Zhao used a tight-binding approach in combination with a genetic algorithm in the size range of 2–21 atoms with a following DFT (GGA) re-optimization.[12] The structures reported in that study were different for several sizes compared to the ones obtained by using the RGL potential,[13] but the energy differences for some selected sizes between the first and the second lowest isomer were found to be vanishingly small. Such a complicated potential energy surface was also found in small to medium-sized silicon clusters where the identification of a unique ground state at elevated temperatures was not possible.[14] In addition, Zhao mentioned that the ionization potential of small Cd clusters reached the bulk limit very fast and that clusters larger than 20 atoms might already show a bulk-like behaviour,[12] a result that was also found earlier by Yonezawa *et al.* in their simulated-annealing-based study.[15] Besides the $n^{-1/3}$ dependency of the ionization potential on the cluster size, n, they concluded that even at sizes around $n = 7$ atoms the clusters were essentially metallic. Doye found putative global minima for zinc and cadmium clusters by using the Gupta potential in combination with the Basin-hopping method up to a size of 125 atoms. The vast majority of the obtained clusters did not show any overall ordering, but Doye observed that many of the structures were based on distorted oblate Marks decahedra. In addition, he concluded that using such potentials is questionable because of a strong dependency of the results on the actual potential parametrization.[13] Instead, Muñoz *et al.* used an extended Lennard-Jones potential to identify candidate structures that were subsequently treated using *ab initio* DFT (GGA) calculations. Thereby, they identified the putative global-minimum-energy structures for sizes between Cd_3 and Cd_{10}.[16] Johansson *et al.* reported tetrahedral Cd_n clusters for $n = 4$, 10, 20, 35, and 56 and showed that these structures were slightly lower in energy for Cd_4 and Cd_{10} than the corresponding structures obtained using the Gupta potential. Larger tetrahedral structures, however, were slightly higher in energy, although still accessible at elevated temperatures. They attributed the special ability of the tetrahedral motifs to arise from many-body effects that are not treated sufficiently accurately by empirical potentials.[17] Other authors undertook studies on small Cd and Zn clusters and concluded that the bonding within these clusters predominantly comes from van der Waals interactions with only minor contributions from covalent bonding.[18,19] An interesting effect that is caused by an unusually large core–shell separation in zinc clusters of certain sizes was reported by Aguado and co-workers.[20] Photoelectron measurements in combination with DFT (GGA) calculations were used to demonstrate that single clusters could possess both metallic and insulating regions in a Janus-like fashion. As seen from this discussion, the structures and their origins of smaller to medium-sized Cd clusters are far from being understood and, moreover, most results are based on the use of the more phenomenological Gupta potential. The purpose of the present work is, therefore, to perform a more accurate study of a large range of Cd_n clusters, $2 \leq n \leq 60$, which, as we shall demonstrate, will allow for a more thorough and complete understanding of their structural motifs. In addition, we shall assign structural motifs to the clusters that have shown to be of high stability in mass spectroscopic measurements (the so-called ''magic-sizes'') by Diederich and co-workers.[21]

We shall determine several new candidates for the putative global-minimum-energy structures using a combination of the density functional tight-binding (DFTB) approach coupled to an evolutionary-based algorithm. Finally, the resulting candidate structures will be re-optimized using a DFT approach. In order to identify the trends in their structures, various descriptors, including a bond-angle analysis, will be applied. These tools allow also the identification of possible growth patterns of the Cd clusters. Also their electronic properties will be analysed, including the adiabatic ionization potentials that can be compared with the experimental results. Finally, we shall analyse the bonding mechanism in these small to medium-sized cadmium clusters and try to identify the size for the onset of metallic behaviour.

2 Methods

2.1 The global optimization procedure

An evolutionary algorithm based on the ''cut-and-splice'' procedure introduced by Deaven and Ho[22] together with the density functional tight-binding theory as implemented in the Hotbit code[23] was used to sample the potential energy of each Cd_n cluster. The algorithm was linked to the atomic simulation environment (ASE) code of Bahn and Jacobsen.[24] In a typical calculation, a population of 10 members was used with the first generation consisting of clusters whose atoms were placed randomly within a cubic box so that a minimum distance of 2.0 Å between two atoms was ensured. Afterwards the two fittest current population members were allowed to form one child with all of the other current population members through a crossover process. In addition mutants were created from all population members by applying operators that have earlier been proposed in the literature including random movements of atoms (probability $p = 0.5$), exchange of two halves of a cluster through a random plane ($p = 0.3$) and twinning mutations ($p = 0.2$).[25–27] Mutants were accepted as candidates in the current generation if their energy was lower, or in the other case at least 0.1 eV higher than the energy of the fittest cluster in the current generation whereby it is ensured that the created mutants efficiently introduce new structural motifs in the gene pool. For the members of the pool of all parents, children and mutants, a tournament of size 5 with the purpose of identifying which clusters should form the next generation of 10 members was carried through. To avoid a loss of a beneficial genome, we passed the cluster with the so far lowest total energy without any modification to the next generation. We assumed that the algorithm was converged if the cluster with the lowest energy did not change for 100 consecutive steps. In the case of a premature convergence we monitored the standard deviation of the fitness function and applied random mutations to keep the value above a

Published on 13 September 2016. Downloaded by Universitat des Saarlandes on 17/12/2016 20:46:23.

threshold of at least 0.1 eV. Three unbiased runs were conducted and the clusters with the overall lowest total energy for every size were finally treated using parameter-free DFT calculations.

2.2 Parametrization of the DFTB method

Within the DFTB method, the total energy of a given system relative to that of the non-interacting neutral atoms can be approximated as a sum of the eigenvalues of all occupied orbitals minus that of the neutral, non-interacting atoms, E_{BS}, plus a term that arises from Coulomb interactions, E_{Coul}, and a pairwise repulsive potential, U_{rep},[28,29]

$$E = E_{BS} + E_{Coul} + U_{rep}. \quad (1)$$

At the lowest level of approximation (corresponding to the so called non-SCC DFTB) we neglect interactions that result from charge fluctuations, *i.e.*, E_{Coul}. U_{rep} is parametrized and can be determined by fitting to either the experimental or the *ab initio* results for some reference system(s).

Using an LCAO approach with the orbitals expanded in terms of a minimal set of atomic-centered non-orthogonal basis functions,

$$\psi_i(\vec{r}) = \sum_v c_{vi}\phi_v(\vec{r}), \quad (2)$$

one has to solve the Kohn–Sham eigenvalue equations for an effective potential V_{eff} to determine E_{BS} as the sum over the eigenvalues of all occupied orbitals,

$$\hat{H}\psi_i(r) = \varepsilon_i\psi_i(r), \quad (3)$$

with

$$\hat{H} = \hat{T} + V_{eff}. \quad (4)$$

here, $\hat{T}$ is the kinetic-energy operator.

Substitution of (2) into (3) gives the eigenvalue equation

$$\sum_v c_{vi}(H_{vi} - \varepsilon_i S_{vi}) = 0 \quad (5)$$

with

$$H_{vi} = \langle\phi_v|\hat{H}|\phi_i\rangle \quad (6)$$

and

$$S_{vi} = \langle\phi_v|\phi_i\rangle. \quad (7)$$

The elements H_{vi} and S_{vi} are determined from calculations on diatomic molecules. Thereby it is assumed that the effective potential can be written as a superposition of atomic potentials

$$V_{eff}(\vec{r}) = \sum_n V_n\left(\left|\vec{r} - \vec{R}_n\right|\right) \quad (8)$$

with $\vec{R}_n$ being the position of the nth atom. Moreover, $V_n(r)$ is the potential of the free, isolated, nth atom, $V_n^{(0)}(r)$, augmented by a short-ranged confining potential that reproduces the contraction of the orbitals when passing from the isolated atom to a compound,

$$V_n(r) = V_n^{(0)}(r) + \left(\frac{r}{r_0}\right)^2. \quad (9)$$

For r_0 we used a value of 5.4 Bohr to get the best agreement between the DFTB calculated electronic band structures and the ones derived from *ab initio* DFT calculations using the PBE functional.

Subsequently, we assume that

$$\langle\phi_v|\hat{T} + V_{eff}|\phi_i\rangle = \begin{cases} \langle\phi_v|\hat{T} + V_n|\phi_i\rangle & \text{for } \phi_v, \phi_i \text{ both on atom } n \\ \langle\phi_v|\hat{T} + V_n + V_m|\phi_i\rangle & \text{for } \phi_v, \phi_i \text{ on atoms } n \neq m \\ 0 & \text{otherwise} \end{cases}. \quad (10)$$

U_{rep} is determined by fitting to the accurate results from *ab initio* DFT (PBE) calculations. In the present work we minimized the force differences $|F^{DFT} - F^{DFTB}|$ in small Cd clusters taken from Muñoz *et al.*[16] with a smoothing spline as explained by Koskinen and Mäkinen.[23] For the repulsion interaction we used a very short cut-off of 3.4 Å, which had the consequence that our calculations were not able to reproduce the large experimental bond length of the dimer (4.07 Å,[9] 3.78 Å[10]). However, as we will discuss later, also *ab initio* DFT methods are not able to reproduce the experimental bond length in the cadmium dimer and we do not expect a parameterized, approximated approach to DFT to perform better in this context. In fact, as emphasized, *e.g.*, by Flad *et al.*[18] clusters of the group-12 elements are special since their bonding properties change from weak van der Waals interactions, *via* covalent bonding, to metallic bonding when their size is increased. Thus, of all Cd_n clusters, the bonding of the one with $n = 2$ may be the most difficult one to treat theoretically.

We checked whether it is possible to keep the 4d states within the core during the DFTB search which would allow us to reduce the size of the basis set and, consequently, the computational requirements. We found that the relative ordering of the isomers of the smaller clusters changed only little, although for an accurate description of the electronic properties, other DFTB parametrizations that explicitly include the 4d orbitals may be more useful.[30] Moreover, it may be relevant to mention that for an accurate description of the bulk phase using parameter-free approaches, an explicit treatment of the 4d states is mandatory[31] But for the purpose of obtaining accurate relative energies and structures, keeping the 4d states in the core should not lead to significant inaccuracies.

2.3 DFT calculations

All subsequent *ab initio* DFT calculations were performed using the PBE functional for exchange and correlation in combination with the Def2-TZVP[32,33] basis set and as implemented in the Gaussian09 program.[34] Due to the complicated nature of the PES, a tighter criterion for the geometry relaxation (10^{-5} Hartree $Bohr^{-1}$) was used. For the re-optimization of the candidates for the global minimum with DFT, the 4d states were treated explicitly in all calculations. In addition, we considered structures that were found using Gupta potentials in the description of the interatomic interactions. In this case, the structures were obtained

 This journal is © the Owner Societies 2016

Published on 13 September 2016. Downloaded by Universitat des Saarlandes on 17/12/2016 20:46:23.

from the Cambridge Cluster Database[35] and re-optimized with DFT (PBE) as described above.

At this place it may be relevant to mention that it, in principle, is possible to include dispersion corrections within DFT calculations in an *ad hoc* approach like that of Grimme.[36] However, the physical motivations behind doing so in the present case are highly questionable. The dispersion interactions depend on the polarizabilities of the interacting species that, for metallic systems, diverge, suggesting diverging dispersion interactions, although the *ad hoc* corrections are finite. Thus, for the present systems we will consider the inclusion of such corrections rather as an empirical correction that may or may not improve certain results although, as above, it is unclear what will happen in those cases where no comparison with the reference results is possible. In the same spirit, one may also consider using other approximate density functionals but, again, lacking any reference information it is hardly possible to identify any optimal density functional.

3 Results

We first analyse the actual obtained clusters regardless of whether they have been found from DFTB or Gupta based global optimization runs and afterwards dedicate a part of this study to critically discuss differences in the results between DFTB and Gupta based approaches.

3.1 Structures of the individual Cd_n clusters

Our obtained lowest-energy isomers for clusters with up to 16 atoms together with other proposed global-minimum-energy structures are shown in Fig. 1. As already mentioned, smaller Cd clusters and especially the dimer is a problem for DFT calculations due to its complicated bonding mechanism that has been described as a mixture of van der Waals and covalent contributions.[18,37] Compared to the shortest reported experimental bond length of 3.78 ± 0.03 Å our value of 3.509 Å is, however, in agreement with the other reported results of DFT calculations.[16] Also our calculated binding energy, E_b, of 0.032 eV per atom is smaller than spectroscopic values (0.041 per atom eV[9,10]). The results reported from calculations with more sophisticated post-HF methods like coupled-cluster (CCSD(T)) are with values of 3.873 Å for the bond length and 0.040 eV per atom for the binding energy in excellent agreement with the experimental results.[19]

For Cd_3 we found an equilateral triangle of point group (PG) D_{3h} with a bond length of r = 3.347 Å, a value that is smaller than the one found by Zhao (r = 3.45 Å)[12] but still larger than the value of Muñoz *et al.* (3.202 Å).[16] The four and five atoms of Cd_4 and Cd_5 form a tetrahedron (T_d) of bond length r = 3.205 Å and a trigonal bipyramid of PG D_{3h} with a bond length of r_{apical} = 3.409 Å and a shorter bond distance of r_{basal} = 3.157 Å, respectively. Planar structures as found for the small silver clusters Ag_4 and Ag_5[38] had higher energies for Cd_4 (+0.25 eV, rhombus, PG C_{2v}) and Cd_5 (+0.27 eV, trapezoid, PG C_{2v}) and were actually found to be saddle points on the PES with very small imaginary vibrational modes (Cd_4: 10.41i cm^{-1}, Cd_5: 10.58i cm^{-1}, 7.29i cm^{-1}). A pentagonal bi-pyramid with a missing vertex was the lowest in energy for Cd_6, followed by a pentagonal pyramid (+0.13 eV) and an octahedron (+0.22 eV) with point group O_h. We did not observe a Jahn–Teller distortion as otherwise reported by Zhao[12] for the highly symmetric octahedron of Cd_6 with PG O_h, nor in the pentagonal bi-pyramid which was found to be slightly higher in energy (+0.06 eV) than the global minimum at that size.

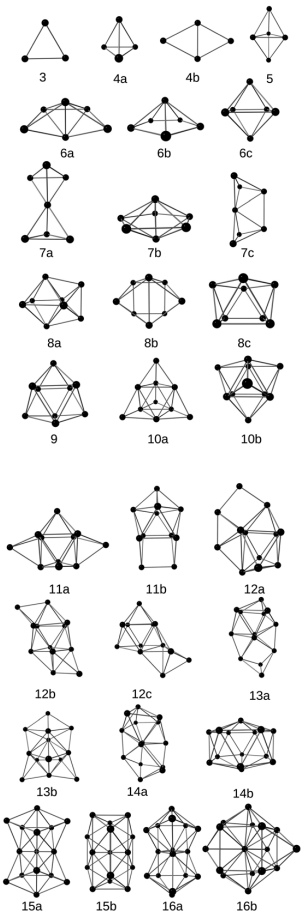

Fig. 1 The putative global-minimum-energy structures of Cd_{3-15} and some other energetically low-lying isomers.

A summary of the calculated properties of our clusters up to a size of 16 atoms can be found in Table 1 where we also compare with the CCSD(T) results of Flad *et al.*[18] This comparison demonstrates that our calculations are capable of reproducing the structural motifs of the smallest clusters but that our calculations predict too large bonding energies and too short bond lengths, as was already found for the Cd_2 dimer to an even higher extent. Thus, it may be suggested that as the size of the Cd_n clusters increases and the chemical bonding becomes more covalent, our calculations become increasingly accurate.

Published on 13 September 2016. Downloaded by Universitat des Saarlandes on 17/12/2016 20:46:23.

Table 1 Point group symmetries (PGs), cohesive energies E_{coh} (eV per atom), average bond lengths d_{av} (Å), effective coordination numbers (ECNs), HOMO–LUMO gaps ΔHL (eV) and adiabatic ionization potentials (aIPs) (eV) of the lowest energy Cd_{3-16} clusters

N	PG	E_{coh}	d_{av}	ECN	ΔHL	aIP
3a	D_{3h}	0.079	3.35	2.00	3.16	7.37
4a	T_d	0.151	3.20	3.00	3.09	6.74
5	D_{3h}	0.156	3.32	3.48	2.58	6.42
6a	C_{2v}	0.163	3.32	3.71	2.56	6.49
6b	C_{5v}	0.141	3.30	3.30	2.07	
6c	O_h	0.126	3.49	4.00	2.17	
7a	D_3	0.182	3.20	3.42	2.39	6.33
7b	D_{5h}	0.175	3.38	4.48	2.57	
7c	C_{2v}	0.181	3.22	3.63	2.57	
8a	D_{2d}	0.184	3.28	4.28	1.97	6.07
8b	C_{2v}	0.184	3.26	4.12	1.90	
8c	D_{4d}	0.183	3.25	3.99	1.87	
9	D_{3h}	0.226	3.20	4.59	1.62	6.18
10a	T_d	0.246	3.16	4.53	2.38	6.24
10b	C_{3v}	0.245	3.17	4.79	1.77	
11a	D_{3h}	0.248	3.20	4.90	1.92	5.91
11b	C_{2v}	0.214	3.23	4.43	1.19	
12a	C_s	0.246	3.17	4.42	1.63	5.70
12b	C_2	0.233	3.24	4.86	1.49	
12c	C_1	0.231	3.24	4.88	1.32	
13a	C_s	0.251	3.18	4.81	1.63	5.80
13b	C_s	0.245	3.24	4.95	1.74	
14a	C_1	0.263	3.17	4.96	1.52	5.94
14b	D_{6d}	0.210	3.30	5.08	1.16	
15a	C_{2v}	0.281	3.16	5.26	1.51	5.51
15a	C_{2v}	0.281	3.16	5.26	1.51	5.51
15b	D_{3h}	0.278	3.18	5.33	1.41	
16a	C_s	0.279	3.19	5.32	1.41	5.62
16b	C_s	0.267	3.20	5.33	1.34	
3[a]	D_{3h}	0.038	3.93			
4[a]	T_d	0.085	3.46			
5[a]	D_{3h}	0.097	3.59			
6[a]	C_{2v}	0.104	3.65			

[a] Results from CCSD(T) were taken from Flad and co-workers.[18]

The global minimum in Cd_7, consisting of two corner-sharing tetrahedra, is almost degenerate in energy (+0.01 eV) with an isomer 7b that was proposed as the global minimum by Muñoz *et al.*[16] in which the two tetrahedra are connected *via* an interatomic bond.

Also for Cd_8, the three energetically lowest isomers were found within an energy range of only 0.01 eV with a bi-capped octahedron being the lowest in energy, followed by a bi-face-capped trigonal prism (<+0.01 eV) and a square-antiprism (+0.01 eV). The tricapped trigonal prism (TTP) was the lowest structure for Cd_9 in agreement with other studies.[12,16] We re-optimized several other isomers that were found to be stable within the DFTB method, including a part of an icosahedron (PG C_{2v}), a face-capped square-antiprism (PG C_{2v}), a tri-capped octahedron (PG C_s), and two face-sharing octahedra (PG D_{3h}). None of these proved to be stable during the relaxation process with all of them leading to the TTP motif.

The TTP motif is found also for clusters with 10 atoms with an additional atom in a face-capping position above one of the equilateral triangles. However it is not the global minimum, the tetrahedral structure proposed by Johansson and Pyykkö[17] was slightly lower in energy (−0.02 eV). At a size of eleven atoms the lowest-energy isomer was a tri-capped trigonal prism with all of its faces occupied by Cd atoms. Also the other structures for Cd_{11} were based on the TTP motif, one structure with PG C_s (+0.16 eV) and the other with PG C_{2v} (+0.37 eV).

Up to a size of 11 atoms, all of the possible candidates for the global minima possess the same structural motifs as found in zinc clusters of equal size with some few exceptions (*e.g.* for Zn_8).[4] Moreover, Zhao *et al.* predicted that the further growth of a small Cd cluster should be based upon icosahedral units,[12] but our structures in the size range of 12–15 atoms are more similar to the corresponding zinc structures of equal size and are based upon the TTP motif of Cd_9, quite similar to the structures of germanium clusters of the same size.[39]

The tetra-capped trigonal prism as seen in Fig. 1(11b) has a higher total energy and the energetically lowest structure for Cd_{12} is indeed based upon the TTP unit. On the other hand, structures based on the tetra-capped trigonal prism (12b and 12c) are 0.15 eV and 0.18 eV higher in energy, respectively. Our results suggest that it is unlikely that structures with icosahedral units are those of the global-total-energy minimum for small Cd clusters. Thus, for Cd_{13} the icosahedron was found to be 0.44 eV higher in energy than the most stable structure, and for Cd_{14} the face-capped isomer was found to be 0.43 eV above the global-minimum-energy structure. A disordered structure for the global minimum for Cd_{13} was also reported by others using molecular-dynamics-based methods[1] or simulated-annealing/Taboo-search methods in combination with DFT calculations.[2]

As one of the largest clusters for which the most stable structure contains the TTP motif, our results gave a cluster with a similar configuration to that found for Ge_{15}[39] as the most stable one for Cd_{15} followed by an isomer slightly higher in energy consisting of two fused tricapped trigonal prisms (+0.05 eV). For Cd_{16} the energetically lowest structure is based on two fused units of the structure 10b in Fig. 1 that share one of the triangular faces and the atom that forms the tip of the square pyramid. This structure was also reported to be the global minimum for Ge_{16} by several other authors.[39–41] Structures that were based on distorted decahedral features like 16b in Fig. 1 were found to be 0.18 eV higher in energy.

From the Cd_{17} cluster the growth pattern changes (Table 2), since for this size a different structural motif besides the stacking of TTP units appears. This is similar to the case for zinc clusters, for which a transition from prolate, low-coordinated and cage-like structures to spherical clusters with atoms occupying positions in the center was found for clusters with 17 atoms.[4] Doye[13] reported that Zn_{16}–Zn_{21} and Cd_{16}–Cd_{21} are based on distorted Marks decahedra where two atoms that were originally isolated in a face-capping position on one of the square faces form a bond which simultaneously removes the bonds between the atoms that were forming the square faces. The two bonded atoms are displaced slightly inwards, thereby coming closer to the central atoms which leads to increased coordination numbers of these inner atoms.

A view along the fivefold symmetry axis in Cd_{17} with the atoms marked that were in a face-capping position is shown in Fig. 2 together with the other putative global-minimum-energy structures and the structures that were obtained from the DFT

 This journal is © the Owner Societies 2016

Published on 13 September 2016. Downloaded by Universitat des Saarlandes on 17/12/2016 20:46:23.

Table 2 Point group symmetries (PGs), cohesive energies E_{coh} (eV per atom), average bond lengths d_{av} (Å), effective coordination numbers (ECNs), HOMO–LUMO gaps ΔHL (eV) and adiabatic ionization potentials (aIPs) (eV) of the lowest energy Cd_{17-60} clusters

N	PG	E_{coh}	d_{av}	ECN	ΔHL	aIP
17	D_{4d}	0.284	3.20	5.78	1.029	5.54
18a	C_1	0.290	3.18	5.86	0.879	5.40
18b	C_{2v}	0.277	3.22	5.49	1.011	
19a	C_{3v}	0.303	3.15	5.66	0.924	5.54
19b	C_{2v}	0.284	3.20	5.69	1.029	
20a	C_{3v}	0.319	3.14	6.03	1.306	5.49
20b	C_{2v}	0.288	3.17	5.80	0.696	
21a	C_s	0.314	3.16	6.00	1.276	5.38
21b	C_1	0.311	3.17	5.97	1.135	
22	C_s	0.311	3.16	5.70	1.193	5.50
23	C_s	0.322	3.15	5.80	1.241	5.52
24	C_1	0.329	3.15	5.99	1.008	5.43
25	C_{3v}	0.339	3.15	6.11	1.282	5.56
26	C_{2v}	0.338	3.14	5.94	1.124	5.53
27	C_s	0.347	3.14	6.13	1.125	5.46
28	C_{2v}	0.353	3.15	6.41	0.925	5.38
29	C_s	0.349	3.16	6.38	0.945	5.42
30	C_s	0.357	3.15	6.47	0.880	5.40
31	C_{3v}	0.364	3.15	6.73	0.787	5.41
32	C_1	0.362	3.15	6.64	0.790	5.15
33	C_s	0.361	3.18	6.82	0.739	5.30
34	T_d	0.372	3.16	6.98	0.647	5.46
35	C_s	0.374	3.12	6.67	0.695	5.16
36	C_{2v}	0.358	3.11	6.34	0.699	5.14
37	C_1	0.368	3.12	6.29	0.796	5.03
38	C_s	0.369	3.14	6.66	0.563	4.95
39	C_s	0.374	3.14	6.85	0.746	5.24
40	C_s	0.376	3.11	6.29	0.739	5.05
41	C_1	0.383	3.12	6.78	0.707	5.05
42	C_s	0.386	3.12	6.71	0.643	5.07
43	C_s	0.391	3.12	6.80	0.717	5.17
44	C_{2v}	0.389	3.11	6.73	0.611	5.22
45	C_s	0.399	3.10	6.82	0.581	5.23
46	T_d	0.411	3.09	6.94	1.130	5.33
47	C_s	0.407	3.10	6.91	1.006	5.11
48	C_s	0.406	3.11	6.92	0.830	5.03
49	C_s	0.408	3.11	7.01	0.853	5.19
50	C_s	0.405	3.10	6.90	0.652	5.00
51	C_s	0.405	3.13	6.99	0.652	5.04
52	C_{2v}	0.407	3.13	7.09	0.654	5.05
53	C_1	0.408	3.10	6.99	0.539	4.95
54	C_1	0.406	3.12	7.08	0.485	4.87
55	C_s	0.411	3.12	7.11	0.546	5.11
56	C_s	0.415	3.13	7.22	0.524	5.05
57	C_1	0.415	3.12	7.25	0.390	4.90
58	C_1	0.415	3.13	7.16	0.462	4.92
59	C_1	0.418	3.12	7.21	0.343	4.84
60	C_1	0.422	3.11	7.23	0.285	4.87

re-optimization of the Gupta minima for the Cd_n clusters with n = 17–21.

It is, however, less trivial to identify main structural motifs for the clusters obtained *via* the DFTB calculations as is the case for the Gupta-derived clusters. In the latter case, for example the five-fold symmetry of the underlying decahedra can easily be identified in 20b in Fig. 2. Also for some clusters, structural motifs related to the putative global-minimum-energy structures of smaller clusters can be identified. This is, *e.g.*, the case for 21b in Fig. 2 where the structure of Cd_{15} can be recognized (marked in white).

Next we shall discuss how the structural properties of the clusters develop when the clusters get larger. To this end, we shall use various descriptors.

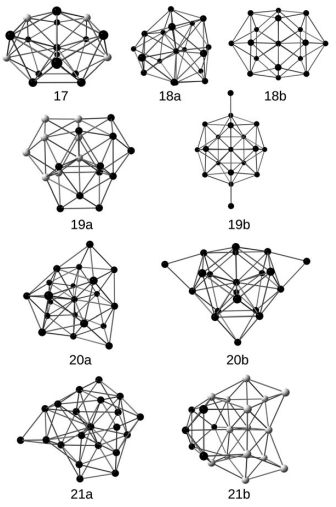

Fig. 2 The putative global-minimum-energy structures of Cd_{17}–Cd_{21} and some of the low-energy isomers obtained from the re-optimization of the structures of Doye[13] found with the Gupta potential. Atoms that belong to a special structural motif are marked in white and are discussed in detail in the text.

Several methods have been introduced with the aim of identifying local environments of atoms that would correspond to atomic arrangements that are typically found in the bulk.[42] As one of those, we used the bond-angle-analysis method of Ackland and Jones[43] as implemented in the ovito program[44] to assign the fcc, hcp, bcc, icosahedral or disordered structure type to each atom of a cluster. The method is based on first calculating a histogram of the values of $\cos\theta_{ijk}$ for each atom, j, and all its neighbouring atoms i and k. Neighbouring atoms are considered to be within a pre-determined cut-off distance which is the average distance over all atoms of their six nearest neighbours. Using heuristic rules, each of these histograms can give an estimate of the local environment of each atom.

Further insight into structural motifs of Cd_n beyond the bond angle analysis can be obtained from the average effective coordination numbers (ECNs) and bond lengths d_{av} using an approach of Hoppe,[45]

$$d^i_{av} = \frac{\sum_{j=1}^{n} d_{ij} e^{\left[1-\left(d_{ij}/d^i_{av}\right)^6\right]}}{\sum_{j=1}^{n} e^{\left[1-\left(d_{ij}/d^i_{av}\right)^6\right]}}. \quad (11)$$

here, d_{ij} is the distance between atoms i and j. It is seen that d^i_{av} has to be determined iteratively. Thereby, d^i_{av} is initially taken as the shortest bond length for atom i and the final value is obtained self consistently using a convergence criterion of 10^{-4} Å. Finally, the effective coordination number ECN of atom i is given by

$$\mathrm{ECN}(i) = \sum_{j=1}^{n} e^{\left[1-\left(d_{ij}/d^i_{av}\right)^6\right]}. \quad (12)$$

Published on 13 September 2016. Downloaded by Universitat des Saarlandes on 17/12/2016 20:46:23.

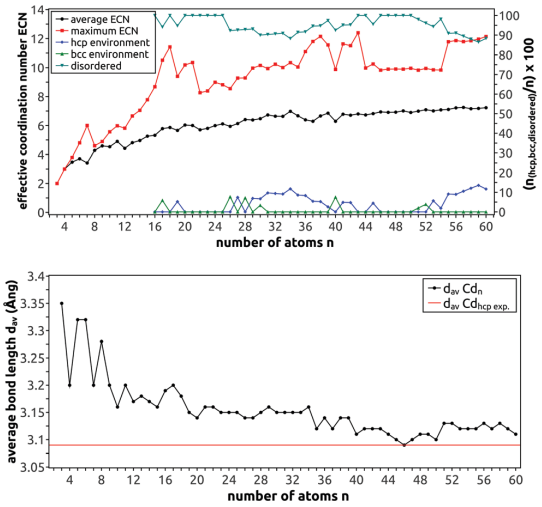

Fig. 3 The average and maximum effective coordination number ECN together with the results from the bond angle analysis (top panel) and the evolution of the average bond length d_{av} (bottom panel) in small to medium-sized cadmium clusters as a function of size n.

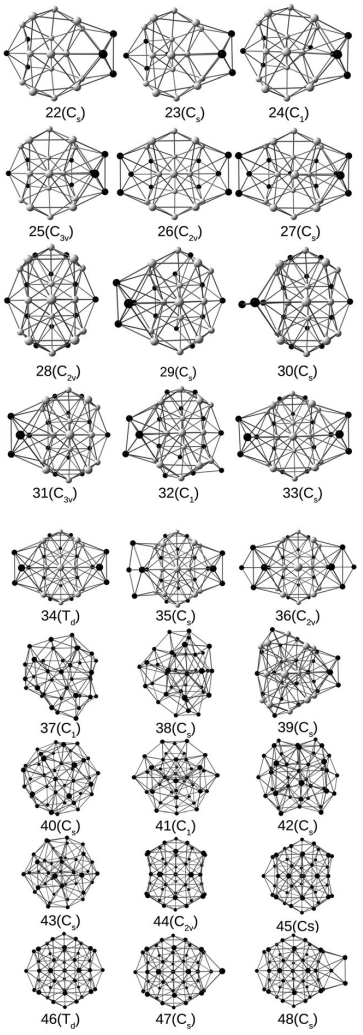

Fig. 4 The putative global-minimum-energy structures for Cd_n clusters with $22 \leq n \leq 48$ and their corresponding point group symmetry. The atoms marked in white are parts of the Cd_{15} unit.

For each cluster size we calculate ultimately averages of ECN(i) and d^i_{av}. In Fig. 3 we show these averages for all Cd_n clusters.

The results of the bond angle analysis show that the central atom in clusters as small as 16 atoms has a local coordination similar to what can be found in the bulk bcc or hcp structures. As has been observed in small silicon clusters, for which a transition from prolate to spherical shapes is seen for clusters with more than 21 atoms, we found such a transition in Cd_n at the smaller size of 18 atoms and, accordingly, just one atom larger than for zinc. However, according to the bond angle analysis, all atoms in Cd_{18} are in a disordered surrounding although the central atom has a coordination number of 12, similar to the value for the bulk hcp phase of cadmium. At a size of 22 atoms, the ECN drops to a value around 8.0 and the shape of the clusters becomes again more prolate as shown in Fig. 4. None of the clusters with n = 21–25 have atoms with a bulk-like coordination in the center and they can at best be described as containing tricapped-trigonal prisms with Cd_{15} as the building block. We will show below that the Cd_{15} unit indeed is particularly stable.

Further growth around the Cd_{15} motif continues up to a size of at least 36 cadmium atoms. Moreover, for Cd_{26}, Cd_{28}, and Cd_{30} we observed atoms in the core with a bcc-like arrangement and for Cd_{27}, Cd_{29}, and Cd_{31}–Cd_{39} with a hcp-like environment. A maximum of hcp-like atoms in the center of the cluster is then reached for the highly symmetric tetrahedral (PG T_d) cluster Cd_{34}. Although not being in the core of the cluster, the Cd_{15} motif itself can still be recognized in the outer part in some of the clusters with neighboring sizes (*e.g.* in Cd_{39}).

However, it was not possible to assign a final structural motif for the clusters with sizes between 37 and 43 atoms. Instead, it is useful to study the structural similarity between clusters of neighbouring sizes. To this end, we calculate a so-called similarity index S between to structures from

$$S = \frac{1}{1 + \frac{\sqrt{q}}{u_1}}. \quad (13)$$

here, the quantity q that has to be minimized is defined as

$$q = \frac{1}{2n}\left(\sum_{i=1}^{n} d^2(a_i, b(a_i)) + \sum_{i=1}^{n} d^2(b_i, a(b_i))\right), \quad (14)$$

where n is the number of atoms in the smaller cluster. q quantifies the sum of the squares of the distances between the atoms of one of the clusters and the closest partner of the

 This journal is © the Owner Societies 2016

Published on 13 September 2016. Downloaded by Universitat des Saarlandes on 17/12/2016 20:46:23.

other cluster when the two clusters are superposed with the additional possibility that the structure of one of the two clusters is scaled by a constant factor. a_i is then one of the atoms of one of the clusters and $b(a_i)$ is its closest partner in the other cluster. Similarly, b_i is one of the atoms in the second cluster and $a(b_i)$ its partner in the first cluster. Unfortunately, the identification of that superposition and that constant scaling factor that optimizes q is non-trivial and, therefore, we use a genetic algorithm for this purpose. Then, the optimization of q involves a genome consisting of several operators including three translations, three rotations, a scaling, and an inversion. Typically, a population of 40 members was found to be appropriate to identify the optimal q within 3000 generations.

In eqn (13), u_l is a length unit, which is arbitrarily chosen to be the average nearest-neighbour distance in the clusters. Our experience with this similarity index, S, gives that a value below 0.8 implies that the two objects are not similar (*e.g.* a square and a tetrahedron for which S equals 0.7). S values between 0.8 and 0.9 are typically found for cases where one structure is closely related to a distorted version of the other structure (*e.g.* a perfect icosahedron with 13 atoms compared to a decahedron of similar size giving S = 0.8). Objects that are only scaled versions of each other (*e.g.* two octahedra with different bond lengths) but otherwise closely resemble each other are correctly identified to be very similar and therefore a value of S = 1.0 is found.

In Fig. 5 we show S for the comparison of the Cd_n cluster with the Cd_{n+1} cluster as a function of n. The fact that S takes relatively high values between 22 and 35 confirms the structural similarity for those sizes, already indicated above. All clusters between a size of 37 and 43 atoms are disordered, dissimilar and of low overall symmetry with the exception of Cd_{38} which shows some similarities not only in its average ECN and bond length but also in its atomic arrangement to Cd_{39}.

On the other hand, the bond-angle analysis of Fig. 3 suggests that there is a maximum in the number of atoms with an hcp-like surrounding for Cd_{34} that subsequently decreases up to n around 40 while simultaneously the maximum ECN increases to 12. It is interesting to notice that although there are more atoms in the center of Cd_{38} with a coordination number greater than 9 compared to Cd_{34} (we consider atoms to be in the core if their ECN is above 9 since no atom in the surface region has a larger value for the ECN), the core is still more hcp-like in Cd_{34} than in Cd_{39} according to the bond angle analysis.

The Cd_{44} cluster of PG symmetry C_{2v} forms the core of the following larger structures up to a size of 54 atoms, with the exception of Cd_{53} whose structure is that of a distorted Marks decahedron which is by 0.18 eV more stable. Continuing the growth around the Cd_{44} core would ultimately result in a tetrahedral cluster of PG T_d at a size of 58 atoms which was, however, not found to be the structure of the global minimum for Cd_{58}. Instead, we obtained disordered clusters with low symmetry for sizes between 55 and 60 atoms which are nevertheless very similar (*cf.* Fig. 6). While the average ECN grows very slowly from 6.8 to 7.2 we see a jump of the maximum ECN from Cd_{54} to Cd_{55} and an increase in the number of atoms with a hcp configuration indicating that the atoms in the core of the cluster are subjected to a re-organization at that size. In parallel, the average bond length seems to be converged at sizes around 40 atoms and are close to the value of the average experimental bond length in bulk hcp cadmium.

The combined results from the bond angle analysis and from the similarity index allow unfortunately not for a classification of the obtained structures into any of the common structures for metallic clusters. However, a general trend is the existence of a tetrahedron at the center of the clusters for sizes as small as n = 21. Such tetrahedral clusters were first described by Leary and Doye as those of local minima for the Lennard-Jones (LJ) cluster with 98 atoms.[46] In order to illustrate the similarity of our structures with this larger one, we show in Fig. 7 the

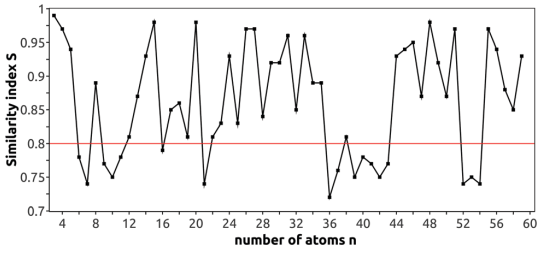

Fig. 5 The calculated similarity index S for the comparison of Cd_n with Cd_{n+1}. The red line represents the border at which two neighboring clusters are considered to be dissimilar, *i.e.*, S drops below a value of 0.8.

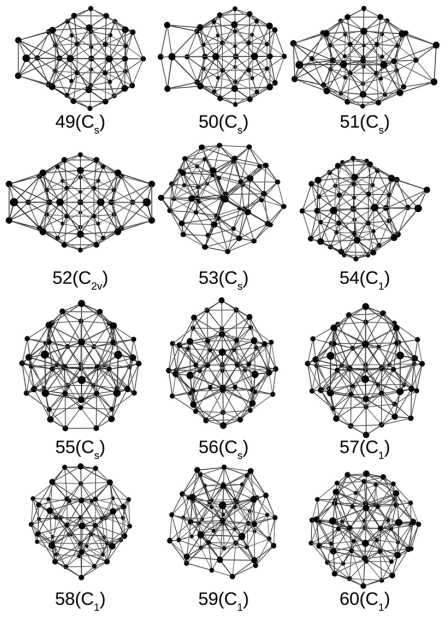

Fig. 6 The putative global-minimum-energy structures for Cd_n with sizes between 49 and 60 atoms and their corresponding point group symmetries.

Published on 13 September 2016. Downloaded by Universitat des Saarlandes on 17/12/2016 20:46:23.

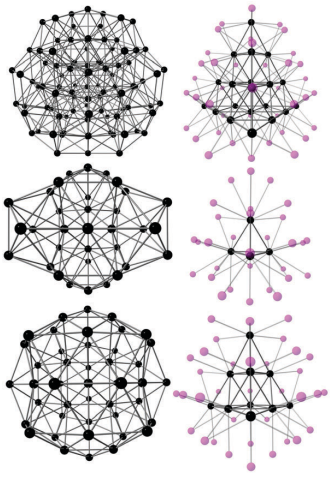

Fig. 7 Lennard-Jones cluster with 98 atoms (T_d) and the tetrahedron at the core of the cluster (top). The middle row shows Cd_{34} (T_d) and the bottom row Cd_{44} (T_d) both with their corresponding core to the right. Atoms marked in pink represent the next coordination shell around the tetrahedron.

LJ_{98} cluster with its tetrahedral core together with Cd_n clusters of increasing size that were found to have a tetrahedron at their center.

The coordination sphere around the inner tetrahedron shows an interesting topology with no atoms in a face-capping position above the faces of one of the smaller tetrahedra. A larger fraction of the outer atoms prefer edge-capping positions between two neighboring atoms of the tetrahedra, and together with the remaining atoms that are only connected *via* a single bond to one of the core atoms they form tricapped-trigonal prisms around the center of the structure. Based on this and the calculated similarity index S that showed a structural similarity for clusters with sizes between 22 and 36 and from 44 to 52 atoms we conclude that cadmium clusters in that size regime tend to form a Leary tetrahedral structure.

The clusters Cd_{37} to Cd_{43} with the exception of Cd_{40} and Cd_{43} possess a distorted tetrahedron in the core (see Fig. 8) although their overall atomic arrangements are not very similar according to the calculated similarity index S shown in Fig. 5. The two exceptions of Cd_{40} and Cd_{43} prefer a trigonal prism or a pentagonal bi-pyramid in their centres. Larger clusters with more than 54 atoms (see Fig. 6) that were all similar to each other (*cf.* Fig. 5) show a tendency towards maximizing the number of atoms with a hcp-like environment in their core. However, for sizes beyond those of the present study, it becomes difficult to suggest the growth pattern which, for instance, can be seen from the fact that Cd_{58} does not possess a T_d structure. Thus, it is possible that the Leary tetrahedral motif is abandoned in favor of another motif for larger clusters.

We close this subsection by comparing the structures obtained from the DFTB and the Gupta based samplings of the potential energy surface. Despite the fact that the Gupta potential

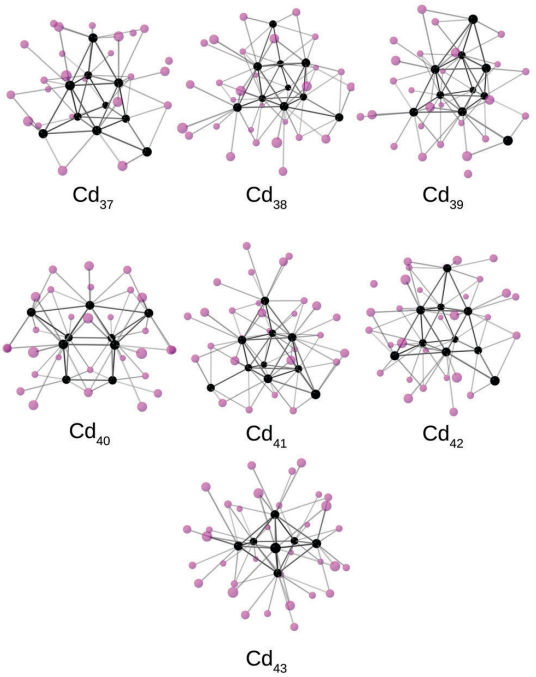

Fig. 8 The cores of Cd_{37} to Cd_{43}. Atoms marked in pink represent the next coordination shell around the core.

has been fitted to reproduce several bulk properties in hcp-Cd it performs surprisingly well in providing candidates for putative global-minimum-energy structures for clusters smaller than 13 atoms. At a size of 14 atoms the differences in the structures become occasionally significant and the energy difference at the DFT (PBE) level exceeds even 1 eV (see further below). To get an impression why the Gupta potential leads to structures with a larger energy at the DFT level than those based on the DFTB calculations, we calculated the average and maximum ECN of all clusters before the *ab initio* re-optimization and show the results in Fig. 9.

The Gupta potential yields structures that in general are more compact with a greater average coordination number per atom than the ones obtained by using the DFTB method. Although both methods suffer from over-coordination compared to the results after re-optimization, the Gupta potential more frequently produced clusters with significantly larger maximum coordination numbers than what was found when using the DFTB method. As a consequence, the DFT optimization procedure then reduced the number of atoms within the coordination sphere of the central atoms which ultimately leads to compact structures with low-coordinated atoms on the surface of the clusters as can be seen for example in Fig. 2 for Cd_{19b} and Cd_{20b}. However, we add that structures with a distorted decahedral motif as predicted by the Gupta potential may become important for sizes greater than or equal to 44 atoms as the difference in the *ab initio* energies between the decahedral structures of the

 This journal is © the Owner Societies 2016

Published on 13 September 2016. Downloaded by Universitat des Saarlandes on 17/12/2016 20:46:23.

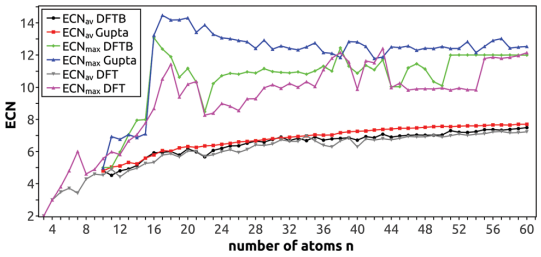

Fig. 9 A comparison of the average and maximum ECN of potential candidates before an *ab initio* re-optimization with DFT (PBE) obtained from DFTB or Gupta sampling of the Cd_n potential energy surface. In addition, we include the average and maximum ECN after the DFT (PBE) re-optimization.

Gupta potential and the non-decahedral clusters of the DFTB calculations is either smaller than 0.1 eV (*e.g.* Cd_{44}, Cd_{54}, and Cd_{58}) or in the singular case of Cd_{53}, the structure of the Gupta potential becomes even lower in energy than the DFTB derived cluster.

3.2 Trends in the energetic properties

At first, we found in all cases, except for Cd_{53} and Cd_{21}, structures with a lower energy when using the results from the DFTB searches compared to those found using the results with the Gupta potential, as can be seen in Fig. 10. Moreover, the structures of the Gupta clusters tend to have lower coordination numbers for the central atoms and, in addition, some of the atoms move outwards in edge capping positions during the DFT relaxation (see, *e.g.*, 19b, 20b and 21b in Fig. 2).

In order to identify particularly stable clusters we calculate the stability function,

$$\Delta^2 E(n) = E(\mathrm{Cd}_{n+1}) + E(\mathrm{Cd}_{n-1}) - 2E(\mathrm{Cd}_n). \qquad (15)$$

here, $E(\mathrm{Cd}_n)$ is the total energy of the Cd_n cluster. A positive value corresponds to a cluster with an enhanced stability (a so called magic number) and often plotting $\Delta^2 E$ against n is useful when interpreting abundance patterns from mass spectroscopic measurements. In Fig. 11 we show $\Delta^2 E(n)$ as a function of n.

Diederich *et al.* have reported the mass spectroscopic results for cadmium clusters that have been produced in ultracold

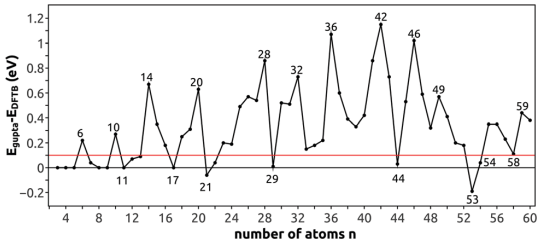

Fig. 10 A comparison of the total energies for the putative global minimum energy structures obtained from the DFT (PBE) re-optimization of the DFTB and Gupta[13] structures. The red line corresponds to a threshold of 0.1 eV in the energy differences.

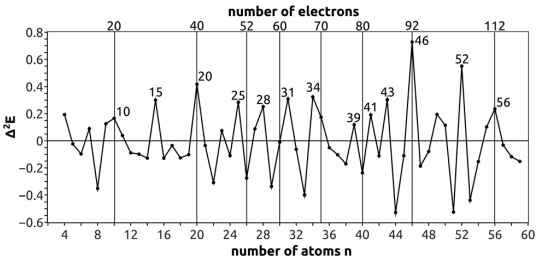

Fig. 11 The stability function as a function of size n for small to medium-sized cadmium clusters. The vertical lines correspond to closed electronic shells according to a spherical jellium model.[21]

helium droplets.[21] They found magic numbers for sizes with 10, 20, 35, 46, and 69 atoms with total 20, 40 70, 92, and 138 valence electrons, respectively. Thereby, they could explain the enhanced stability as being due to the closing of electronic shells as predicted by a spherical jellium model. Our results allow us to assign structures to the most abundant peaks in the mass spectra.

In Fig. 11, magic sizes are found for clusters with 10, 15, 20, 34, 46, 52, and 56 atoms which only partially match the closing of electronic shells according to the spherical jellium model. The maxima at n = 10, 20, 46, and 56 can be explained from the spherical jellium model, but in addition we find, *e.g.*, a maximum for n = 15, a cluster that was found to form the core of clusters between 22 and 36 atoms. However, no experimental study has predicted Cd_{15} to be a magic number. In a theoretical study, Zhao found Cd_{15} to be a magic number with an uncompleted double-icosahedron as the structural motif. The stability of Cd_{20} can most likely be explained by electronic shell closing effects as the cluster itself possesses a compact and disordered motif of PG symmetry C_3. The maxima at n = 25, 28, and 31 correspond to fragments of the highly symmetric Cd_{34} structure with PG T_d and it is remarkable that their greater relative stability seems to correlate with their larger overall symmetry compared to their neighbors as seen in Fig. 4. Despite the possible shell closing for Cd_{35} with its 70 electrons, we found a greater stability for Cd_{34} where the larger geometric symmetry appears to be the dominating effect. Interestingly, Reimann *et al.* showed in their studies on triangular and tetrahedral clusters that such shapes have a strong shell structure and an enhanced stability as it would be predicted by DFT and the jellium model.[47] As mentioned in the introduction, also Johansson *et al.* predicted that tetrahedral, pyramidal-like structures could be possible candidates for the global-minimum-energy structures.[17] In contrast to this, we found a perfect tetrahedral structure for Cd_{34}, which, however, is not of pyramidal shape and Cd_{35} to be the structure of Cd_{34} plus an additional atom. This structure was found to be lower in energy by 0.31 eV than the one found by Johansson *et al.* The large stability of Cd_{46} predicted in our study is in agreement with the experimental results[21,48] and the result of a beneficial electronic-shell closing in combination with a high point-group symmetry (T_d) that gives the cluster an overall spherical shape. For the maxima of $\Delta^2 E$ for Cd_{52} and Cd_{56} the

Published on 13 September 2016. Downloaded by Universitat des Saarlandes on 17/12/2016 20:46:23.

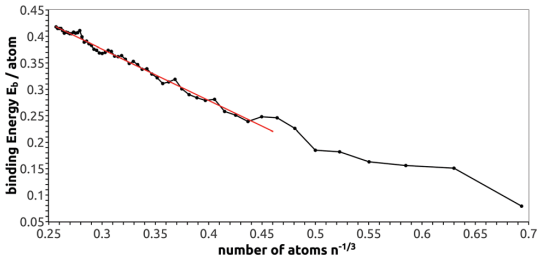

Fig. 12 The binding energy of small to medium-sized Cd clusters as a function of $n^{-1/3}$. Clusters with less than 12 atoms were omitted in the linear fit shown in red.

latter coincides with an electron-shell closing for 112 electrons according to the spherical jellium model.

The binding energy per atom is shown in Fig. 12. From a linear fit of those values for clusters with at least 12 atoms a bulk cohesive energy of 0.67 eV per atom can be identified, which indeed is very close to the value of DFT (PBE) calculations for bulk hcp-Cd (0.69 eV per atom[31]) but still significantly smaller than the experimental value of 1.16 eV per atom. As discussed by Gaston *et al.*, this discrepancy is most likely due to an improper treatment of correlation effects.[31]

3.3 Trends in the electronic properties

The main electronic properties we shall discuss are the HOMO–LUMO gap (ΔHL), the Kubo gap and the ionization potential as a function of size. All these properties may provide also an answer to the question at which size a possible nonmetal-to-metal transition can be observed. Zhao reported such a transition from a DFT study to occur at a size between 7 and 20 atoms and also Diederich *et al.* mentioned that such a transition should be completed for clusters with 20 atoms.[12,21] Fig. 13 shows the calculated HOMO–LUMO gaps for neutral Cd clusters as a function of the size *n*. In some cases, our largest HOMO–LUMO gaps match the sizes for which we find particularly stable clusters. When approximating the ionization potential and the electron affinity through the electronic-orbital energies and, in addition, using a finite-difference approximation, the hardness can be related to the HOMO–LUMO gap. Then, the relation between a large HOMO–LUMO gap and an increased stability can be interpreted as a manifestation of Pearson's principle of maximum hardness.[49] Moreover, this finding is also in accord with that of Harbola who showed for small lithium clusters that the stability that results from electronic rather than geometric effects can be explained through this principle[50] and indeed some of our magic sizes correspond to the closing of electronic shells as discussed above.

It may be difficult to identify the size at which the clusters become metallic from the plot of the HOMO–LUMO gap *vs. n* due to the shortcomings of DFT for this property. Nevertheless, we observe a large decrease of the gap from 3.16 eV for Cd_3 to 0.29 eV for Cd_{60}. The calculated HOMO–LUMO gaps can be further compared to the so-called Kubo gap[51] with the aim of identifying metallicity in the small clusters. Clusters with gaps smaller then the Kubo Gap E_{Kubo} can be considered metallic whereby E_{Kubo} is defined as

$$E_{\mathrm{Kubo}} = \frac{4E_{\mathrm{F}}}{3N_{\mathrm{E}}}. \qquad (16)$$

here E_F is the Fermi energy of bulk hcp-cadmium (E_F = 6.45 eV)[52] and N_E is the number of valence electrons (*i.e.*, 2*n* when considering taking only two valence electrons per cadmium atom into account). In addition to our calculated gaps we added the ones calculated by Zhao[12] for comparison in Fig. 13. Neither our predicted gaps, nor the ones proposed by Zhao drop below the Kubo gap as shown in Fig. 13 for any cluster size. The smallest gap was calculated for the largest considered cluster, *i.e.*, Cd_{60} (ΔHL = 0.285 eV) which is still significantly larger than the Kubo gap predicted for that size (E_{Kubo} = 0.072 eV for Cd_{60}). Hence, according to the Kubo criterion none of the clusters of the present study shows a metallic behavior.

Ruppel and Rademann reported the ionization potentials for Cd_n up to a size of n = 30 atoms.[53] In order to compare their results with ours we calculated the adiabatic ionization potentials (aIPs) for all obtained clusters from the total energy difference between the relaxed neutral and cationic clusters. The results are compared to those of Ruppel and Rademann in Fig. 14. From this figure we may extract several pieces of information also relevant for the identification of a possible metallic behaviour. It is known that the ionization potential of a spherical metal cluster

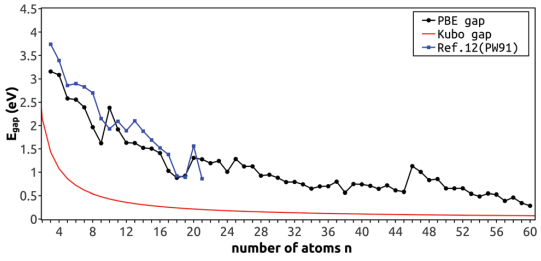

Fig. 13 The Kubo gap (red curve) and the HOMO–LUMO gaps from our GGA-PBE calculations and from the GGA-PW91 calculations of Zhao[12] for cadmium clusters as a function of size *n*.

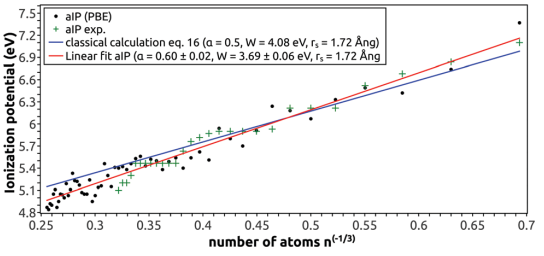

Fig. 14 The calculated adiabatic ionization potentials together with the results from Ruppel and Rademann[53] for small to medium-sized Cd clusters as a function of size *n*. The blue line was calculated from eqn (17) with α = 0.5, W = 4.08 eV, and r_0 = 1.72 Å. The red line corresponds to a linear fit of the calculated adiabatic ionization potentials.

 This journal is © the Owner Societies 2016

Published on 13 September 2016. Downloaded by Universitat des Saarlandes on 17/12/2016 20:46:23.

converges to the work function of a planar metal surface as the size of the cluster tends to infinity. The size dependency of the ionization potential can then be calculated from the work function W plus a positive term that is proportional to the inverse radius of a given cluster with size n multiplied by a constant α,

$$\mathrm{aIP}(n) = W + \alpha \frac{e^2}{4\pi\varepsilon_0 r_0} n^{-1/3}. \quad (17)$$

In our case, the Wigner–Seitz radius r_0 can be calculated from the experimental lattice constant for hcp-Cd[54] and becomes 1.72 Å. The coefficient α that accounts for the size effect was shown to be exactly 0.5 by Seidl and Perdew[55] and any deviation from this value should be caused by quantum effects. Corrections to α are typically expressed as:

$$\alpha = \frac{1}{2} + c. \quad (18)$$

Later, Seidl and Perdew showed that c is about -0.08 for simple metals treated within the spherical jellium model and -0.05 for higher-density metals.[56] They also mentioned that different values for c should be possible in noble or transition metals. However, measurements on small to medium-sized silver clusters, for example, suggested a value of 0.5 for α in Ag_n.[57] Here, we shall use our calculated adiabatic ionization potentials to determine c and W.

From a linear fit to our calculated data, shown in Fig. 14, we extracted values of $\alpha = 0.60 \pm 0.02$ and $W = 3.69 \pm 0.06$ eV. According to eqn (18), then $c = +0.1$ which indicates large quantum effects for the Cd_n clusters or that eqn (17) is inaccurate. Indeed, Svanqvist and Hansen showed that the description of metal clusters by density functional theory in combination with a jellium model fails and they suggested a non-trivial relation between aIPs and W based on the analysis of the experimental results for several metal clusters including cadmium.[58] They reported $\alpha = 0.65 \pm 0.07$ and $W = 3.54 \pm 0.27$ eV based on a fit to the data of Ruppel and Rademann. Both values are in good agreement with our values with a noticeable deviation for both α and W to the results of the simpler model also shown in Fig. 14. Accordingly, the fact that the classical calculation does not provide an accurate description of the results in Fig. 14 implies that it may be difficult to identify metallic behaviour by comparing calculated adiabatic ionization potentials with the results from a simple model that obviously cannot handle sufficiently accurately the more complicated electronic conditions found in cadmium.

To gain information on the bonding in cadmium clusters we study the density of states (DOS) and the contribution of each atomic orbital to the molecular orbitals (shown as partial DOS) using a Mulliken population analysis. The results for Cd_{10}, Cd_{34}, and Cd_{46} as representative examples are shown in Fig. 15.

The 4d and 5s levels are clearly well separated and, therefore, d–s hybridizations appear to be of little importance. However, although the hybridization is weak, it cannot be completely neglected which is why it can be difficult to treat the 4d states as core states, and may also explain why simpler models based, for example, on the jellium model fail in the description of

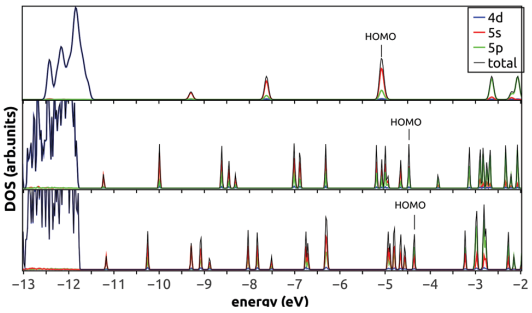

Fig. 15 The density of states (DOS) and partial DOS (calculated from the corresponding Mulliken population analysis) for Cd_{10} (top), Cd_{34} (middle), and Cd_{46} (bottom). The curves were obtained by broadening the orbital eigenvalues with Gaussians with a full width at half-maximum equal to 0.03 eV.

cadmium clusters. The energetically higher-lying orbitals are dominated by s and p contributions as is the case for bulk hcp-Cd where the bands around the Fermi level have mixed s and p character.[59]

4 Conclusions

Our results allow for suggesting a growth pattern for small and medium-sized cadmium clusters which is different to the one proposed through the results from other semi-empirical methods that appear to have a tendency towards over-coordination. By using the DFTB method coupled to a genetic-algorithm followed by an *ab initio* re-optimization with DFT (PBE) we obtained several new candidate structures for the global-minimum-energy structures for sizes up to 60 atoms and we showed that these are not based upon distorted Marks decahedra as proposed earlier. Up to a size of around 36 atoms the growth is dominated by a process in which the atoms are added to a smaller core based on two fused tricapped-trigonal prisms. The first shell is complete at the highly symmetrical Cd_{34} cluster with point group T_d and further addition of atoms leads to clusters with relatively low symmetry but overall spherical shape. This growth process also leads to clusters in which the atoms in the core are arranged similar to what is found in the hcp bulk structure with a maximum number of bulk-like atoms found in Cd_{34}. At a size of 44 atoms, the next core is formed but, maybe surprisingly, the further growth does not proceed so that the number of atoms with a bulk-like environment is maximized. We also found that distorted Marks decahedra can become important with sizes about 53 atoms since at these sizes the cluster structures that have been proposed by others become energetically comparable with those obtained in our study. For sizes greater than 54 atoms we identified clusters with an overall low symmetry but a tendency to maximize the number of hcp-like atoms in the core of the clusters as predicted by the bond-angle analysis. Our candidates for the global minima were also in good agreement with the results obtained from mass spectroscopic analysis where the abundance of several

Published on 13 September 2016. Downloaded by Universitat des Saarlandes on 17/12/2016 20:46:23.

clusters was explained through electron-shell-closing effects. By calculating the adiabatic ionization potentials and comparing these to the results from a spherical jellium model it was not possible to identify the size at which the cadmium clusters can be described as being metallic. This analysis showed also that a simpler model for such systems, based on the spherical jellium model, hardly is capable of capturing all the electronic effects of the Cd_n clusters. However from a comparison of the HOMO–LUMO gaps with the Kubo gap we conclude that cadmium clusters are not metallic up to a size of at least 60 atoms. Finally we found that the chemical bonding is dominated by admixing of s and p states already for sizes as small as 10 atoms, although also the contribution of the 4d orbitals could not be completely neglected.

Acknowledgements

Stephan Kohaut would like to thank N. Louis for computational support and Prof. H. P. Beck and P. Thiel for fruitful discussions. Moreover, the authors would like to thank C^3MSaar for providing the computational resources.

References

1 M. J. Piotrowski, P. Piquini and J. L. F. Da Silva, *Phys. Rev. B: Condens. Matter Mater. Phys.*, 2010, **81**, 155446.
2 Y. Sun, M. Zhang and R. Fournier, *Phys. Rev. B: Condens. Matter Mater. Phys.*, 2008, **77**, 075435.
3 K. Michaelian, M. R. Beltrán and I. L. Garzón, *Phys. Rev. B: Condens. Matter Mater. Phys.*, 2002, **65**, 041403.
4 J. Wang, G. Wang and J. Zhao, *Phys. Rev. A: At., Mol., Opt. Phys.*, 2003, **68**, 013201.
5 H. C. Tran and J. G. Eden, *J. Chem. Phys.*, 1996, **105**, 6771–6777.
6 G. Rodriguez and J. G. Eden, *J. Chem. Phys.*, 1991, **95**, 5539–5552.
7 C. F. Bender, T. N. Rescigno, H. F. Schaefer and A. E. Orel, *J. Chem. Phys.*, 1979, **71**, 1122–1127.
8 M. Helmi, T. Grycuk and G. Roston, *Spectrochim. Acta, Part B*, 1996, **51**, 633–641.
9 M. Czajkowski and J. Koperski, *Spectrochim. Acta, Part A*, 1999, **55**, 2221–2229.
10 M. Strojecki, M. Krośnicki, P. Zgoda and J. Koperski, *Chem. Phys. Lett.*, 2010, **489**, 20–24.
11 F. Cleri and V. Rosato, *Phys. Rev. B: Condens. Matter Mater. Phys.*, 1993, **48**, 22–33.
12 J. Zhao, *Phys. Rev. A: At., Mol., Opt. Phys.*, 2001, **64**, 043204.
13 J. P. K. Doye, *Phys. Rev. B: Condens. Matter Mater. Phys.*, 2003, **68**, 195418.
14 W. Hellmann, R. G. Hennig, S. Goedecker, C. J. Umrigar, B. Delley and T. Lenosky, *Phys. Rev. B: Condens. Matter Mater. Phys.*, 2007, **75**, 085411.
15 F. Yonezawa and H. Tanikawa, *J. Non-Cryst. Solids*, 1996, **205–207**(part 2), 793–796.
16 M. Muñoz, A. Varas, C. Cardenas, J. Rogan and P. Fuentealba, *Comput. Theor. Chem.*, 2013, **1021**, 249–255.
17 M. P. Johansson and P. Pyykkö, *Phys. Chem. Chem. Phys.*, 2004, **6**, 2907–2909.
18 H.-J. Flad, F. Schautz, Y. Wang, M. Dolg and A. Savin, *Eur. Phys. J. D*, 1999, **6**, 243–254.
19 E. Pahl, D. Figgen, A. Borschevsky, K. A. Peterson and P. Schwerdtfeger, *Theor. Chem. Acc.*, 2011, **129**, 651–656.
20 A. Aguado, A. Vega, A. Lebon and B. vonIIssendorff, *Angew. Chem., Int. Ed.*, 2015, **54**, 2111–2115.
21 T. Diederich, T. Döppner, T. Fennel, J. Tiggesbäumker and K.-H. Meiwes-Broer, *Phys. Rev. A: At., Mol., Opt. Phys.*, 2005, **72**, 023203.
22 D. M. Deaven and K. M. Ho, *Phys. Rev. Lett.*, 1995, **75**, 288–291.
23 P. Koskinen and V. Mäkinen, *Comput. Mater. Sci.*, 2009, **47**, 237–253.
24 S. R. Bahn and K. W. Jacobsen, *Comput. Sci. Eng.*, 2002, **4**, 56–66.
25 G. G. Rondina and J. L. F. D. Silva, *J. Chem. Inf. Model.*, 2013, **53**, 2282–2298.
26 M. D. Wolf and U. Landman, *J. Phys. Chem. A*, 1998, **102**, 6129–6137.
27 R. Gehrke and K. Reuter, *Phys. Rev. B: Condens. Matter Mater. Phys.*, 2009, **79**, 085412.
28 D. Porezag, T. Frauenheim, T. Köhler, G. Seifert and R. Kaschner, *Phys. Rev. B: Condens. Matter Mater. Phys.*, 1995, **51**, 12947–12957.
29 G. Seifert, D. Porezag and T. Frauenheim, *Int. J. Quantum Chem.*, 1996, **58**, 185–192.
30 S. Sarkar, S. Pal, P. Sarkar, A. L. Rosa and T. Frauenheim, *J. Chem. Theory Comput.*, 2011, **7**, 2262–2276.
31 N. Gaston, D. Andrae, B. Paulus, U. Wedig and M. Jansen, *Phys. Chem. Chem. Phys.*, 2010, **12**, 681–687.
32 F. Weigend and R. Ahlrichs, *Phys. Chem. Chem. Phys.*, 2005, **7**, 3297–3305.
33 K. L. Schuchardt, B. T. Didier, T. Elsethagen, L. Sun, V. Gurumoorthi, J. Chase, J. Li and T. L. Windus, *J. Chem. Inf. Model.*, 2007, **47**, 1045–1052.
34 M. J. Frisch, G. W. Trucks, H. B. Schlegel, G. E. Scuseria, M. A. Robb, J. R. Cheeseman, G. Scalmani, V. Barone, B. Mennucci, G. A. Petersson, H. Nakatsuji, M. Caricato, X. Li, H. P. Hratchian, A. F. Izmaylov, J. Bloino, G. Zheng, J. L. Sonnenberg, M. Hada, M. Ehara, K. Toyota, R. Fukuda, J. Hasegawa, M. Ishida, T. Nakajima, Y. Honda, O. Kitao, H. Nakai, T. Vreven, J. A. Montgomery Jr., J. E. Peralta, F. Ogliaro, M. Bearpark, J. J. Heyd, E. Brothers, K. N. Kudin, V. N. Staroverov, R. Kobayashi, J. Normand, K. Raghavachari, A. Rendell, J. C. Burant, S. S. Iyengar, J. Tomasi, M. Cossi, N. Rega, J. M. Millam, M. Klene, J. E. Knox, J. B. Cross, V. Bakken, C. Adamo, J. Jaramillo, R. Gomperts, R. E. Stratmann, O. Yazyev, A. J. Austin, R. Cammi, C. Pomelli, J. W. Ochterski, R. L. Martin, K. Morokuma, V. G. Zakrzewski, G. A. Voth, P. Salvador, J. J. Dannenberg, S. Dapprich, A. D. Daniels, Ö. Farkas, J. B. Foresman, J. V. Ortiz, J. Cioslowski and D. J. Fox, *Gaussian09 Revision E.01*, Gaussian Inc., Wallingford CT, 2009.
35 D. J. Wales, J. P. K. Doye and A. Dullweber, *The Cambridge Cluster Database*, http://www-wales.ch.cam.ac.uk/CCD.html.

 This journal is © the Owner Societies 2016

Published on 13 September 2016. Downloaded by Universitat des Saarlandes on 17/12/2016 20:46:23.

36 S. Grimme, J. Antony, S. Ehrlich and H. Krieg, *J. Chem. Phys.*, 2010, **132**, 154104.
37 M. uukomski, J. Koperski, E. Czuchaj and M. Czajkowski, *Phys. Rev. A: At., Mol., Opt. Phys.*, 2003, **68**, 042508.
38 R. Fournier, *J. Chem. Phys.*, 2001, **115**, 2165–2177.
39 H. Li, W. Chen, X. Han, L. Li, Q. Sun, Z. Guo and Y. Jia, *J. Comput. Chem.*, 2015, **36**, 1919–1927.
40 S. Bulusu, S. Yoo and X. C. Zeng, *J. Chem. Phys.*, 2005, **122**, 164305.
41 L.-Z. Zhao, W.-C. Lu, W. Qin, Q.-J. Zang, C. Wang and K. Ho, *Chem. Phys. Lett.*, 2008, **455**, 225–231.
42 A. Stukowski, *Modell. Simul. Mater. Sci. Eng.*, 2012, **20**, 045021.
43 G. J. Ackland and A. P. Jones, *Phys. Rev. B: Condens. Matter Mater. Phys.*, 2006, **73**, 054104.
44 A. Stukowski, *Modell. Simul. Mater. Sci. Eng.*, 2010, **18**, 015012.
45 R. Hoppe, *Z. Kristallogr.*, 1979, **150**, 224410.
46 R. H. Leary and J. P. K. Doye, *Phys. Rev. E: Stat. Phys., Plasmas, Fluids, Relat. Interdiscip. Top.*, 1999, **60**, R6320–R6322.
47 S. M. Reimann, M. Koskinen, H. Häkkinen, P. E. Lindelof and M. Manninen, *Phys. Rev. B: Condens. Matter Mater. Phys.*, 1997, **56**, 12147–12150.
48 K. Rademann, *J. Non-Cryst. Solids*, 1993, **156**, 794–802.
49 R. G. Pearson, *Acc. Chem. Res.*, 1993, **26**, 250–255.
50 M. Harbola, *Proc. Natl. Acad. Sci. U. S. A.*, 1992, **89**, 1036–1039.
51 R. Kubo, *J. Phys. Soc. Jpn.*, 1962, **17**, 975–986.
52 S. Halas and T. Durakiewicz, *J. Phys.: Condens. Matter*, 1998, **10**, 10815.
53 M. Ruppel and K. Rademann, *Chem. Phys. Lett.*, 1992, **197**, 280–285.
54 D. A. Edwards, W. E. Wallace and R. S. Craig, *J. Am. Chem. Soc.*, 1952, **74**, 5256–5261.
55 M. Seidl and J. P. Perdew, *Phys. Rev. B: Condens. Matter Mater. Phys.*, 1994, **50**, 5744–5747.
56 M. Seidl, J. P. Perdew, M. Brajczewska and C. Fiolhais, *J. Chem. Phys.*, 1998, **108**, 8182–8189.
57 C. Jackschath, I. Rabin and W. Schulze, *Z. Phys. D: At., Mol. Clusters*, 1992, **22**, 517–520.
58 M. Svanqvist and K. Hansen, *Eur. Phys. J. D*, 2010, **56**, 199–203.
59 X. W. Sha, D. A. Papaconstantopoulos, M. J. Mehl and N. Bernstein, *Phys. Rev. B: Condens. Matter Mater. Phys.*, 2011, **84**, 184109.

Computational and Theoretical Chemistry xxx (2016) xxx–xxx

Contents lists available at ScienceDirect

Computational and Theoretical Chemistry

journal homepage: www.elsevier.com/locate/comptc

Growth patterns, shapes, and electronic properties of mixed Si_mGe_n clusters with $n + m \leqslant 30$

Stephan Kohaut [a], Philipp Thiel [a], Michael Springborg [a,b,*]

[a] Physical and Theoretical Chemistry, University of Saarland, 66123 Saarbrücken, Germany
[b] School of Materials Science and Engineering, Tianjin University, Tianjin 300072, China

ARTICLE INFO

Article history:
Received 9 October 2016
Received in revised form 30 November 2016
Accepted 1 December 2016
Available online xxxx

Keywords:
Global optimization
Nano-alloys
Semiconductor clusters
Density functional tight-binding

ABSTRACT

A global optimization method in combination with the density-functional tight-binding approach is used to determine all putative global minimum energy structures for mixed silicon-germanium clusters Si_mGe_n with $n + m \leqslant 30$. All obtained structures are re-optimized with first-principles density-functional calculations and the influence of the composition on the shapes is studied. Several extraordinary stable structures are identified and it is shown that the stability correlates with the 'prolateness' of the cluster. However, it was not possible to relate the electronic properties to a single structural property like shape, composition, or local atomic environment.

© 2016 Elsevier B.V. All rights reserved.

1. Introduction

Silicon and silicon-based alloys are still the most widely used semiconductors in our modern electronic-based devices. Not only direct doping of silicon with other elements has been used to alter the optoelectronic properties of silicon nanocrystals [1], but also effects arising from strain are used to optimize the materials properties [2,3]. However, it is well know that additional complications arise when the bulk size regime is left and effects of the finite size of a system are becoming more and more dominating. As the structure of such finite systems are a priori not predictable from bulk properties alone one has to use theoretical methods to assist the experimental findings. However, when searching for the most stable structures, such theoretical approaches are very demanding just for systems consisting of only one element and even more when a second element is added leading to the so called homotops. This is especially true for combinations of elements that show larger differences in their atomic sizes or bulk cohesive energies, as the stability and structure of the resulting mixed clusters then may become influenced by segregation effects. Despite the complicated potential energy surface of pure silicon and germanium nanoclusters, both systems are well studied. Thus, Hellmann et al. pointed out the difficulties in obtaining an agreement between experimental and theoretical results for larger silicon clusters [4]. Several structures are energetically close and may all contribute to the experimental results whereas theory usually will identify only a single structure. The small energy differences between the lowest isomers make it also difficult to assign a specific structural motif for each size except for the smallest clusters, as a change of the theoretical method used [e.g. from Hartree-Fock theory to DFT (density-functional theory) or semi-empirical methods to ab initio methods] also changes the energetical ordering of the isomers. Earlier studies by Raghavachari et al. [5] reported in a Hartree-Fock based study a tetra-capped octahedron with T_d symmetry for Si_{10}, while Ballone et al. found a tetra-capped trigonal prism of C_{3v} symmetry in a DFT (LDA) based study [6]. Inclusion of electronic correlation effects reversed the ordering in the HF study and the C_{3v} structure was now found to be lower in energy than the T_d structure at the MP4 level. Also for Si_{11} differences smaller than 0.1 eV were reported between the first and second isomer at the CCSD(T) level, with the actual value turned out to depend critically on the used basis set [7]. Ho et al. reported from unconstrained DFT (LDA) calculations based on a combination of a genetic algorithm and the simulated annealing method that clusters between 12 and 18 atoms are built from tricapped trigonal prisms (the TTP-motif) and a transition from prolate to more spherical shapes should occur at a size of 19 atoms. However their ion-mobility measurements showed that this transition happens at a slightly larger size [8]. Tekin and Hartke later used several empirical potentials in combination with an unconstrained GA (genetic algorithms) search and found indications of alternative growth

* Corresponding author at: Physical and Theoretical Chemistry, University of Saarland, 66123 Saarbrücken, Germany.
E-mail addresses: s.kohaut@mx.uni-saarland.de (S. Kohaut), thiel.philipp91@gmail.com (P. Thiel), m.springborg@mx.uni-saarland.de (M. Springborg).

http://dx.doi.org/10.1016/j.comptc.2016.12.001
2210-271X/© 2016 Elsevier B.V. All rights reserved.

Please cite this article in press as: S. Kohaut et al., Growth patterns, shapes, and electronic properties of mixed Si_mGe_n clusters with $n + m \leqslant 30$, Comput. Theoret. Chem. (2016), http://dx.doi.org/10.1016/j.comptc.2016.12.001

mechanisms beside the TTP structural motif. They mentioned that the results are strongly dependent upon the parameters used entering the empirical potential [9]. Jackson et al. used a method that imitates the big bang to gain candidate structures with the help of a density-functional-based tight-binding approach (DFTB) that were later re-optimized with ab initio DFT (PBE) in an unbiased way for sizes between 20 and 27 atoms and showed that these clusters are not based on the TTP-motif. They found excellent agreement to experimental results based on ion-mobility measurements and concluded that the structural motifs found for medium-sized clusters are indeed controlled by thermodynamic effects [10]. The work by Lyon et al. gave direct experimental evidence that the structures of smaller clusters are based on a pentagonal bipyramidal building block with a change to the TTP motif for larger clusters [11]. Yoo and Zeng added a new structural building unit into the discussion, the so called 'six/six' motif, a sixfold-puckered hexagonal ring Si_6 plus a six-atomic tetragonal bipyramid Si_6. The relative stability between these motifs were revealed to be dependent on the computational approach whereby the CCSD (T) calculations slightly favored the 'six/six' motif over the TTP one [12]. Later, a fourth structural type, consisting of 'Y-shaped' three-arm structures, where each arm is a small-sized magic cluster (Si_6, Si_7, or Si_{10}) were described by the same authors and shown to be competitive in energy compared to the TTP, the 'six-six', and the spherical motifs [13]. In contrast to the case of silicon clusters, ion mobility measurements suggested a prolate growth pattern for germanium clusters with up to 70 atoms [14]. Theoretical calculations supported the experimental finding that prolate structures are favoured over compact ones for Ge_n with n up to around 40 atoms [15,16], while smaller clusters with 12–20 atoms adopted the TTP motif [17]. An extension of the 'six-six' motif was reported by Yoo and Zeng consisting of a 'six-nine' (a puckered-hexagonal-ring Ge_6 attached to a tri-capped trigonal prism Ge_9) and six-ten motif and they suggested that these motifs are present in most of the energetically low-lying isomers of Ge_n [15]. Quin et al. predicted the presence of the 'Y-shaped' three-arm structural motif also in medium to larger germanium clusters with 34–39 atoms. Larger clusters favoured plate-like structures that were built from smaller magic-sized clusters like Ge_9 and Ge_{10} [18]. Li et al. recently found that van-der-Waals interactions may have a strong influence on the bonding strength between the fragments of the smaller magic-sized Ge_n clusters and that these fragments are connected by bulk-like Ge_6, Ge_9, or Ge_{10} units via strong covalent bonds [19]. Shvartsburg et al. compared the growth patterns of silicon and germanium clusters and concluded that both systems start to form different clusters for sizes as small as 13 atoms, but both clusters are based on TTP subunits [20]. Lu et al. showed that the building blocks consisting of 6, 7, and 10 atoms in germanium clusters can acquire more energy from their corresponding bulk energy than the ones in the silicon system and, therefore, the transition from a prolate to a spherical shape happens for smaller sizes in silicon than in germanium.

Compared to the pure clusters which have been extensively studied both theoretically and experimentally there are much less results reported in the literature for binary SiGe cluster. Most of the investigations were restricted to smaller sizes or specific stoichiometries. Thus, Wang and Chao studied neutral and ionic Si_m-Ge_n clusters with $m+m \leqslant 12$ with DFT (B3LYP) and CCSD(T) methods and reported that the silicon atoms preferred to occupy higher-coordinated sites than the germanium atoms. They also found negative mixing energies for all considered sizes for both neutral and ionic clusters although the cationic clusters proved to be more stable than the anionic ones [21]. Li et al. reported that the mixed clusters at smaller sizes followed the structural motifs known from the pure clusters and predicted Si_4Ge_6 and Si_6Ge_4 to be magic numbers of particularly high stability [22]. Marim et al. showed that the average inter-atomic distances in small clusters with up to 7 atoms increased linearly with the germanium content and that such a behavior can be understood as the clusters analogue of Vegard's law. ur Rehman et al. used the parametrized density-functional tight-binding method and studied pure and mixed clusters of silicon and germanium with up to 44 atoms [23,24]. They restricted the ratio of silicon to germanium to 1:1 and could show that the silicon atoms occupy the higher coordinated sites and that Si–Si and Si–Ge bonds dominated the cigar-shaped SiGe clusters. Various similarity indices were calculated by them to compare the structures of the mixed clusters with the pure ones of similar size and in the first work [23], they found that the mixed systems have a greater similarity to the pure silicon clusters than to their germanium counterparts, whereas the later, improved definition of a similarity index indicated that the mixed clusters were equally different from the pure ones of the same size [24].

In this work we shall address several issues of mixed silicon-germanium clusters that have not been studied earlier. We shall begin with a comparison of the structures of pure silicon and germanium clusters and use several geometric descriptors to identify differences and similarities during the growth of the pure clusters. To study the influence of different compositions on the shape and the distribution of silicon and germanium within each cluster we determine subsequently the putative global minimum energy structures for all Si:Ge ratios with a density functional tight-binding/genetic algorithm (DFTB/GA) approach and re-optimized all structures with the DFT (PBE) method. In order to identify compositions of greater stability we shall calculate two criteria for stability. The excess energy that is defined by comparing with either the bulk cohesive energies or the total energies of the pure clusters of similar size and a local stability that compares the stability of neighboring sizes and compositions without any connections to the bulk or pure structures. Finally, we shall explore the dependency of the electronic properties, especially of the HOMO-LUMO gap (HL-gap), on the size and composition of all obtained clusters.

2. Computational methods

2.1. The global optimization procedure

In the present work we used a genetic algorithm (GA) derived from the 'cut-and-splice' procedure introduced by Deaven and Ho [25] together with the density-functional tight-binding method as implemented in the Hotbit code [26] to determine the putative total-energy-minima structures of the Si–Ge clusters. Our own genetic algorithm was linked to the atomic simulation environment (ASE) code introduced by Bahn and Jacobsen to benefit from their large number of useful methods within their central 'Atoms' object [27].

For the genetic algorithm we use a population of 10 members and construct the first generation in each calculation by placing the atoms randomly within a cubic box of volume V that scales with the number of atoms as

$$V_{box} = m \cdot \frac{a_{Si}^3}{4} + n \cdot \frac{a_{Ge}^3}{4} \quad (1)$$

with a_{Si} and a_{Ge} being the corresponding experimental lattice constants of the diamond structures of Si (a = 5.431 Å) [28] and Ge (a = 5.658 Å) [29] followed by a local relaxation to the next local minimum on the potential energy surface (pes). In contrast to traditional algorithms in which only small parts of a generation are subjected to a crossover, selection and mutation procedure to evolve a given structure to the global minimum, we allowed all population members within each generation to form one offspring that is

Please cite this article in press as: S. Kohaut et al., Growth patterns, shapes, and electronic properties of mixed Si_mGe_n clusters with $n+m \leqslant 30$, Comput. Theoret. Chem. (2016), http://dx.doi.org/10.1016/j.comptc.2016.12.001

constructed as follows: First, each of two parents is cut along a random plane. Next, the two parts of the two parent clusters are interchanged and subsequently translated in the *x*-, *y*-, or *z*-direction until no atom from one part is closer than the bond length of the dimer to an atom of the other part. The offspring clusters are relaxed to their next local total-energy-minima and added to the current pool of structures. This step is then followed by a mutation procedure in which all current parents are mutated by one of the following operations that all are applied with equal probability:

- Random displacements of all atoms with a Gaussian-distributed step-size [30].
- Permutation of two atomic species to explicitly include homotops of the same structural motif in the search process.
- A twinning mutation in which two halfparts of a cluster are rotated relative to each other by a small random angle [31].
- An etch-add process in which a randomly picked atom is removed and placed next to another atom [31].

All mutation procedures were followed by a local relaxation to the next local minimum and the mutants were added to the pool of structures. To prohibit a premature convergence to another local total-energy minimum than that of the global minimum, we accepted a newly created mutant only if its energy was lower than the structure with the lowest energy already contained in the pool or if its energy was larger than a predefined energy threshold (here a value of $\Delta = 0.1$ eV was used) with regard to the structure with the lowest energy found so far. The size of the pool members was afterwards reduced to a size of nine members by applying a simple tournament with five participants while as the last member we used the unmodified structure with the lowest energy from the preceding crossover and mutation cycle (correspond to 'elitism'). The algorithm used in this study was considered to be converged if the energy of the putative global minimum energy structure did not change for 100 consecutive generations and we repeated every global optimization run for every composition for three times starting every run from randomly created starting structures. All acquired clusters that were lowest in energy for every considered stoichiometry were later used as starting points for DFT re-optimizations.

2.2. Parametrization of the DFTB method

Within the DFTB method, the total energy relative to that of non-interacting neutral atoms can be approximated as a sum of the energies of all occupied orbitals minus that of the neutral, non-interacting atoms, E_{BS}, plus a term due to Coulomb interactions E_{Coul} and a pairwise repulsive potential U_{rep} [32,33],

$$E = E_{BS} + E_{Coul} + U_{rep}. \tag{2}$$

At the lowest level of approximation (corresponding to the non-SCC DFTB) we neglect interactions that result from charge fluctuations and ignore E_{Coul}. U_{rep} can then be parametrized and adjusted to reproduce either experimental or ab initio results once E_{BS} is known for a given set of structures.

Using an LCAO approach the orbitals are expanded in a minimal set of atomic-centered non-orthogonal basis functions,

$$\psi_i(\vec{r}) = \sum_v c_{vi}\phi_v(\vec{r}). \tag{3}$$

The Kohn-Sham eigenvalue equations are solved for an effective potential V_{eff} to determine E_{BS} as the sum over the eigenvalues of all occupied orbitals,

$$\hat{H}\psi_i(r) = \varepsilon_i\psi_i(r), \tag{4}$$

with

$$\hat{H} = \hat{T} + V_{eff}. \tag{5}$$

Here, $\hat{T}$ is the kinetic-energy operator.

Substitution of (3) into (4) gives the eigenvalue equation

$$\sum_v c_{vi}(H_{vi} - \epsilon_i S_{vi}) = 0 \tag{6}$$

with

$$H_{vi} = \langle\phi_v|\hat{H}|\phi_i\rangle \tag{7}$$

and

$$S_{vi} = \langle\phi_v|\phi_i\rangle. \tag{8}$$

The elements of H_{vi} and S_{vi} are determined from calculations on diatomic molecules for a whole set of interatomic distances by using the Slater-Koster rules and stored in a table. Thereby it is assumed that the effective potential can be written as a superposition of atomic potentials

$$V_{eff}(\vec{r}) = \sum_n V_n(|\vec{r} - \vec{R}_n|) \tag{9}$$

with $\vec{R}_n$ being the position of the nth atom. Moreover, $V_n(r)$ is the potential of the free, isolated, nth atom, $V_n^{(0)}(r)$, augmented by a short-ranged confining potential that leads to the typical contraction of the orbitals when passing from the isolated atom to a compound,

$$V_n(r) = V_n^{(0)}(r) + \left(\frac{r}{r_0}\right)^2. \tag{10}$$

For r_0 we use for Si 3.57 bohr and for Ge 3.92 bohr to get the best agreement between the DFTB calculated electronic band structures and the ones derived from ab initio DFT calculations using the PBE functional.

Subsequently, we assume that

$$\langle\phi_v|\hat{T} + V_{eff}|\phi_i\rangle = \begin{cases} \langle\phi_v|\hat{T} + V_n|\phi_i\rangle & \text{for } \phi_v,\ \phi_i \text{ both on atom } n \\ \langle\phi_v|\hat{T} + V_n + V_m|\phi_i\rangle & \text{for } \phi_v,\ \phi_i \text{ on atoms } n \neq m \\ 0 & \text{otherwise.} \end{cases} \tag{11}$$

U_{rep} is determined by fitting to accurate results from ab initio DFT (PBE) calculations. Specifically, in the present work we minimized the force differences $|F^{DFT} - F^{DFTB}|$ for the dimers with a smoothing spline as explained by Koskinen and Mäkinen [26]. The thereby obtained derivative, U'_{rep}, was integrated to give the repulsion potential and tested against results from DFT calculations.

2.3. Ab initio density-functional calculations

All subsequent ab initio DFT calculations for the clusters were performed using the PBE functional for exchange and correlation as implemented in the Siesta program [34]. The scalar-relativistic pseudopotentials for silicon and germanium were created within the norm-conserving Troullier-Martins scheme for Si ($3s^{2.0}3p^{2.0}3d^{0.0}4f^{0.0}$) and Ge($4s^{2.0}4p^{2.0}4d^{0.0}4f^{0.0}$) valence configurations with cut-off values of 1.75, 1.94, 2.09, and 2.09 bohr for silicon and 1.98, 1.98, 2.39 and 2.39 bohr for germanium, respectively. A basis set of DZP quality together with a soft-confinement potential was used within a split-valence scheme in which the first basis function was fixed to a cut-off of 8.5 bohr and the split-norm r_m of the second basis function was optimized variationally for the bulk structures and for dimers of silicon and

Please cite this article in press as: S. Kohaut et al., Growth patterns, shapes, and electronic properties of mixed Si_mGe_n clusters with $n + m \leqslant 30$, Comput. Theoret. Chem. (2016), http://dx.doi.org/10.1016/j.comptc.2016.12.001

Table 1
Details of the DZP basis set used in this study. All values are in bohr.

	Si_{3s}	Si_{3p}	Si_{3d}	Ge_{4s}	Ge_{4p}	Ge_{4d}
r_c	8.50	8.50	4.67	8.50	8.50	4.89
r_m	4.94	4.92	–	5.15	5.01	–

Table 2
Summary of the performance of the DZP basis set for bulk and dimer structures (without zpe or BSSE corrections) compared to other reported DFT-PBE, CCSD(T), or experimental results [37–43]. $a_X, B_X, E_X^{coh}, d_{X-Y}$, and E_{X-Y}^{bind} represent the lattice constant, bulk modulus and cohesive energy per atom for crystalline X, and the bond length and the binding energy for the X-Y dimer, respectively.

Property	DZP(PBE)	PBE	Exp.
a_{Si} [Å]	5.507	5.49, 5.466	5.431, 5.416
B_{Si} [GPa]	85.0	89.2, 88.6	99.2
E_{Si}^{coh} [eV]	4.547	4.56	4.681, 4.62 ± 0.08
d_{Si-Si} [Å] ($^3\Sigma_g^-$)	2.308	2.281, 2.30	2.246
E_{Si-Si}^{bind} [eV]	1.78	1.685	1.64, 1.605
a_{Ge} [Å]	5.820	5.759,	5.640, 5.658
B_{Ge} [GPa]	56.4	59.7	75.8
E_{Ge}^{coh} [eV]	3.677	3.73	3.863
d_{Ge-Ge} [Å] ($^3\Sigma_g^-$)	2.431	2.409 [CCSD(T)]	2.368
E_{Ge-Ge}^{bind} [eV]	1.566	1.355 [CCSD(T)]	1.332
d_{Si-Ge} [Å] ($^3\Sigma$)	2.371	2.339 [CCSD(T)]	-
E_{Si-Ge}^{bind} [eV] [Å] ($^3\Sigma$)	1.667	1.433 [CCSD(T)]	1.531

germanium at the corresponding experimental lattice constants of Si and Ge [28,29], bond lengths of the dimer from either experiment (Si) [35] or from calculations at the CCSD(T) level (Ge) [36]. Afterwards, we added one *p*-type polarization function to both basis sets and fine-tuned their cut-off values for the bulk and dimer structures. The final values for the basis set are summarized in Table 1. For the sake of completeness, the results for bulk Si and Ge and the dimers are shown in Table 2 and compared to other results reported in the literature.

The candidates for the global minimum were placed in a large cubic box with a side length of 22.0 Å, and re-optimized with the optimized DZP basis set using one $\vec{k}$ point at the Γ point. A mesh-cutoff of 500 Ry was used for the real space grid. Atomic positions in all calculations were optimized to a residual force smaller than 0.01 eV/Å with the conjugate-gradient algorithm as implemented in Siesta.

2.4. Quantifying structural similarity

In the present work we shall be particularly interested in identifying structural similarity, also in order to be able to study growth patterns and structural motifs. For this purpose, it is very useful to define a quantitative measure for the similarity of two objects which we determined as follows.

First, we compare the structures of the pure silicon and germanium clusters one by one and define a similarity index that gives an information about how similar the two structures are. The calculation of such indices were carried through with a genetic algorithm with three translations x, y, z, three rotational angles θ, ϕ, ρ, an overall scaling factor r and an inversion-flag i as the genome and the sum of squared nearest-neighbor distances as target function. Starting with two clusters, *A* and *B*, all positions of *B* are translated by the vector (x, y, z). The resulting cluster is then rotated by θ around the *z*-axis, by ϕ around the resulting *x*-axis and by ρ around the resulting *z*-axis. Every resulting position vector is then multiplied by r $(-r)$ for $i = 1$ $(i = -1)$. Subsequently, for each atom a in cluster *A* the closest atom $b(a)$ in cluster *B* is chosen and the distance $d(a, b(a))$ is calculated. Similarly, for every atom b in *B*, the closest atom $a(b)$ in cluster *A* is identified and the distance $d(b, a(b))$ is calculated. The function

$$q = \frac{1}{2n}\left(\sum_{i=1}^{n} d^2(a_i, b(a_i)) + \sum_{i=1}^{n} d^2(b_i, a(b_i))\right) \tag{12}$$

where n is the number of atoms in the smaller cluster and $\{a_i\}, \{b_i\}$ are the sequences of atoms in both clusters, ordered by distance to their closest atoms in the other cluster, is chosen as the target function.

Once the smallest value of q has been identified, the similarity index S is defined as

$$S = \frac{1}{1 + \frac{\sqrt{q}}{u_l}} \tag{13}$$

where u_l is a unit length, which is arbitrarily chosen to be the average nearest-neighbor distance in cluster *A*. Two clusters are considered similar, if S is greater than 0.9 and they are considered dissimilar if S is smaller than 0.8. Values in between indicate deformational configurations.

In the genetic algorithm an initial population containing different values for the above-mentioned eight parameters is randomly generated and used to produce children. For each child, two parents are chosen randomly whereby the values for each of the seven parameters are obtained randomly from the two parents. Additionally, a set of mutants is generated, which start from a parent structure that is modified in random genome entries by a random number drawn from a Gaussian, uniform or χ^2 distribution within appropriate ranges. To construct the next generation, all candidates are placed in a pool and a tournament is run that decides which genome modification is allowed to be passed to the follow-

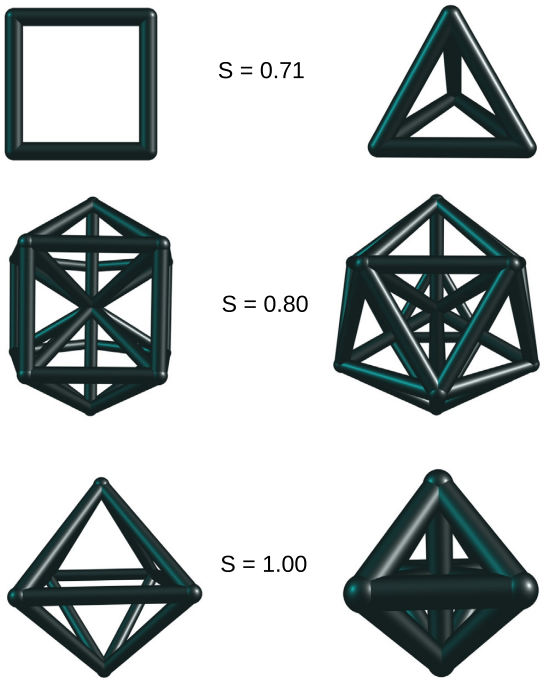

Fig. 1. A comparison of different structural motifs through their calculated similarity indices, *S*.

Please cite this article in press as: S. Kohaut et al., Growth patterns, shapes, and electronic properties of mixed Si_mGe_n clusters with $n + m \leqslant 30$, Comput. Theoret. Chem. (2016), http://dx.doi.org/10.1016/j.comptc.2016.12.001

ing generation. The whole procedure is stopped, when the lowest value of q has not changed after a predefined number of generations. In typical runs a population size of 40 was found to be appropriate to reach the global minimum within 2000 generations.

To give an impression about the meaning of the calculated index S, we give the results in Fig. 1 for three different cases, i.e., for the comparison of a tetrahedron with a square (completely different structural motif, upper row), followed by a comparison of an icosahedron (that often is found as structural motif in many clusters with a size of 13 atoms) with a decahedron of the same size (middle row), and, finally, for the comparison of a perfect octahedron with a octahedron for which all bond lengths were scaled by a factor of 0.5 (bottom row).

Finally, we add that through the present definition of S it is possible to identify structural similarities not only between two clusters but also between clusters and parts of a crystal. Moreover, the present approach shares many similarities with the one introduced earlier [24] but without the pitfall that the latter may be trapped in local minima for q.

3. Results

3.1. Pure silicon and germanium clusters

Both in order to demonstrate the reliability of our approach and for the sake of comparison with the results for the mixed clusters we start our discussion with an analysis of the obtained structures for the pure silicon and germanium clusters with up to 30 atoms.

In Fig. 2 we show the calculated similarity indices for the comparison of the pure silicon with the pure germanium clusters. Already for smaller clusters, differences in the structures of the two cluster sets are recognizable. For Ge_8, we find a face-capped pentagonal-bipyramid in agreement with the findings of other studies [44], while for Si_8 we obtain a bi-face-capped octahedron of point group (pg) C_{2h} which was also the result of several other authors including experimental studies [20,45–47].

An icosahedral fragment was found for Ge_9 whereas Si_9 was identified to be a bi-face-capped pentagonal bipyramid. The occurrence of the icosahedral motif for the Ge_n clusters is the source of structural differences (a drop in S) between the Si_n and Ge_n clusters for n around 12–13. We located, as several other authors, a distorted icosahedron for Ge_{12} and a face-capped icosahedron for Ge_{13} as the structures with the lowest energy, whereas the icosahedral motif could not be identified for Si_{12} or Si_{13} [8].

For larger clusters with more than 14 atoms the two types of pure clusters do not share many structural similarities. The TTP motif was found to be present in the silicon clusters up to a size of 14 atoms while larger structures did not follow a clear growth pattern as can be seen in Fig. 4. We found several structural motifs including ones that are based on bilayers as is the case for Si_{16}, Si_{20}, Si_{22}, and Si_{23}, as well as more spherical clusters with highly coordinated silicon atoms in the center like in Si_{17}, Si_{18}, Si_{19}, Si_{21}, Si_{24} and in clusters larger than Si_{25}.

Our optimized silicon clusters are not always those of the global minimum-energy found in other studies, which can be related to inaccuracies in the computational approach, whereby it is hardly possible to make conclusive statements about which structures indeed are those of the global total-energy-minima. Thus, Marim et al. showed in their TB/GA calculations that spherical silicon clusters are competitive in energy compared to more prolate structures already for sizes as small as $n = 14$ [48]. This agrees well with our results where we did not find a sharp transition from prolate to spherical clusters within the observed size range and instead an oscillatory behavior between both shapes. Moreover, Yoo et al. [49] reported the transition to happen between 21 and 25 atoms which is qualitatively in agreement with our findings as well as those of other authors who have reported spherical silicon clusters for sizes below $n = 20$ [50,8].

The TTP motif was found to be the dominating one in our results for smaller germanium cluster as it can be seen in Fig. 3. Up to a size of $n = 18$ our optimized structures are in agreement with the other reported putative global minimum energy results mentioned in Section 1. For larger clusters, the icosahedral motif appears besides the TTP one and we find tricapped trigonal prisms attached to icosahedra in several larger clusters with the TTP motif disappearing for the largest clusters of the present study. A distorted icosahedron as a building unit was not found by other authors for the lowest-energy structures and, therefore, we examined whether this structural motif indeed leads to low-energy structures by re-optimizing both our optimized structures and those by Li et al. with DFT (PBE) calculations [19].

Indeed, as can be seen in Fig. 5 our structures with an icosahedron as building unit, are predicted to be slightly higher in energy than the TTP-based structures proposed by Li et al. although the differences are small (just some few 0.01 eV/atom) so that both structural motifs most likely will be observed in experimentally produced clusters. We add that independent of this difference, all germanium clusters in the size range of the present study are

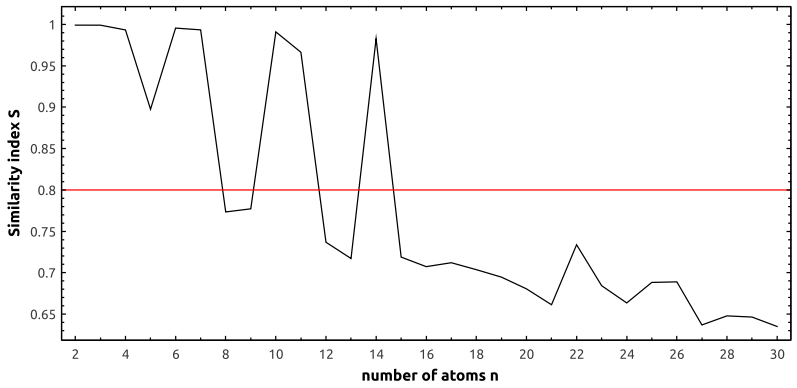

Fig. 2. Calculated similarity indices S for the comparison of pure silicon with the pure germanium clusters of the same size. The horizontal red line indicates the value of S below which two clusters show two completely different structural motifs. (For interpretation of the references to color in this figure legend, the reader is referred to the web version of this article.)

Please cite this article in press as: S. Kohaut et al., Growth patterns, shapes, and electronic properties of mixed Si_mGe_n clusters with $n + m \leqslant 30$, Comput. Theoret. Chem. (2016), http://dx.doi.org/10.1016/j.comptc.2016.12.001

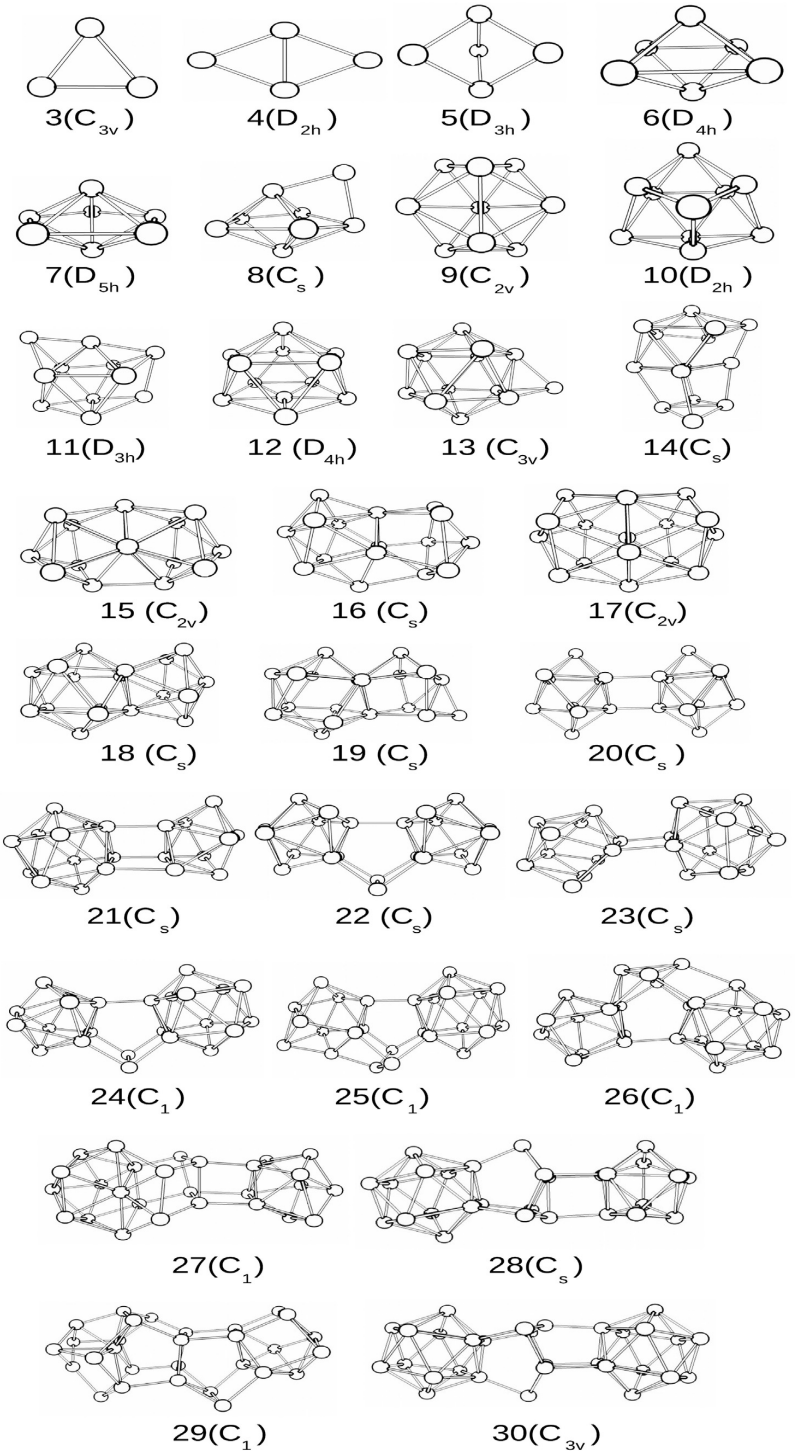

Fig. 3. The obtained putative global-minimum-energy structures for the pure Ge_n clusters with their corresponding point-group symmetries.

Please cite this article in press as: S. Kohaut et al., Growth patterns, shapes, and electronic properties of mixed Si_mGe_n clusters with $n + m \leqslant 30$, Comput. Theoret. Chem. (2016), http://dx.doi.org/10.1016/j.comptc.2016.12.001

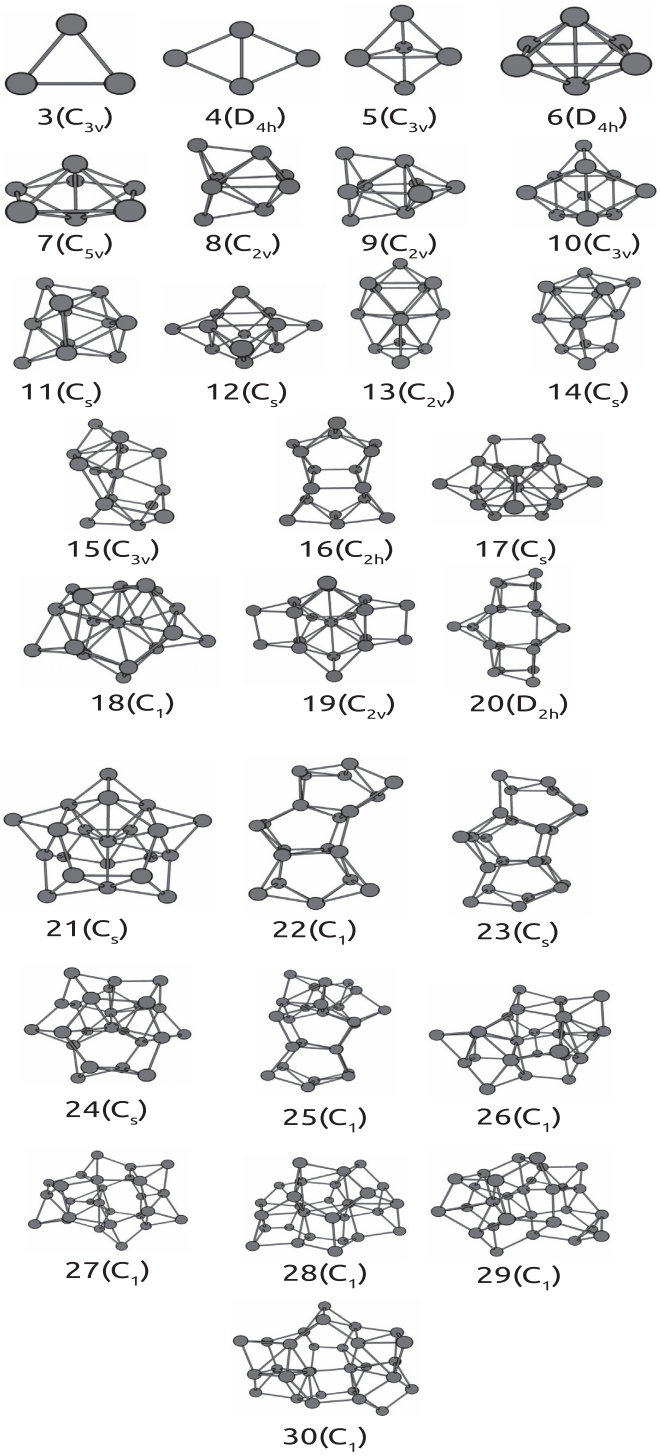

Fig. 4. The obtained putative global-minimum-energy structures for the pure Si_n clusters with their corresponding point-group symmetries.

Please cite this article in press as: S. Kohaut et al., Growth patterns, shapes, and electronic properties of mixed Si_mGe_n clusters with $n + m \leqslant 30$, Comput. Theoret. Chem. (2016), http://dx.doi.org/10.1016/j.comptc.2016.12.001

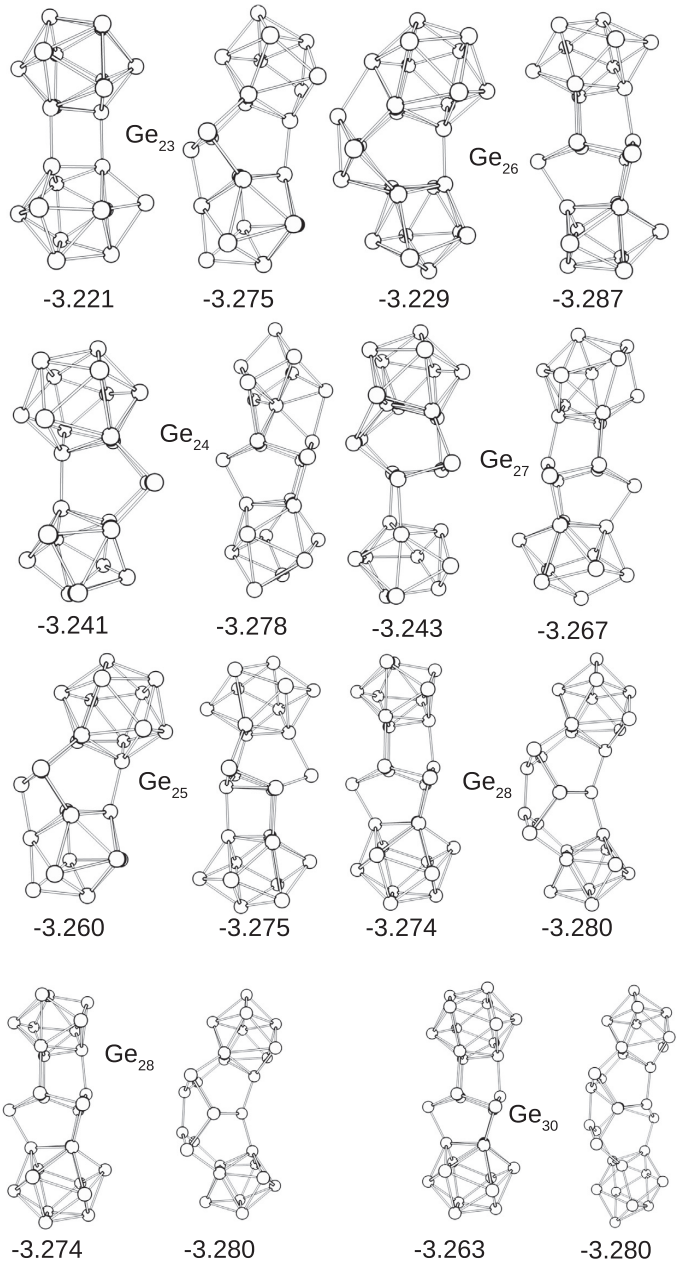

Fig. 5. Comparison of our obtained putative global minimum-energy structures for selected Ge_n clusters (left clusters) with those reported by Li et al. [19] (right clusters). Also shown are their calculated binding energy/atom (in eV/atom) from the DFT (PBE) calculations.

found to be prolate, whereas several earlier studies based on tight-binding approaches resulted in either spherical and amorphous-like clusters or clusters that were essentially prolate but did not show any of the known building units [23,51,24,44]. In order to obtain further information on the shape, we use methods that are widely used in the description of the shapes of polymer chains and are typically based on the calculation of the gyration tensor [52,53]. The gyration tensor $\underline{\underline{G}}$ is defined as

$$\underline{\underline{G}} = \frac{1}{N}\begin{pmatrix} \sum_i (x_i - x_0)^2 & \sum_i (x_i - x_0)(y_i - y_0) & \sum_i (x_i - x_0)(z_i - z_0) \\ \sum_i (x_i - x_0)(y_i - y_0) & \sum_i (y_i - y_0)^2 & \sum_i (y_i - y_0)(z_i - z_0) \\ \sum_i (x_i - x_0)(z_i - z_0) & \sum_i (y_i - y_0)(z_i - z_0) & \sum_i (z_i - z_0)^2 \end{pmatrix} \tag{14}$$

where (x_i, y_i, z_i) are the coordinates of atom i within a cluster and (x_0, y_0, z_0) the average of all positions of the cluster. Diagonalizing

Please cite this article in press as: S. Kohaut et al., Growth patterns, shapes, and electronic properties of mixed Si_mGe_n clusters with $n + m \leqslant 30$, Comput. Theoret. Chem. (2016), http://dx.doi.org/10.1016/j.comptc.2016.12.001

$\underline{\underline{G}}$ leads to three eigenvalues $(\lambda_1, \lambda_2, \lambda_3)$ that we will sort in descending order, $\lambda_1 \geqslant \lambda_2 \geqslant \lambda_3$. From those, the radius of gyration R^2 that represents the average squared distance from each atom to the center of mass (with all masses set to unity) can be determined,

$$\mathrm{Tr}(\underline{\underline{G}}) = \lambda_1 + \lambda_2 + \lambda_3 = R^2. \tag{15}$$

Further shape descriptors that also can be obtained from the eigenvalues of $\underline{\underline{G}}$ are the relative shape anisotropy κ^2 which describes both the symmetry and dimensionality of a structure, and lies between 0 (corresponding to the case that all atoms are arranged spherically symmetric or distributed uniformly on any platonic solid) and 1 (corresponding to a case in which all atoms are placed along a straight line) and defined as

$$\kappa^2 = \frac{3}{2}\frac{\mathrm{Tr}(\underline{\underline{G}})^2}{[\mathrm{Tr}(\underline{\underline{G}})]^2} = 1 - 3\frac{\lambda_1\lambda_2 + \lambda_2\lambda_3 + \lambda_3\lambda_1}{(\lambda_1 + \lambda_2 + \lambda_3)^2}, \tag{16}$$

as well as the asphericity parameter b that quantifies the deviation from sphericity,

$$b = \lambda_1 - \frac{1}{2}(\lambda_2 + \lambda_3). \tag{17}$$

Finally, we can quantify the acylindricity c which is non-negative, and zero only for $\lambda_2 = \lambda_1$

$$c = \lambda_2^2 - \lambda_1^2. \tag{18}$$

and analyze the ratio $\frac{\lambda_1}{\lambda_3}$ that gives additional information about the prolateness of an object.

Although the Si_n and Ge_n clusters do not share the same structural motifs for smaller clusters, they nevertheless are very similar in their overall shape up to a size of $n = 17$. For κ^2, shown in Fig. 6, we found values close to zero for smaller structures, which indicates that these clusters are close to being spherical. At a size of

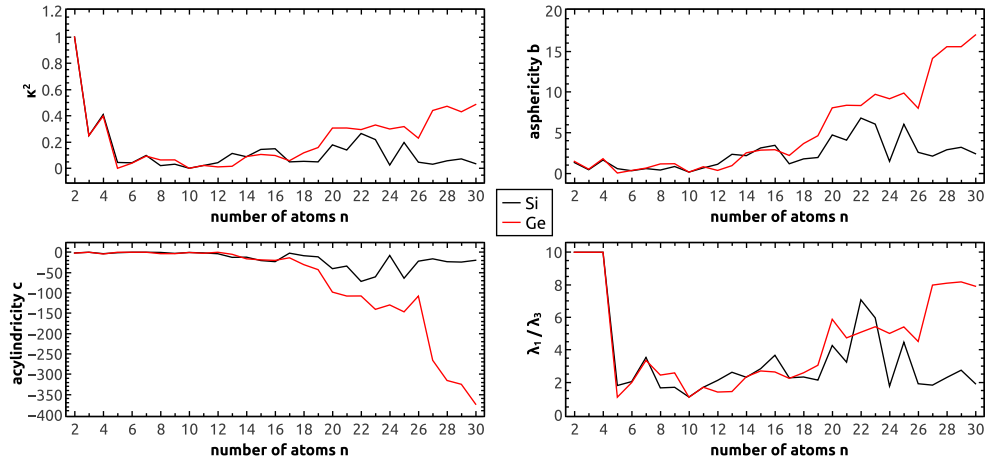

Fig. 6. The relative shape anisotropy κ^2 (top-left panel), asphericity b given in Å^2 (top-right panel), acylindricity given in Å^4 c (bottom-left panel) and the ratio $\frac{\lambda_1}{\lambda_3}$ (bottom-right panel) for pure Si_n and Ge_n clusters as a function of n.

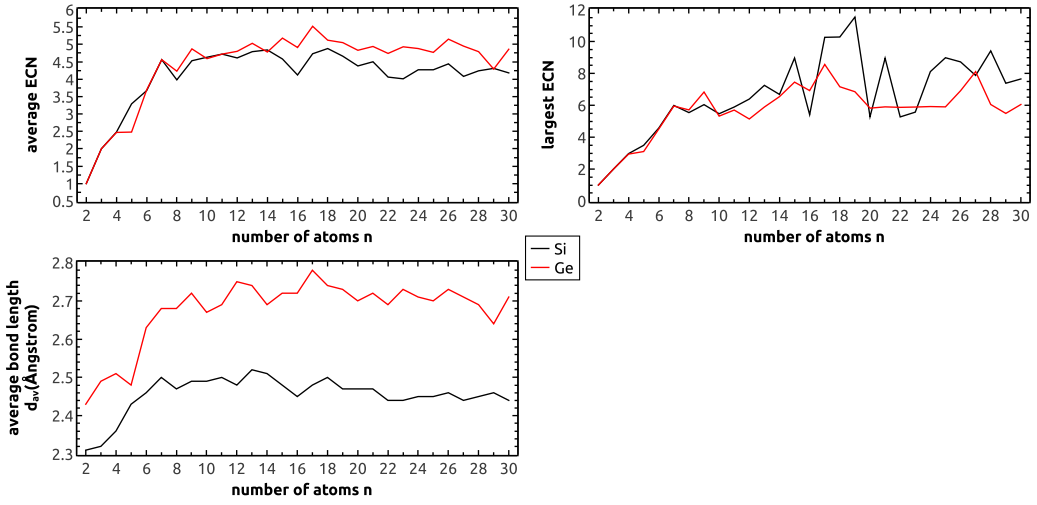

Fig. 7. The average effective coordination number ECN (top-left panel), the largest ECN (top-right panel) and the average bond length d_{av} (bottom-left panel) calculated from Hoppe's approach for pure silicon and germanium clusters as a function of the size n.

Please cite this article in press as: S. Kohaut et al., Growth patterns, shapes, and electronic properties of mixed Si_mGe_n clusters with $n + m \leqslant 30$, Comput. Theoret. Chem. (2016), http://dx.doi.org/10.1016/j.comptc.2016.12.001

$n = 17$, the germanium clusters show an increase in κ^2 while for the silicon structures, κ^2 reaches a maximum for Si_{22} and then decreases to values below 0.1 with a single exception for Si_{25}. The difference in the shape for larger clusters is also recognizable in the asphericity parameter b shown in Fig. 6 as b, like κ^2, increases throughout the complete series of germanium clusters of the present work, whereas, for silicon clusters, we find a behavior very similar as before with a maximum at Si_{22} and Si_{25} followed by a decrease of b to a value of around 2.4 Å. The large difference for κ^2 and b for the two elements for the largest sizes indicates a greater difference in the growth motifs of the larger clusters of silicon and germanium.

To get further information on the deviations from the spherical symmetry, especially for the germanium clusters, we study the acylindricity and the ratio $\frac{\lambda_1}{\lambda_3}$, both shown in Fig. 6. Except for Si_{10}, Ge_{10}, and Ge_5, which are the most spherical clusters, we note that also smaller clusters are not perfectly spherically symmetric as the ratio $\frac{\lambda_1}{\lambda_3}$ is larger than 1 even in those smaller structures. The acylindricity in germanium decreases while the ratio $\frac{\lambda_1}{\lambda_3}$ simultaneously increases, which indicates that the germanium clusters indeed possess a prolate shape, at least for the sizes of the present study. The shape transition in silicon clusters from prolate to spherical is not sharp and we observe oscillations in all shape descriptors. However, we find the most prolate structures for silicon for the sizes 22–25 after which a sharp drop to more spherical shapes occurs which is qualitatively in agreement to the proposed transition range of Li et al. between 21 and 25 atoms [49].

For a more complete understanding of the structural properties of the clusters we shall analyze the local environment of each atom in every cluster which will become particularly important for the mixed clusters to be discussed later. To calculate the effective coordination number (ECN) and average bond lengths (d_{av}) we use an approach described by Hoppe et al. [54] and tested for example by Chou et al. for clusters [55]. According to this, the average bond length for atom i is defined as

$$d_{av}^{i} = \frac{\sum_{j=1}^{N} d_{ij} e^{[1-(d_{ij}/d_{av}^{i})^{6}]}}{\sum_{j=1}^{N} e^{[1-(d_{ij}/d_{av}^{i})^{6}]}} \tag{19}$$

with N being the total number of atoms in the cluster. It is seen that d_{av}^{i} has to be determined iteratively. Thereby, d_{av}^{i} is initially taken as the shortest nearest-neighbor distance for atom i and the final value

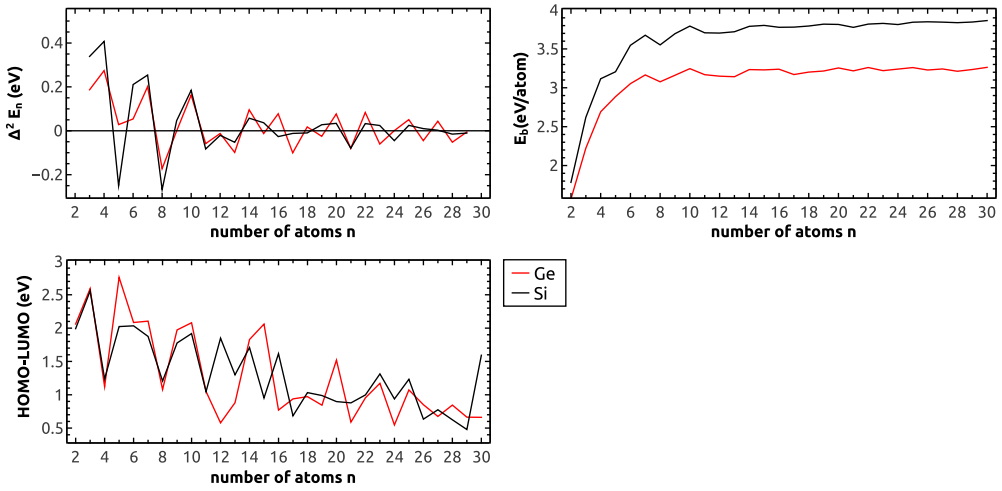

Fig. 8. The second stability function (top-left panel), the binding energy E_b (top-right panel) and the HOMO-LUMO gap (bottom-left panel) for pure silicon and germanium clusters as a function of the size n.

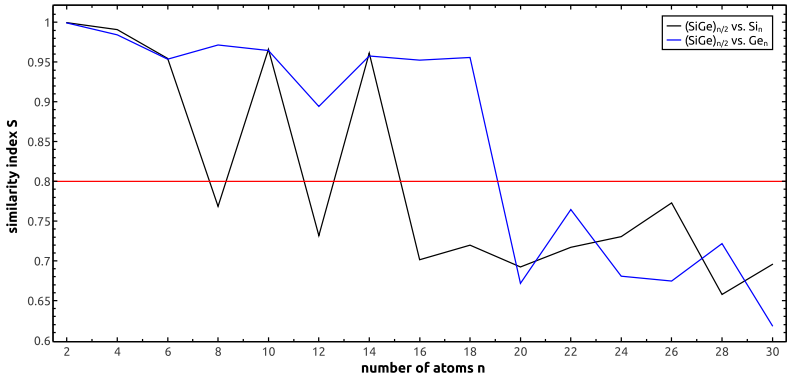

Fig. 9. The similarity index S calculated from the comparison of mixed $(SiGe)_{n/2}$ with pure silicon or germanium clusters of size n.

Please cite this article in press as: S. Kohaut et al., Growth patterns, shapes, and electronic properties of mixed Si_mGe_n clusters with $n + m \leqslant 30$, Comput. Theoret. Chem. (2016), http://dx.doi.org/10.1016/j.comptc.2016.12.001

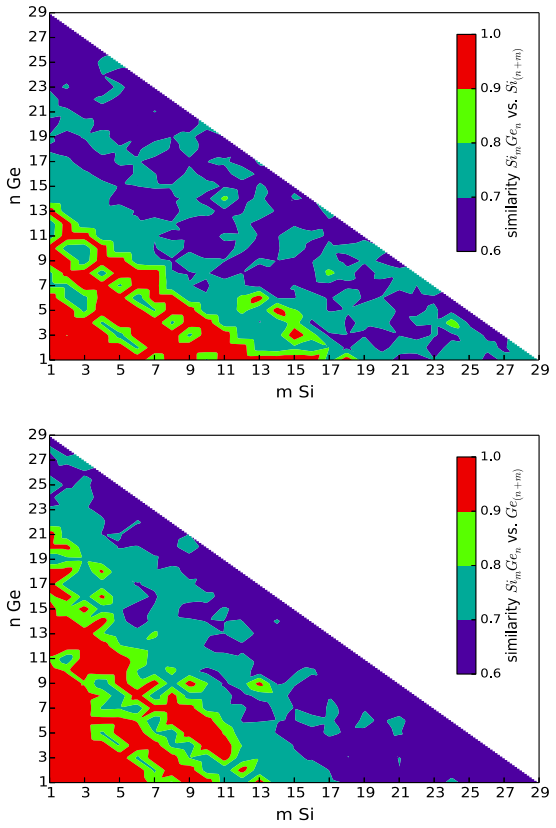

Fig. 10. The similarity index S calculated from the comparison of mixed Si_mGe_n with pure silicon or germanium clusters of size $(n+m)$.

obtained self consistently using a convergence criterion of 10^{-4} Å. Subsequently, an effective coordination number ECN of atom i defined as

$$\mathrm{ECN}(i) = \sum_{j=1}^{N} e^{[1-(d_{ij}/d_{\mathrm{av}}^{i})^{6}]} \tag{20}$$

can be introduced.

Averages of ECN and d_{av}^{i} for all atoms of a given cluster can then be obtained. In Fig. 7 we show the average ECN, the largest calculated ECN and the average bond lengths, respectively, for pure Si_n and Ge_n clusters. In general we observe a larger mean coordination number in germanium clusters, although the plot of the largest ECN shows that some of the silicon atoms in the spherical clusters can reach very large coordination numbers up to 12. The average bond length in the silicon clusters is overall about 9% smaller than in the germanium cluster and in neither of them the average bond length reaches the bond length found in the bulk.

Finally we shall address the issues of stability and electronic properties of the pure clusters. Stability can be either understood in a chemical sense and is usually associated with large gaps between the highest occupied and the lowest unoccupied molecular orbital (the so-called chemical hardness) or in relative stabilities between two clusters that are differing in size or structure. The latter definition typically coincidences with results from mass spectroscopy and can be calculated for the example of pure clusters from

$$\Delta^2 E(n) = E(\mathrm{X}_{n+1}) + E(\mathrm{X}_{n-1}) - 2E(\mathrm{X}_n) \tag{21}$$

with $E(\mathrm{X})$ being the total energy of the system X. This function is shown in Fig. 8 and demonstrates that there are certain cluster sizes with increased stability compared to neighboring sizes (the so-called magic clusters) and that these sizes coincide for $n \leqslant 14$ for the two elements but differ for larger cluster sizes.

For Si_n we can identify magic sizes for $n = 4, 7, 10, 14, 15, 19, 23$ and 25 while for Ge_n we find $n = 4, 7, 10, 14, 16, 20, 22, 25$ and 26 to be of special stability. These magic numbers correlate with the

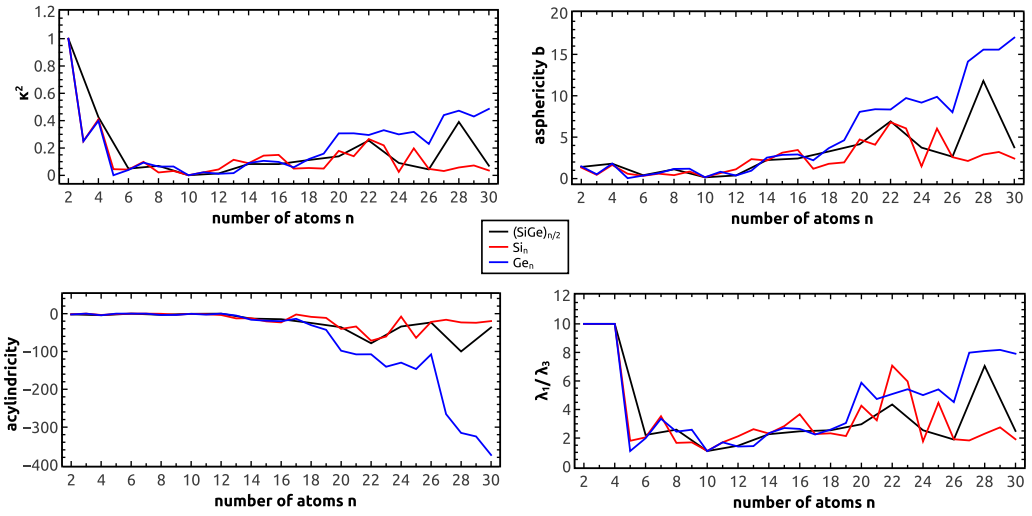

Fig. 11. The asphericity b given in Å^2 (top-left panel), the shape anisotropy κ^2 (top-right panel), the acylindricity c given in Å^4 (bottom-left panel), and the prolateness parameter $\frac{\lambda_1}{\lambda_3}$ (bottom-right panel) of mixed $(SiGe)_{n/2}$ clusters as a function of the number of atoms n.

Please cite this article in press as: S. Kohaut et al., Growth patterns, shapes, and electronic properties of mixed Si_mGe_n clusters with $n+m \leqslant 30$, Comput. Theoret. Chem. (2016), http://dx.doi.org/10.1016/j.comptc.2016.12.001

occurrence of the Ge_{10} and Si_{10} subunit which is of great stability for both elements like in Ge_{20} and Ge_{22} which were predicted to contain two interconnected Ge_{10} units. For silicon it is noteworthy that spherical clusters like Si_{17}, Si_{18} and, according to the shape descriptor, the most spherical, larger cluster Si_{24} are not among the magic-sized clusters. Alternatively, one may study the binding energy per atom, E_b, that is also shown in Fig. 8. This figure shows that any silicon cluster has a higher binding energy than the germanium cluster of the same size but also that each of the curves has visible maxima at certain values of n, which indicates an enhanced stability at those sizes. A large HL-gap is not automatically associated with high stability as it can be seen by comparing the maxima between the HL-gap and the stability function, both shown in Fig. 8. While there can be maxima seen in both curves for Si_{14}, Si_{15}, Si_{23}, and Si_{25} we notice discrepancies for example for the clusters Si_5, Si_4, and Si_{20}. Also the spherical clusters Si_{17}, Si_{18}, Si_{21}, Si_{24}, and Si_{26} have in general a smaller HL-gap as the prolate structures. For germanium we observe that the TTP unit in larger clusters does not lead to structures with a large HL-gap compared with their neighboring clusters, see, e.g., Ge_{20} and Ge_{22}.

3.2. Mixed SiGe clusters

Next, we shall study the properties of mixed Si_mGe_n clusters. Rehman et al. [23] reported a greater similarity of $(SiGe)_n$ clusters with $n = 1$—22 to silicon clusters of the same size which, however, was modified in a later study where a more reliably similarity indicator was introduced [24]. Therefore, we start our analysis by calculating the similarity indices for the comparison of our obtained clusters with pure silicon and germanium clusters of equal size. As can be seen in Fig. 9, the present study gives a comparable similarity between the Si_{2n} and Ge_{2n} clusters on the one hand and the Si_nGe_n clusters on the other hand.

In addition, the abrupt drops found for the smaller pure Si clusters are not recovered for the pure Ge clusters. In fact, when comparing the mixed Si_mGe_n clusters with the pure Si_{m+n} and the pure Ge_{m+n} clusters (see Fig. 10) there is a smaller tendency for the mixed clusters to be more similar to the pure Ge clusters than to the pure Si clusters, at least up to a total size of 23 atoms.

In contrast to this, our results suggest that silicon has a greater influence than germanium on the overall shape of the 1:1 mixed clusters as one, for instance, can see from the shape descriptors shown in Fig. 11. Thus, as the upper panel shows, the mixed clusters are more spherical than their pure germanium counterparts but similar to the case for the pure silicon clusters. An exception is found for $n = 28$ which was identified to be highly prolate. But also for the other properties in Fig. 11, the $(SiGe)_{n/2}$ clusters show shape behaviors much more similar to those of the Si_n than to the Ge_n clusters.

When considering the shape properties of the complete set of Si_mGe_n clusters of the present study, we obtain the results shown in Fig. 12. We see that for the asphericity b, the shape anisotropy κ^2, the acylindricity c, and the prolateness parameter $\frac{\lambda_1}{\lambda_3}$ in general all are largest for the Ge rich clusters and smallest for the Si rich clusters and that there is a more or less smooth transition in between. Thus, Ge rich clusters tend to have less regular shapes than Si rich clusters.

The plot of the effective coordination numbers (ECN) of either silicon or germanium in the $(SiGe)_{n/2}$ clusters in Fig. 13, show the interesting result that Si in general is higher coordinated than Ge in the mixed clusters and that the Si coordination then is even larger than in the pure Si_n clusters, whereas that Ge coordination is larger in the mixed than in the pure clusters. Thus, silicon tends

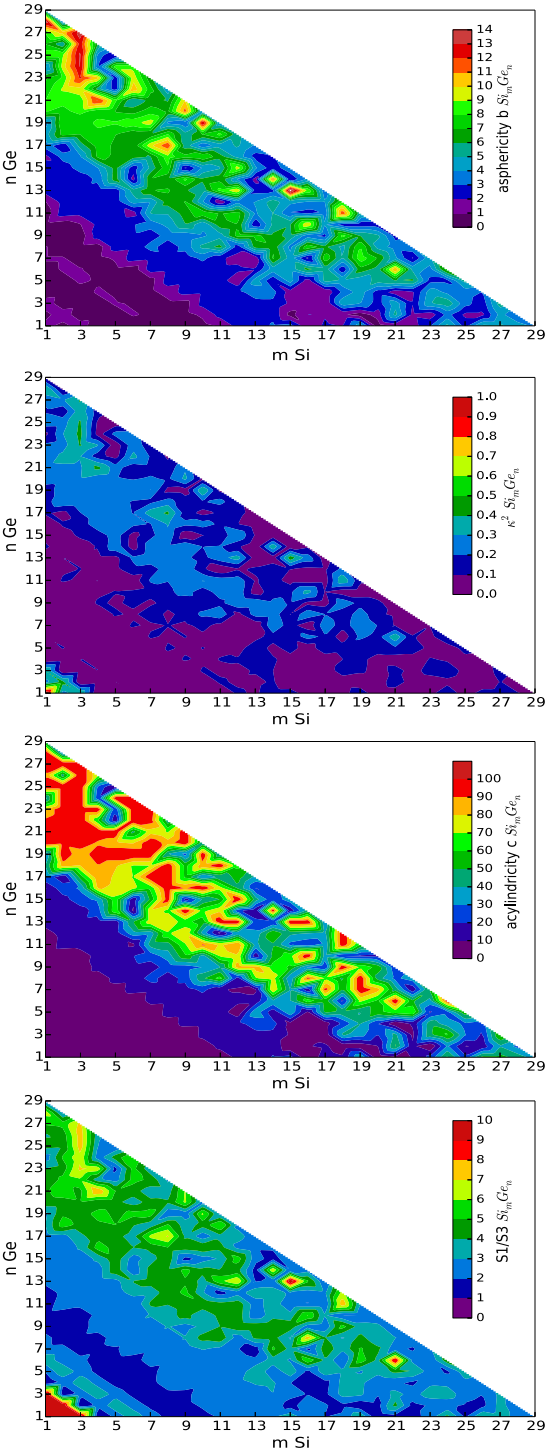

Fig. 12. The asphericity b in Å^2 (top-row), the shape anisotropy κ^2 (second-row), the acylindricity c in Å^4 (third-row), and the prolateness parameter $\frac{\lambda_1}{\lambda_3}$ (bottom-row) of mixed Si_mGe_n clusters as functions of (m, n).

Please cite this article in press as: S. Kohaut et al., Growth patterns, shapes, and electronic properties of mixed Si_mGe_n clusters with $n + m \leqslant 30$, Comput. Theoret. Chem. (2016), http://dx.doi.org/10.1016/j.comptc.2016.12.001

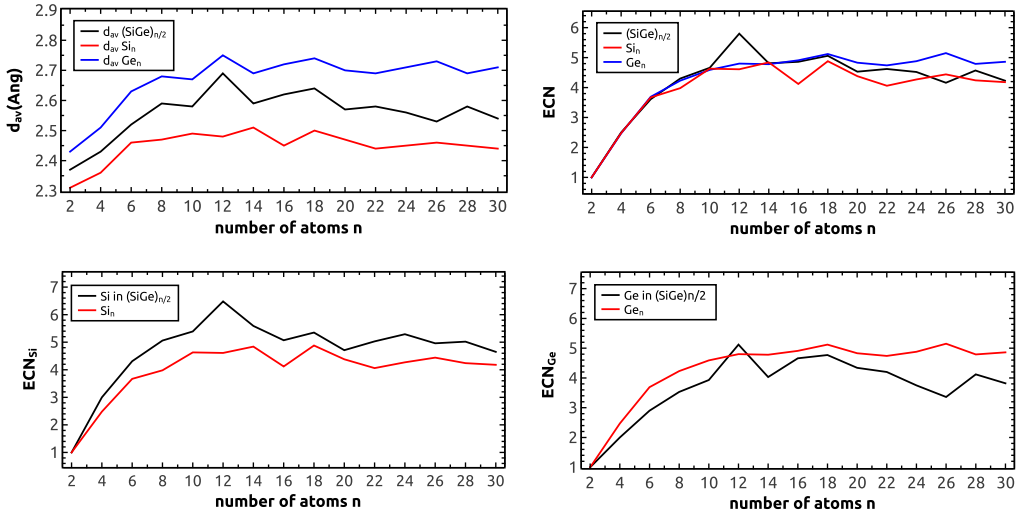

Fig. 13. The average bond length d_{av} (top-left panel), average effective coordination number ECN (top-right panel), average ECN of Si in $(SiGe)_{n/2}$ (bottom-left panel) and average ECN of Ge in $(SiGe)_{n/2}$ (bottom-right) as a function of the number of atoms n.

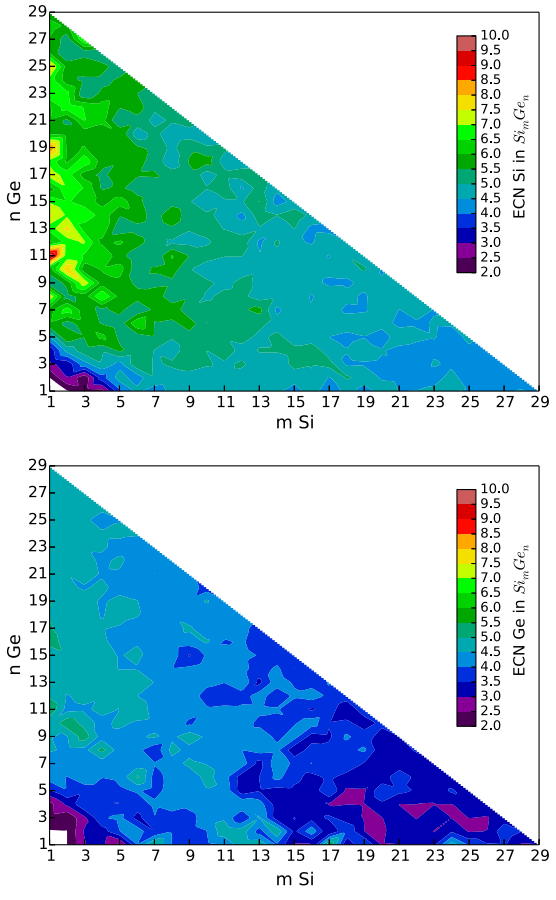

Fig. 14. The effective coordination number of Si (top) and Ge (bottom) in Si_mGe_n as a function of (m, n).

to occupy higher-coordinated positions than germanium in the mixed clusters with equal Si:Ge ratios, a finding that is in agreement with results from other authors who have reported a segregation of germanium to the surface [23,56–58]. This behavior prevails for all other Si:Ge ratios as can be seen in Fig. 14: the average effective coordination number of the germanium atoms is always smaller than for the silicon atoms with the smallest values found for germanium in silicon-rich clusters. Fig. 14 also shows that the germanium sites are hardly ever over-coordinated compared to the bulk, while the opposite is true for silicon which occupies positions with average effective coordination numbers occasionally as large as 9 in the germanium-rich clusters.

Next we shall study the effect of a gradual exchange of silicon by germanium. For this, Tarus et al. [56] reported a linear growth of the average bond length within mixed clusters with an increasing content of germanium and explained such a behavior as an analogue of Vegard's rule for nanoalloys. As shown in Fig. 15, also our results are in agreement with having a roughly linear dependence of the average bond length on the germanium content although the results suggest that this rule should be taken with some caution. In particular for the smallest clusters the average bond lengths turn out to be smaller than this simple rule would suggest (these results are the lowest ones in Fig. 15).

Further information on the energetic properties of the clusters can be obtained from the excess energy E_{exc}. This is not uniquely defined but here we will use the definition

$$E_{exc} = E(Si_mGe_n) - \left[\frac{m}{n+m}E(Si_{m+n}) + \frac{n}{n+m}E(Ge_{m+n})\right]. \quad (22)$$

Fig. 16 shows E_{exc} for all the clusters of the present study. In contrast to the case of the macroscopic solids where complete miscibility for any m/n is known, our results indicate that smaller mixed clusters do not show such a behavior if the criterion for miscibility is based on a comparison to the stability of the pure clusters of equal size. Unfortunately, this prediction may depend on the definition of E_{exc}, so that particularly stable pure clusters may imply that mixing is not possible for those sizes. Another criterion for stability compares the second difference in energy for neighboring clusters as a function of the number of atoms. The second

Please cite this article in press as: S. Kohaut et al., Growth patterns, shapes, and electronic properties of mixed Si_mGe_n clusters with $n + m \leqslant 30$, Comput. Theoret. Chem. (2016), http://dx.doi.org/10.1016/j.comptc.2016.12.001

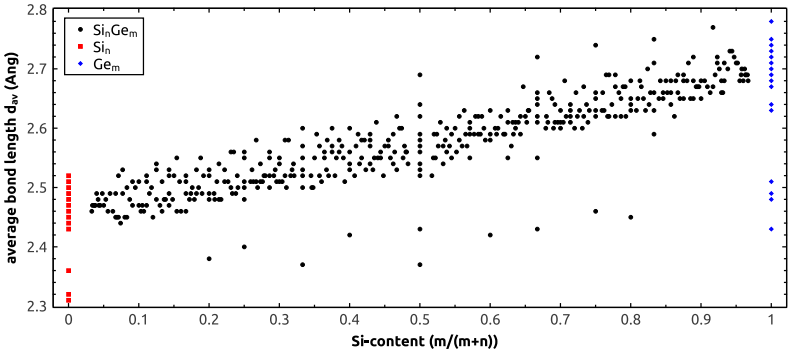

Fig. 15. The average bond length in mixed Si_mGe_n clusters as a function of $\frac{m}{m+n}$.

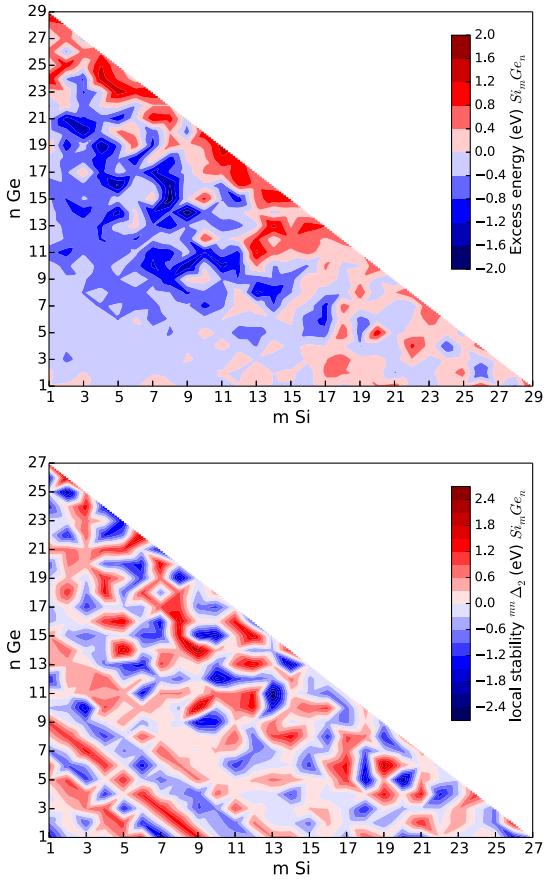

Fig. 16. The excess energy E_{exc} (top layer) and the local stability $^{mn}\Delta_2$ (bottom layer) of mixed Si_mGe_n clusters as a function of the size up to $n + m = 30$.

difference in energy is uniquely defined for monoatomic clusters and is used to compare the stability of those with abundance patterns from mass spectroscopic analysis. However in bimetallic systems the stability of clusters does not solely depend upon the number of atoms N but is also a function of the composition (m, n) and therefore several definitions can be proposed. Based on all eight neighbors of a cluster with composition (n, m) we decided to study the following stability function, different from what we have done in earlier studies [59]

$$^{mn}\Delta_2 = \frac{1}{8}\sum_{p,q=-1}^{1}[E(m+p, n+q) - E(m, n)] \tag{23}$$

with $E(m + p, n + q)$ being the total energy of the $Si_{m+p}Ge_{n+q}$ cluster.

This function is shown in Fig. 16. Smaller mixed clusters up to a total size of about 15 atoms show pronounced odd-even oscillations with a greater stability found for the odd clusters irrespective of their composition. For larger clusters we do not see such an odd-even oscillation and the resulting difference in the relative stabilities among certain clusters seem to be a product of several properties beside their composition. In Tables 3 and 4 we show for every size the clusters with the most stable and unstable compositions. Interestingly, for most of the stable compositions we found a coincidence between the two criteria that were used to define the cluster stability. This is surprising as the stability that was calculated from the excess energy E_{exc} is typically biased by the stability of the pure structures.

Unfortunately, it is difficult to perform an extensive statistical analysis due to the small number of data. However several qualitative results can be obtained by analyzing the data shown in Table 3. We extracted the median of the silicon content from a plot of the cumulative frequency for both cases and found a smaller value in the stable clusters (0.32) compared to their unstable counterparts (0.5) as shown in Fig. 17. Clusters with a silicon ratio in that range were found to be prolate (see Fig. 12) with a greater average ECN for the silicon atoms (Fig. 14) which would naturally be associated with a core-shell formation. In the next paragraph we show through several segregation descriptors that clusters with a lower silicon content indeed tend to avoid a mixing of both elements in favor of segregation. In addition, it can be noticed (see the ball-stick models of all stable compositions in Fig. 20 and of all the unstable ones in the supporting informations) that the TTP motif is over-represented among the pool of the most stable clusters while most of the larger unstable compositions are spherical and amorphous-like, especially the larger mixed clusters. Beside the TTP-motif we also found Y-shaped clusters (Si_2Ge_{26}) and structures that belong to the "six-six" class of motifs ($Si_{14}Ge_8$, Si_9Ge_{14}, Si_8Ge_{16}, Si_8Ge_{17}, $Si_{12}Ge_{15}$ and Si_9Ge_{20}). Only three clusters out of all the most stable compositions can be described as being amorphous ($Si_{21}Ge_9$, $Si_{19}Ge_6$ and $Si_{26}Ge_2$) with all of them having large silicon contents. In Table 4 one can also notice that there are no unstable compositions

Please cite this article in press as: S. Kohaut et al., Growth patterns, shapes, and electronic properties of mixed Si_mGe_n clusters with $n + m \leqslant 30$, Comput. Theoret. Chem. (2016), http://dx.doi.org/10.1016/j.comptc.2016.12.001

Table 3
The most stable compositions (m,n) according to Eqs. (22) and (23) for Si_mGe_n clusters within the size range $N = n + m \leqslant 30$.

N	$^{mn}\Delta_2$	E_{exc}	N	$^{mn}\Delta_2$	E_{exc}
4	(2,2)	(1,3)	18	(6,12)	(7,11)
5		(2,3)	19	(9,10)	(9,10)
6	(5,1)	(2,4)	20	(2,18)	(7,13)
7	(6,1)	(2,5)	21	(5,16)	(5,16)
8		(1,7)	22	(4,18)	(14,8)
9	(1,8)	(1,8)	23	(9,14)	(9,14)
0	(9,1)	(3,7)	24	(8,16)	(8,16)
11		(4,7)	5	(19,6)	(8,17)
12	(1,11)	(1,11)	26	(8,18)	(8,18)
13		(2,11)	27	(12,15)	(12,15)
14	(4,10)	(4,10)	28	(2,26)	(26,2)
15	(14,1)	(3,12)	29		(9,20)
16	(4,12)	(4,12)	30		(21,9)
17	(10,7)	(7,10)			

Table 4
The most unstable compositions (m,n) according to Eqs. (22) and (23) for Si_mGe_n clusters within the size range $N = n + m \leqslant 30$.

N	$^{mn}\Delta_2$	E_{exc}	N	$^{mn}\Delta_2$	E_{exc}
2	(1,1)	(1,1)	17	(6,11)	(15,2)
3	(1,2)	(1,2)	18	(9,9)	(17,1)
4		(3,1)	19	(6,13)	(17,2)
5	(3,2)	(3,2)	20	(12,8)	(18,2)
6			21	(18,3)	(18,3)
7			22	(10,12)	(10,12)
8	(7,1)	(7,1)	23	(18,5)	(18,5)
9	(3,6)	(8,1)	24	(13,11)	(13,11)
10			25	(20,5)	(1,24)
11	(1,10)		26	(4,22)	(22,4)
12	(6,6)	(6,6)	27	(2,25)	(14,13)
13	(3,10)	(11,2)	28	(4,24)	(5,23)
14			29		(4,25)
15	(6,9)	(13,2)	30		(1,29)
16	(15,1)				

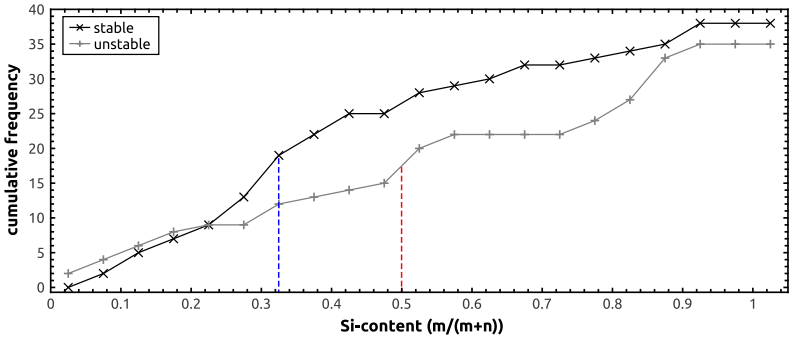

Fig. 17. A plot of the cumulative frequency of the silicon content $\frac{m}{n+m}$ for the most stable and unstable compositions. The dashed lines in blue and red represent the median of the corresponding data sets. (For interpretation of the references to color in this figure legend, the reader is referred to the web version of this article.)

shown according to the defined stability criteria for some of the compositions ($m + n$ = 6, 7, 10 and 14). All of these sizes showed a negative excess energy E_{exc} or a positive local stability for all calculated compositions and therefore we did not consider them as being unstable.

To check if a segregation (e.g. core-shell structures) exists we calculate the bond order σ for every cluster, defined as

$$\sigma = \frac{N_{Si-Si} + N_{Ge-Ge} - N_{Si-Ge}}{N_{Si-Si} + N_{Ge-Ge} + N_{Si-Ge}} \tag{24}$$

While a positive value of σ indicates segregation, a negative value would be found for mixed and onion-like distributions of the atoms. A σ close to zero would correspond to disorderly mixed clusters. The calculated bond order σ for all compositions and sizes is shown in Fig. 18. It demonstrates that for germanium- or silicon-rich clusters a tendency towards segregation exists, whereas the clusters with approximately equal ratios of silicon and germanium tend to mix. Further information about a possible trend to form a core-shell system can be obtained by calculating the ratio of the average radial distance of both elements to the geometric center within a

Please cite this article in press as: S. Kohaut et al., Growth patterns, shapes, and electronic properties of mixed Si_mGe_n clusters with $n + m \leqslant 30$, Comput. Theoret. Chem. (2016), http://dx.doi.org/10.1016/j.comptc.2016.12.001

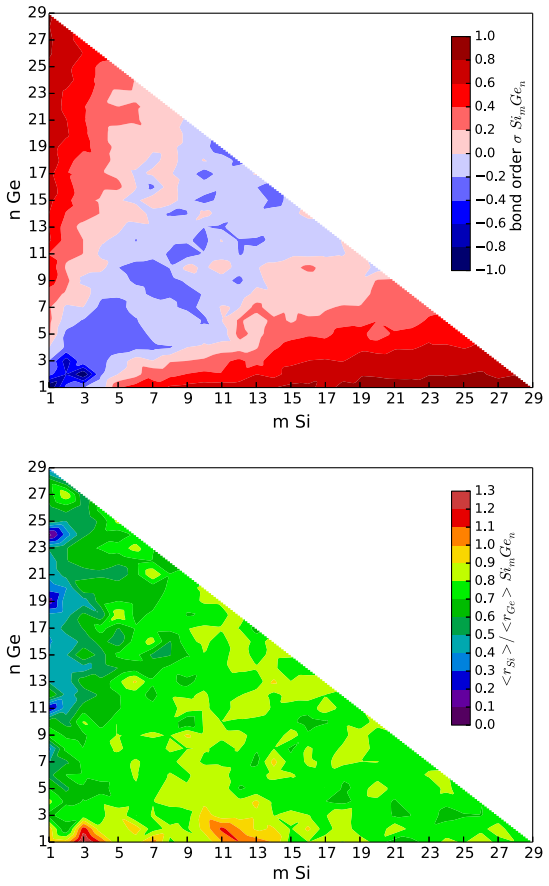

Fig. 18. The calculated bond order σ (top panel) and the ratio of the average radial distance of the Si atoms to that of Ge atoms (bottom panel) for mixed Si_mGe_n clusters as a function of (m, n).

cluster. At first we calculated the geometric center $\vec{R}_0$ of a cluster with N atoms from the position of all atoms $\vec{R}_i$

$$\vec{R}_0 = \frac{1}{N}\sum_{i=1}^{N}\vec{R}_i \tag{25}$$

and afterwards the radial distance r_i for the i-th atom to the geometric center $\vec{R}_0$ as

$$r_i = |\vec{R}_i - \vec{R}_0|. \tag{26}$$

The ratio $r(m, n)$ between the average radial distances of the silicon and germanium atoms calculated from

$$r_{m,n} = \frac{\langle r_{Si}\rangle}{\langle r_{Ge}\rangle} \tag{27}$$

now indicates the type of segregation. A ratio being smaller than 1 indicates a $Si_{core}Ge_{shell}$ cluster whereas values larger 1 would imply that a $Si_{shell}Ge_{core}$ structure has been formed. Values close to 1 on the other side suggest that mixing is beneficial or that a multishell structure is the preferred type of segregation in a given cluster. The ratio $r_{m,n}$ for all compositions is shown in Fig. 18. Likewise as predicted by the bond order σ, a segregation is visible with a clear preference for $Si_{core}Ge_{shell}$ for most of the compositions. However, we also noticed some compositions with ratios $r_{m,n}$ closer to 1, suggesting that also a mixing of both elements is realized in some of the studied compositions.

As for the pure clusters we studied the HL-gap and, in addition, the energies of the HOMO and LUMO of the mixed clusters in order to get some insight into the electronic properties of the clusters. Despite the fact that our structures differ from those reported by Rehman et al. [23] we qualitatively found the same behavior in our study. Thus, the energies of the HOMO and the LUMO of the 1:1 mixed clusters are in general closer to those of the pure germanium clusters than the pure silicon clusters of the same total size as can be seen in Fig. 19. Furthermore, we observe a reduction in the HL gap when increasing the cluster size of those mixed clusters plus an oscillatory behavior of the HOMO/LUMO and HL energies as function of cluster size, especially for the smaller clusters.

In Fig. 21 we show the HOMO-LUMO gaps for all compositions and sizes. The reduction of the HL gap with increasing cluster size as was found for the clusters with a fixed Si:Ge ratio can also be seen in the results for the other compositions and sizes. In addition, the calculated gaps are far from converged to the bulk values for the clusters of the present study, which may not surprise taking the facts into account that most of the atoms of the clusters are placed in the closest vicinity to the surfaces and that the structures do not resemble those of the bulk materials.

Rehman et al. [23] reported that the HOMO and LUMO energies are not a simple function of the size and composition alone and therefore we explored whether it was possible to identify possible correlations between those properties and other properties of the clusters by calculating the covariance and Pearson correlation coef-

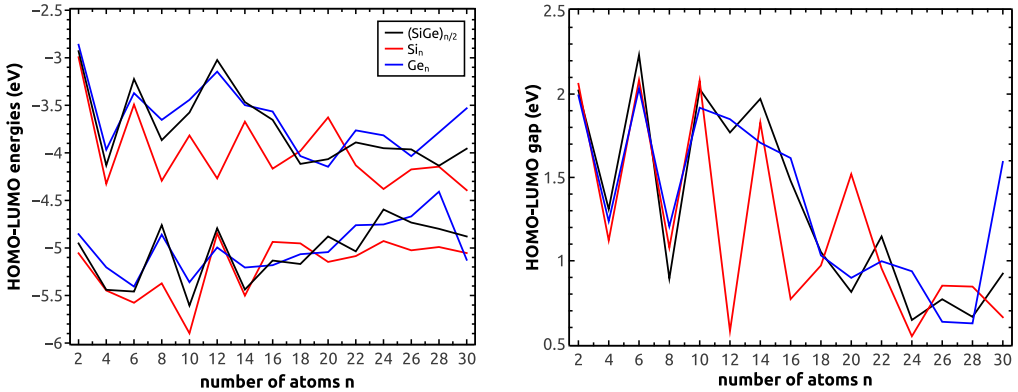

Fig. 19. The HOMO-LUMO energies (left plot) and the HOMO-LUMO gaps (right plot) of $(SiGe)_{n/2}$ clusters as a function of the size n.

Please cite this article in press as: S. Kohaut et al., Growth patterns, shapes, and electronic properties of mixed Si_mGe_n clusters with $n + m \leqslant 30$, Comput. Theoret. Chem. (2016), http://dx.doi.org/10.1016/j.comptc.2016.12.001

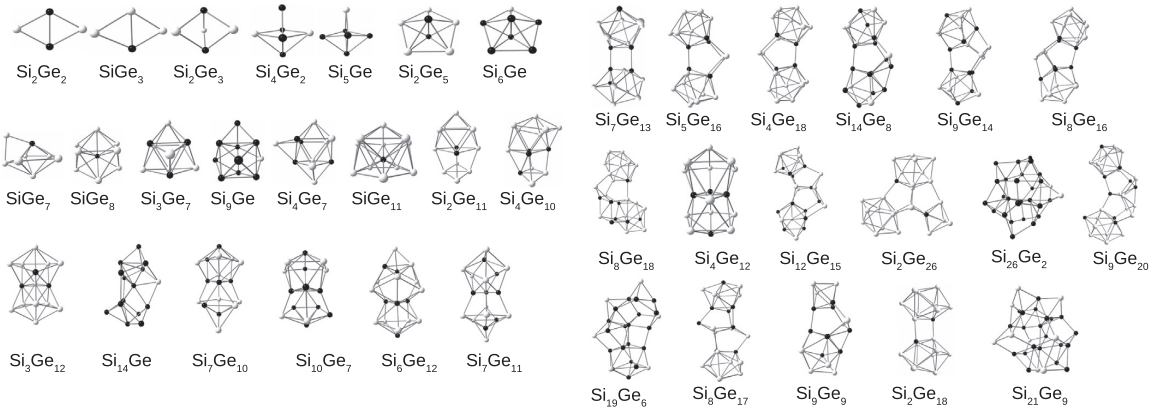

Fig. 20. The structures of the most stable compositions according to Eqs. (22) and (23) in mixed Si_mGe_n clusters. Si atoms are colored in white whereas Ge atoms are shown in black. (For interpretation of the references to color in this figure legend, the reader is referred to the web version of this article.)

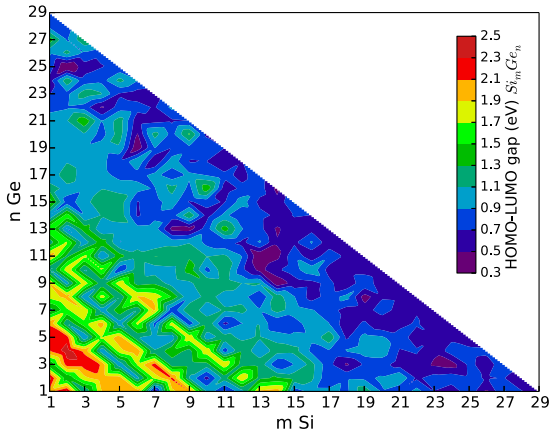

Fig. 21. The HOMO-LUMO gap of Si_mGe_n clusters as a function of (m, n).

ficients between the energies of the HOMO and LUMO and the resulting HL energy gap on the one side and various other properties that we have used to describe the shape and structures of the clusters. The covariance between two properties X and Y was calculated from

$$\mathrm{cov}(X,Y) = \frac{\sum_{i=1}^{n}(x_i - \bar{x})(y_i - \bar{y})}{n} \tag{28}$$

with x_i and y_i being the individual values for X and Y, and $\bar{x}, \bar{y}$ their averages. Afterwards the Pearson correlation coefficient r can be obtained from

$$r_{X,Y} = \frac{\mathrm{cov}(X,Y)}{\sigma_X \sigma_Y} \tag{29}$$

with σ being equal to the standard deviation of X and Y.

However, as can be seen in Table 5 it was not possible to identify any correlations between the electronic and the structural properties. Only a weak correlation between the energy of the HOMO as well as the HL-gap and the asphericity could be identified. We therefore conclude that the electronic properties are a result of several aspects and simple explanations based on a decomposition into size, shape, or composition effects in small to medium-sized SiGe clusters are not feasible.

4. Conclusions

We have used an evolutionary-based global-optimization procedure in combination with the parametrized DFTB method to determine the putative global minimum-energy structures of Si_mGe_n clusters for all stoichiometries up to $n + m \leqslant 30$. All obtained structures were re-optimized through DFT (PBE) calculations and the influence of the composition on the structures and shapes were discussed. In contrast to the bulk where full solubility for both elements is known, we showed that the stability correlates with the shape of the clusters with the most stable structures being found for prolate clusters with an average content of 32% silicon. In general, we also found that the larger clusters are neither similar to the corresponding pure clusters of silicon nor to the motifs found for germanium, especially for the mixed clusters with about equal amounts of silicon and germanium. However, silicon is the element that dominates the shape in clusters with larger Si contents. The trend towards the formation of a core-shell system is also visible if one analyses the average effective coordination numbers and variable shape descriptors in the mixed structures, especially in clusters with lower contents of foreign atoms. For clusters with about equal ratios of both elements we found a preference for disorderly mixed or onion-like structures. In contrast to the bulk where clear correlations between the composition of mixed SiGe

Table 5
The calculated Pearson correlation coefficients for the electronic properties and various shape and structure descriptors.

	X_{Ge} %	Asphericity b	ECN	d_{av}	ECN_{Si}	d_{av}^{Si}	ECN_{Ge}	d_{av}^{Ge}
HOMO	0.18	0.40	0.18	0.18	0.18	0.11	0.11	0.17
LUMO	0.32	−0.23	0.06	0.30	0.25	0.34	0.15	0.19
HL-gap	0.11	−0.37	−0.06	0.10	0.06	0.16	0.04	0.03

Please cite this article in press as: S. Kohaut et al., Growth patterns, shapes, and electronic properties of mixed Si_mGe_n clusters with $n + m \leqslant 30$, Comput. Theoret. Chem. (2016), http://dx.doi.org/10.1016/j.comptc.2016.12.001

and their electronic properties are known [3], we could not find any evidence that the electronic properties are determined by a single property alone in our studied mixed Si–Ge clusters.

Acknowledgements

Stephan Kohaut would like to thank N. Louis for computational support. Moreover, the authors acknowledge C^3MSaar for providing the computational resources for this study.

Appendix A. Supplementary material

Supplementary data associated with this article can be found, in the online version, at http://dx.doi.org/10.1016/j.comptc.2016.12.001.

References

[1] B.L. Oliva-Chatelain, T.M. Ticich, A.R. Barron, Doping silicon nanocrystals and quantum dots, Nanoscale 8 (2016) 1733–1745.
[2] Y. Sun, S.E. Thompson, T. Nishida, Physics of strain effects in semiconductors and metal-oxide-semiconductor field-effect transistors, J. Appl. Phys. 101 (10) (2007) 104503.
[3] M.V. Fischetti, S.E. Laux, Band structure, deformation potentials, and carrier mobility in strained Si, Ge, and SiGe alloys, J. Appl. Phys. 80 (4) (1996) 2234–2252.
[4] W. Hellmann, R.G. Hennig, S. Goedecker, C.J. Umrigar, B. Delley, T. Lenosky, Questioning the existence of a unique ground-state structure for Si clusters, Phys. Rev. B 75 (February) (2007) 085411.
[5] K. Raghavachari, C.M. Rohlfing, Bonding and stabilities of small silicon clusters: a theoretical study of Si_7-Si_{10}, J. Chem. Phys. 89 (4) (1998) 2219–2234.
[6] P. Ballone, W. Andreoni, R. Car, M. Parrinello, Equilibrium structures and finite temperature properties of silicon microclusters from ab-initio molecular-dynamics calculations, Phys. Rev. Lett. 60 (January) (1988) 271–274.
[7] X. Zhu, X.C. Zeng, Structures and stabilities of small silicon clusters: ab-initio molecular-orbital calculations of Si_7-Si_{11}, J. Chem. Phys. 118 (8) (2003) 3558–3570.
[8] Kai-Ming Ho, Alexandre A. Shvartsburg, Bicai Pan, Zhong-Yi Lu, Cai-Zhuang Wang, Jacob G. Wacker, James L. Fye, Martin F. Jarrold, Structures of medium-sized silicon clusters, Nature 392 (April) (1998) 582–585, http://dx.doi.org/10.1038/33369.
[9] A. Tekin, B. Hartke, Global geometry optimization of small silicon clusters with empirical potentials and at the DFT level, Phys. Chem. Chem. Phys. 6 (2004) 503–509.
[10] K.A. Jackson, M. Horoi, I. Chaudhuri, T. Frauenheim, A.A. Shvartsburg, Unraveling the shape transformation in silicon clusters, Phys. Rev. Lett. 93 (July) (2004) 013401.
[11] J.T. Lyon, P. Gruene, A. Fielicke, G. Meijer, E. Janssens, P. Claes, P. Lievens, Structures of silicon cluster cations in the gas phase, J. Am. Chem. Soc. 131 (3) (2009) 1115–1121, PMID: 19154175.
[12] S. Yoo, X.C. Zeng, Structures and stability of medium-sized silicon clusters. III. Reexamination of motif transition in growth pattern from Si_{15} to Si_{20}, J. Chem. Phys. 123 (16) (2005) 164303.
[13] S. Yoo, X.C. Zeng, Structures and relative stability of medium-sized silicon clusters. IV. Motif-based low-lying clusters Si_{21}-Si_{30}, J. Chem. Phys. 124 (5) (2006).
[14] J.M. Hunter, J.L. Fye, M.F. Jarrold, J.E. Bower, Structural transitions in size-selected germanium cluster ions, Phys. Rev. Lett. 73 (October) (1994) 2063–2066.
[15] S. Yoo, X.C. Zeng, Search for global-minimum geometries of medium-sized germanium clusters. II. Motif-based low-lying clusters Ge_{21}-Ge_{29}, J. Chem. Phys. 124 (18) (2006) 184309.
[16] L.-Z. Zhao, W.-C. Lu, W. Qin, Q.-J. Zang, C.Z. Wang, K.M. Ho, Fragmentation behavior of Ge_n clusters ($2 \leqslant n \leqslant 33$), Chem. Phys. Lett. 455 (46) (2008) 225–231.
[17] S. Bulusu, S. Yoo, X.C. Zeng, Search for global minimum geometries for medium sized germanium clusters: Ge_{12}-Ge_{20}, J. Chem. Phys. 122 (16) (2005).
[18] W. Qin, W.-C. Lu, L.-Z. Zhao, Q.-J. Zang, G.-J. Chen, C.Z. Wang, K.M. Ho, Platelike structures of semiconductor clusters Ge_n(n = 40 - 44), J. Chem. Phys. 131 (12) (2009) 124507.
[19] H. Li, W. Chen, X. Han, L. Li, Q. Sun, Z. Guo, Y. Jia, Van der Waals effects on semiconductor clusters, J. Comput. Chem. 36 (25) (2015) 1919–1927.
[20] A.A. Shvartsburg, B. Liu, Z.-Y. Lu, C.-Z. Wang, M.F. Jarrold, K.-M. Ho, Structures of germanium clusters: where the growth patterns of silicon and germanium clusters diverge, Phys. Rev. Lett. 83 (September) (1999) 2167–2170.
[21] Y.-S. Wang, S.D. Chao, Structures and energetics of neutral and ionic silicon-germanium clusters: density functional theory and coupled cluster studies, J. Phys. Chem. A 115 (9) (2011) 1472–1485, PMID: 21322541.
[22] S.-D. Li, Z.-G. Zhao, X.-F. Zhao, H.-S. Wu, Z.-H. Jin, Structural and electronic properties of semiconductor binary microclusters A_mB_n ($a, b = \mathrm{Si, Ge, C}$) : a B3LYP-DFT study, Phys. Rev. B 64 (October) (2001) 195312.
[23] H. ur Rehman, M. Springborg, Y. Dong, Structural and electronic properties of Si_n, Ge_n, and Si_nGe_n clusters, J. Phys. Chem. A 115 (10) (2011) 2005–2015, PMID: 21338159.
[24] Y. Dong, M. Springborg, Y. Pang, F.M. Morillon, Analysing the properties of clusters: structural similarity and heat capacity, Comput. Theoret. Chem. 1021 (2013) 16–25.
[25] D.M. Deaven, K.M. Ho, Molecular geometry optimization with a genetic algorithm, Phys. Rev. Lett. 75 (July) (1995) 288–291.
[26] P. Koskinen, V. Mäkinen, Density-functional tight-binding for beginners, Comput. Mater. Sci. 47 (1) (2009) 237–253.
[27] S.R. Bahn, K.W. Jacobsen, An object-oriented scripting interface to a legacy electronic structure code, Comput. Sci. Eng. 4 (May-June) (2002) 56–66.
[28] M.S.e.O. Madelung, U. Rössler, Silicon (Si) lattice parameters. Landolt-Börnstein - Group III Condensed Matter 41A1a (Group IV Elements, IV-IV and III-V Compounds. Part a - Lattice Properties).
[29] M.S.e.O. Madelung, U. Rössler, Germanium (Ge), lattice parameter, thermal expansion. Landolt-Börnstein - Group III Condensed Matter 41A1b (Group IV Elements, IV-IV and III-V Compounds. Part b - Electronic, Transport, Optical and Other Properties).
[30] R. Gehrke, K. Reuter, Assessing the efficiency of first-principles basin-hopping sampling, Phys. Rev. B 79 (2009) 085412.
[31] M.D. Wolf, U. Landman, Genetic algorithms for structural cluster optimization, J. Phys. Chem. A 102 (1998) 6129–6137.
[32] D. Porezag, T. Frauenheim, T. Köhler, G. Seifert, R. Kaschner, Construction of tight-binding-like potentials on the basis of density-functional theory: application to carbon, Phys. Rev. B 51 (May) (1995) 12947–12957.
[33] G. Seifert, D. Porezag, T. Frauenheim, Calculations of molecules, clusters, and solids with a simplified LCAO-DFT-LDA scheme, Int. J. Quant. Chem. 58 (1996) 185–192.
[34] J.M. Soler, E. Artacho, J.D. Gale, A. García, J. Junquera, P. Ordejón, D. Snchez-Portal, The SIESTA method for ab-initio order-N materials simulation, J. Phys.: Conden. Matter 14 (11) (2002) 2745.
[35] K. Huber, G. Herzberg, Molecular Spectra and Molecular Structure. IV. Constants of Diatomic Molecules, Van Nostrand Reinhold Co., 1979.
[36] E.F. Archibong, A. St-Amant, A study of Ge_n^- and Ge_n ($n = 2 - 6$) using B3LYP-dft and CCSD(T) methods: the structures and electron affinities of small germanium clusters, J. Chem. Phys. 109 (3) (1998) 962–972.
[37] J. Heyd, G.E. Scuseria, Efficient hybrid density functional calculations in solids: assessment of the Heyd-Scuseria-Ernzerhof screened coulomb hybrid functional, J. Chem. Phys. 121 (3) (2004) 1187–1192.
[38] G.I. Csonka, J.P. Perdew, A. Ruzsinszky, P.H.T. Philipsen, S. Lebègue, J. Paier, O.A. Vydrov, J.G. Ángyán, Assessing the performance of recent density functionals for bulk solids, Phys. Rev. B 79 (April) (2009) 155107.
[39] T. Ozaki, H. Kino, Numerical atomic basis orbitals from H to Kr, Phys. Rev. B 69 (May) (2004) 195113.
[40] Ding Li Ping, Zhang Fang Hui, Zhu Yong Sheng, Lu Cheng, Kuang Xiao Yu, Lv Jian, Shao Peng, Understanding the structural transformation, stability of medium-sized neutral and charged silicon clusters, Sci. Rep. 5 (November) (2015) 15951.
[41] D.A. Hostutler, H. Li, D.J. Clouthier, G. Wannous, Exploring the bermuda triangle of homonuclear diatomic spectroscopy: the electronic spectrum and structure of Ge_2, J. Chem. Phys. 116 (10) (2002) 4135–4141.
[42] K.A. Peterson, T.H. Dunning, Accurate correlation consistent basis sets for molecular core-valence correlation effects: the second row atoms Al-Ar, and the first row atoms B-Ne revisited, J. Chem. Phys. 117 (23) (2002) 10548–10560.
[43] B. Farid, R.W. Godby, Cohesive energies of crystals, Phys. Rev. B 43 (June) (1991) 14248–14250.
[44] J. Wang, G. Wang, J. Zhao, Structure and electronic properties of Ge_n (n=2–25) clusters from density-functional theory, Phys. Rev. B 64 (October) (2001) 205411.
[45] C. Pouchan, D. Bégué, D.Y. Zhang, Between geometry, stability, and polarizability: density functional theory studies of silicon clusters Si_n ($n = 3 - 10$), J. Chem. Phys. 121 (10) (2004) 4628–4634.
[46] D.A. Götz, S. Heiles, R.L. Johnston, R. Schäfer, Note: Gas phase structures of bare Si_8 and Si_{11} clusters from molecular beam electric deflection experiments, J. Chem. Phys. 136 (18) (2012) 186101.
[47] W. Qin, W.-C. Lu, L.-Z. Zhao, Q.-J. Zang, C.Z. Wang, K.M. Ho, Stabilities and fragmentation energies of Si_n clusters ($n = 2 - 33$), J. Phys.: Condens. Matter 21 (45) (2009) 455501.
[48] L.R. Marim, M.R. Lemes, A. Dal Pino, Investigation of prolate and near spherical geometries of mid-sized silicon clusters, Physica Status Solidi (b) 243 (2) (2006) 449–458.
[49] S. Yoo, Possible lowest-energy geometry of silicon clusters Si_{21} and Si_{25}, J. Am. Chem. Soc. 125 (44) (2003) 13318–13319, PMID: 14583002.
[50] B. Liu, Z.-Y. Lu, B. Pan, C.-Z. Wang, K.-M. Ho, A.A. Shvartsburg, M.F. Jarrold, Ionization of medium-sized silicon clusters and the geometries of the cations, J. Chem. Phys. 109 (1998) 9401–9409.
[51] S. Ma, G. Wang, Structures of medium size germanium clusters, J. Mol. Struct.: {THEOCHEM} 767 (13) (2006) 75–79.
[52] H. Arkin, W. Janke, Gyration tensor based analysis of the shapes of polymer chains in an attractive spherical cage, J. Chem. Phys. 138 (5) (2013) 054904.

Please cite this article in press as: S. Kohaut et al., Growth patterns, shapes, and electronic properties of mixed Si_mGe_n clusters with $n + m \leqslant 30$, Comput. Theoret. Chem. (2016), http://dx.doi.org/10.1016/j.comptc.2016.12.001

[53] D.N. Theodorou, U.W. Suter, Shape of unperturbed linear polymers: polypropylene, Macromolecules 18 (6) (1985) 1206–1214.
[54] R. Hoppe, Effective coordination numbers (ECoN) and mean fictive ionic radii (MEFIR), Z. Kristallogr. 150 (1979) 224410.
[55] J.P. Chou, C.R. Hsing, C.M. Wei, C. Cheng, C.M. Chang, Ab initio random structure search for 13-atom clusters of fcc elements, J. Phys. Condens. Matter 25 (2013) 125305.
[56] J. Tarus, M. Tantarimäki, K. Nordlund, Segregation in SiGe clusters, Nucl. Instrum. Methods Phys. Res. Sect. B: Beam Interact. Mater. Atoms 228 (14) (2005) 51–56 (Proceedings of the Seventh International Conference on Computer Simulation of Radiation Effects in Solids).
[57] A. Harjunmaa, K. Nordlund, Molecular dynamics simulations of Si/Ge cluster condensation, Comput. Mater. Sci. 47 (2) (2009) 456–459.
[58] A. Harjunmaa, K. Nordlund, A. Stukowski, Structure of Si/Ge nanoclusters: kinetics and thermodynamics, Comput. Mater. Sci. 50 (4) (2001) 1504–1508 (Proceedings of the 19th International Workshop on Computational Mechanics of Materials IWCMM 19).
[59] M. Molayem, V.G. Grigoryan, M. Springborg, Global minimum structures and magic clusters of Cu_mAg_n nanoalloys, J. Phys. Chem. C 115 (45) (2011) 22148–22162.

Please cite this article in press as: S. Kohaut et al., Growth patterns, shapes, and electronic properties of mixed Si_mGe_n clusters with $n + m \leqslant 30$, Comput. Theoret. Chem. (2016), http://dx.doi.org/10.1016/j.comptc.2016.12.001

J Clust Sci (2016) 27:913–933
DOI 10.1007/s10876-016-1003-1

ORIGINAL PAPER

Structural, Energetic, and Magnetic Properties of $Ag_{n-m}Rh_m$ and Ag_mRh_{n-m} Clusters with $n \leq 20$ and $m = 0, 1$

Stephan Kohaut[1] · Michael Springborg[1,2]

Received: 12 November 2015 / Published online: 22 March 2016
© Springer Science+Business Media New York 2016

Abstract At first, a genetic algorithm in combination with either the parametrized density-functional tight-binding method or a Gupta-potential is used to determine the putative global minimum energy structures of mixed $Ag_{n-m}Rh_m$ and Ag_mRh_{n-m} clusters with $n \leq 20$ and $m = 0, 1$. Subsequently, the resulting structures are re-optimized with a first-principles method. The results demonstrate that the exchange of a single silver atom by rhodium leads to compact core-shell-like structures with structural motifs well known from the Lennard-Jones system. For the systems of the present study, $AgRh_{n-1}$ clusters retain their cube-based structural motif and the silver atoms typically avoid the corner positions within a cube if possible. Population analysis of both cluster systems shows that the total magnetic moment is mainly due to unpaired electrons on the rhodium atoms with a small ferro-magnetic contribution of the silver host in $Ag_{n-1}Rh$ and virtually no contribution to the total magnetic moment from the single silver atom in $AgRh_{n-1}$ clusters.

Keywords AgRh clusters · Structure · Energetics · Magnetism

Introduction

Silver and Rhodium are traditionally known to be two immiscible metals in the bulk. Already at the beginning of the twentieth century Rossler reported an extremely small solubility of rhodium in silver and a larger solubility of silver in

✉ Michael Springborg
m.springborg@mx.uni-saarland.de

Stephan Kohaut
s.kohaut@mx.uni-saarland.de

[1] Physical and Theoretical Chemistry, University of Saarland, 66123 Saarbrücken, Germany

[2] School of Materials Science and Engineering, Tianjin University, Tianjin 300072, China

rhodium [1]. The vanishingly small solubility of rhodium in liquid silver was later confirmed by X-ray diffraction studies of Drier and Walker who also showed the absence of any intermediate phases between these two elements [2]. Rudnitskii and Khitinskaya measured mechanic and thermoelectric properties and excluded on the basis of these results a greater solubility of rhodium in silver up to 800 °C [3]. On the rhodium-rich side of the phase diagram a greater miscibility of 4.7 at% was measured that increased with temperature to 19 at% at 1200 °CC [3]. Miedema et al. explained the immiscibility within their semi-empirical theory as being due to a large mismatch of the electron density at the border of the Wigner–Seitz cells of the two atoms [4]. The elimination of such discontinuities of the electron density at the interface between the different atoms requires energy that ultimately leads to a positive mixing enthalpy with a maximum at a composition of about 50:50 and a positive heat of formation for all silver–rhodium alloys [5]. Additionally, there is a small lattice mismatch as a result of the difference in atomic radii [6], that, however, is below the well known Hume–Rothery rule of 15 % difference in the lattice constants which would make it already unfavourable for both elements to form alloys because of a simple size effect (like, e.g., in the Au–Ni system) [7]. Nevertheless, efforts have been undertaken to synthesize such alloys by co-reduction in solution [8] or through microwave-based methods [9] because of their predicted promising catalytic properties for instance in hydrogenation reactions and hydrogen storage applications [10, 11].

The difference in the electronic structure between silver and rhodium expresses itself also in different growth paths and structural motifs preferred in sizes below the bulk domain. Experimental measurements on neutral and charged silver clusters showed an icosahedral growth pattern [12–14] albeit there is evidence that such icosahedra are only metastable and subsequently relax to close-packed fcc structures [15]. The structures and growth paths of rhodium clusters are quite controversial. Thus, whereas density functional methods on a lower level on Jacob's ladder of density functional theory predict cubic motifs as building units [16–20], the global minimum energy structures predicted by hybrid density functional theory are more compact [21, 22] and in better agreement with structures proposed from experimental results [23, 24]. However, inclusion of a portion of exact exchange increases the magnetic moment of each cluster which then becomes larger than the experimental values, a result that was also obtained through pure Hartree–Fock calculations [25, 26].

Most of the published work on doped bimetallic silver clusters deal with dopants of the first row of the transition-metal series, e.g. the systems Ag–Ni, Ag–Cu, Ag–Co [27, 28], Ag–Fe [29, 30], Ag–Mn [31] or from the third row like Ag–Au [32] and the effect of mixing silver with an element from the second row was hardly ever considered except for the mixable Ag–Pd system [33, 34]. It can be expected that the effect of alloying of silver with a 4*d* transition metal will lead to different bonding mechanisms within the clusters because of an enhanced covalency in the involved bonds due to the fact that the 4*d* orbitals are less diffuse than their 3*d* counterparts. It was also shown in weakly mixable systems like Ag–Cu or Ag–Ni [35, 36] that clusters well below the bulk regime can show enhanced mixability because of an interplay between the specific surface energy and the bulk cohesive

energy of the elements involved, making it worthwhile to study the effect of doping of silver clusters with rhodium atoms and vice-versa. Therefore, in this paper we present results of a global optimization search for mixed $Ag_{n-1}Rh$ and $AgRh_{n-1}$ clusters and compare their properties with pure Ag_n and Rh_n clusters. We have used a density functional tight-binding approach (DFTB) to sample the potential energy surface of this systems because quantum mechanic effects seems to be crucial to describe the smaller clusters, in particular for possible cube-based structures with a larger rhodium content. Additionally, we compare the results of our DFTB structure optimizations with results from a RGL-potential [37, 38] function. Subsequently, we re-optimize all located putative global minimum-energy structures within the density functional theory as implemented in the Siesta code [39]. In particular, we discuss the effects on the magnetism arising from a single dopant of rhodium or silver in small, pure silver and rhodium clusters.

Computational Methods

For the unbiased structure optimization we apply an evolutionary algorithm based on a cut-and-splice procedure [40, 41] that is combined with the DFTB method [42] for the determination of the total energy for a given structure as implemented in the Hotbit code [43]. We use a self-written code in combination with the ASE [44] collection of python scripts.

An initial population of structures was created from more sets of randomly placed rhodium and silver atoms inside a cubic box that subsequently were relaxed to their nearest local total-energy minima. Each cluster is ascribed a simple fitness value based on its DFTB total-energy after having been relaxed structurally. In each generation the two fittest clusters are allowed to form offspring clusters with every other population member by cutting two parent clusters along a randomly defined plane and reassembling them randomly and simultaneously assuring that the correct stoichiometry is kept (the so called crossover process). Additionally, we apply mutation operators to all of the current population members and move all the structures (the current population members, the offsprings and the mutants) into a large pool on which a selection process based on a tournament was run to build the next generation. Several mutation operators have been used in the literature [45] that all should help in maintaining the genetic diversity in a population of a given size and prohibit premature convergence to a non-optimal structure. In the present study, the following operators were used:

- Random displacements of all atoms with a Gaussian-distributed step-size [46]
- Permutation of two atomic species to explicitly include homotops of the same structural motif in the search process
- A twinning mutation in which two halves of a cluster are rotated by a small random angle in opposite directions [47]
- An etch-add process in which a randomly picked atom is removed and placed next to another atom [47].

As there is no strict stop criterion defined or known in evolutionary algorithms of this kind, the algorithm was simply stopped after it has not led to clusters with a lower energy during 150 generations. All simulations used a population size of ten members and the fittest cluster in each generation is passed to the next generation immediately (=elitism). After the global minimization, the obtained clusters that are lowest in energy were subjected to a DFT re-optimization.

DFTB Paramatrization

For details and a rigorous mathematical treatment of the DFTB method we refer to several published review articles, whereas here we want to focus merely on details of our parametrization [42, 48]. The total energy relative to that of non-interacting neutral atoms can be approximated as a sum of the eigenvalues of all occupied orbitals minus that of the neutral, non-interacting atoms, E_{BS}, plus a term that arises from Coulomb interactions E_{Coul} and a pairwise repulsive potential U_{rep}.

$$E = E_{\text{BS}} + E_{\text{Coul}} + U_{\text{rep}} \tag{1}$$

At the lowest level of approximation (corresponding to the non-SCC DFTB) we neglect interactions that result from charge fluctuations and express the total energy as the sum of E_{BS} and U_{rep}. U_{rep} can be parametrized and adjusted to reproduce either experimental or ab-initio results.

Using an LCAO approach with atomic orbitals ϕ_v expanded in terms of a minimal set of atomic-centered non-orthogonal basis functions,

$$\psi_i(\mathbf{r}) = \sum_v c_{vi}\phi_v(\mathbf{r}), \tag{2}$$

one has to solve the Kohn–Sham eigenvalue equation for an effective potential V_{eff} to determine E_{BS} as the sum over the eigenvalues of all occupied orbitals,

$$\hat{H}\psi_i(r) = \epsilon_i\psi_i(r), \tag{3}$$

with

$$\hat{H} = \hat{T} + V_{\text{eff}}. \tag{4}$$

Here, $\hat{T}$ is the kinetic-energy operator.

Substitution of (2) into (3) gives the eigenvalue equation

$$\sum_v c_{vi}(H_{vi} - \epsilon_i S_{vi}) = 0 \tag{5}$$

with

$$H_{vi} = \langle\phi_v|\hat{H}|\phi_i\rangle \tag{6}$$

and

$$S_{vi} = \langle\phi_v|\phi_i\rangle. \tag{7}$$

The elements of H_{vi} and S_{vi} are determined from calculations on diatomic molecules by using the Slater–Koster rules and stored in a table. Thereby it is assumed that the effective potential can be written as a superposition of atomic potentials

$$V_{\text{eff}}(\mathbf{r}) = \sum_n V_n(|\mathbf{r} - \mathbf{R}_n|) \tag{8}$$

with $\mathbf{R}_n$ being the position of the nth atom. Moreover, $V_n(r)$ is the potential of the free, isolated, nth atom, $V_n^{(0)}(r)$, augmented by a short-ranged confining potential that gives a contraction of the orbitals when passing from the isolated atom to a compound,

$$V_n(r) = V_n^{(0)}(r) + \left(\frac{r}{r_0}\right)^2. \tag{9}$$

For r_0 we use for Rh 4.56 bohr and for Ag 5.21 bohr.

Subsequently, we assume that

$$\langle \phi_v|\hat{T} + V_{\text{eff}}|\phi_i\rangle = \begin{cases} \langle \phi_v|\hat{T} + V_n|\phi_i\rangle & \text{for } \phi_v,\ \phi_i \text{ both on atom } n \\ \langle \phi_v|\hat{T} + V_n + V_m|\phi_i\rangle & \text{for } \phi_v,\ \phi_i \text{ on atoms } n \neq m \\ 0 & \text{otherwise.} \end{cases} \tag{10}$$

U_{rep} is determined by fitting to accurate results from ab-initio DFT (PBE) calculations. Specifically, in the present work we optimized a couple of appropriate structures (i.e., bulk and small symmetric clusters) with DFT and minimized the force differences $|F^{\text{DFT}} - F^{\text{DFTB}}|$ with a smoothing spline as explained by Koskinen and Mäkinen [43]. The thereby obtained derivative, U'_{rep}, was integrated to give the repulsion potential and tested against results from DFT calculations.

To increase the pool of candidates for possible global minimum energy structures, we additionally made global optimization runs using the well established RGL-potential [49] for the description of the Ag–Rh potential energy surface. With the RGL potential, also known as Gupta many-body potential, the energy of a system of atoms can be expressed as the sum of a repulsive pair potential E_r and an attractive many-body potential E_m. E_m can be calculated for an atom i interacting with atom j in the lattice $\alpha\beta$ from

$$E_m^i = -\left[\sum_j \xi_{\alpha\beta}^2 e^{-2q_{\alpha\beta}(r_{ij}/r_0^{\alpha\beta}-1)}\right]^{1/2} \tag{11}$$

with r_{ij} being the distance between atoms i and j, $r_0^{\alpha\beta}$ being the first-neighbours distance in lattice $\alpha\beta$, ξ an effective hopping integral, while q describes its dependency on the inter-atomic distance.

The repulsive potential is described by a Born–Mayer type ion-ion repulsive potential,

$$E_r^i = \sum_j A_{\alpha\beta} e^{-p_{\alpha\beta}(r_{ij}/r_0^{\alpha\beta}-1)} \tag{12}$$

with p being related to the compressibility of the metal and A representing a repulsion.

The total cohesive energy can then be calculated from

$$E_{\text{coh}} = \sum_i (E_m^i + E_r^i) \tag{13}$$

The parameters A, p, q, r_0, and ξ are most often obtained through fitting in order to reproduce experimental results (if available) like mechanical, structural and energetic properties. The parameters for the pairwise Rh–Rh and Ag–Ag interactions were taken unmodified from Cleri and Rosatto [50]. The hetero-atomic interactions were obtained by minimizing the sum of the relative errors between DFT and Gupta results for the lattices parameters, elastic constants, the bulk modulus, the cohesive energy, and the change in enthalpy for the reaction from the corresponding bulk structures in Ag_2Rh, AgRh, $AgRh_2$, $AgRh_3$, and Ag_3Rh. DFT results for the lattice constants and mechanic properties were calculated from spin polarized PBEsol calculations using the methods described elsewhere [50], while cohesive energies and changes in enthalpy were obtained from spin polarized PBE calculations.

Table 1 summarizes the results after the fitting process together with the relative deviations to the results of the DFT calculations (in brackets) whereas Table 2 gives the values of the Gupta parameters that were determined and subsequently used in this study.

All subsequent ab-initio DFT calculations for the clusters were performed using the PBE functional for exchange and correlation as implemented in the Siesta program. The scalar-relativistic pseudopotentials for silver and rhodium were created within the norm-conserving Troullier−Martins scheme for Ag($5s^{1.5}5p^04d^{9.5}4f^0$) and Rh($5s^15p^04d^84f^0$) valence configurations with cut-off values of 2.28, 2.59, 2.28, and

Table 1 Calculated properties of various crystals together with their relative errors in % using the modified RGL potential

Property	Ag_2Rh(C1)	AgRh(B2)	$AgRh_2$(C1)	$AgRh_3$($L1_2$)	Ag_3Rh ($L1_2$)
a [Å]	6.196 (+1.9)	3.144 (+0.7)	6.107 (+3.2)	3.867 (+0.6)	4.003 (+0.5)
B [GPa]	111.78 (−6.1)	179.74 (+0.9)	126.61 (−13.1)	224.47 (−4.5)	145.46 (−1.9)
C_{11} [GPa]	111.47 (+27.3)	177.63 (+0.4)	105.73 (−4.1)	296.63 (−10.3)	185.48 (+7.9)
C_{12} [GPa]	111.94 (−16.9)	180.79 (+1.2)	137.04 (−16.2)	188.39 (+0.6))	125.50 (−8.0)
C_{44} [GPa]	76.60 (−0.5)	130.79 (+0.9)	103.96 (−10.2)	142.62 (+13.3)	74.89 (0.4)
E_{coh} [eV/atom]	−3.127 (+7.8)	−3.904 (+6.8)	−3.771 (+4.6)	−4.764 (+3.1)	−3.360 (8.9)
ΔE_r [eV/atom]	0.7625 (+11.7)	0.4511 (−1.9)	1.050 (0.6)	0.289 (−1.1)	0.297 (28.1)

Table 2 RGL parameters used in this study for the description of the Ag−Rh interaction

	p	q	A (eV)	ξ (eV)	r_0 (Å)
Ag−Rh	13.666	2.9744	1.3615	0.10056	2.7604

Table 3 Details of the DZP basis set used in this study. All values are in bohr

	r_c	r_m
Ag_{5s}	7.00	5.85
Ag_{5p}	5.60	–
Ag_{4d}	7.00	3.36
Rh_{5s}	7.00	4.16
Rh_{5p}	4.71	–
Rh_{4d}	7.00	3.53

2.59 bohr for silver and 2.00, 2.08, and 2.44 bohr for rhodium, respectively. Moreover, we included non-linear core corrections with small pseudo-core radii of 1.1 bohr for both elements. A basis set of DZP quality together with a soft-confinement potential was used within a split-valence scheme in which the first basis function was fixed to a cut-off of 7.0 bohr and the split-norm r_m of the second basis function was optimized variationally for the bulk structures and for dimers of silver and rhodium. Afterwards, we added one *p*-type polarization function in either basis set and fine-tuned their cut-off values for larger clusters of rhodium and silver (the results are shown in Table 3). The re-optimization of the DFTB and Gupta results were done using this optimized DZP basis set and collinear spin-polarization in a large cubic box of 20.0 Å, using one **k** point at the Γ point for molecular systems and a **k** grid cutoff of 15 Å for all bulk calculations, respectively. A small Fermi-type smearing of 0.01 eV was applied in all DFT calculations to improve the convergence behaviour and a mesh-cutoff of 450 Ry was used for the real space grid. Atomic positions in all calculations were optimized to a residual force smaller than 0.01 eV/Å with the conjugate-gradient algorithm as implemented in Siesta.

Results

We start our discussion by comparing our putative global minimum energy structures for pure Ag and Rh clusters with results reported in the literature in order to estimate the accuracy of our combined DFTB/Gupta DFT approach. Although still based on an approximation, we expect the DFTB method to perform better for pure clusters, especially for small systems, were other semi-empirical potentials (eg. potentials that are based on a second-moment approximation to the local density of states like the Gupta potential) tend to maximize the number of contacts between the atoms leading in general to compact structures that often show similarities with simpler Lennard–Jones systems [51, 52].

Our optimized structures for the Rh clusters found by using DFTB and re-optimized with DFT, see Fig. 1, are in good agreement with what has been reported by several other authors already mentioned in the introduction. In addition, the calculated magnetic moments and other structural properties, shown in table 4, are consistent with other reported results [16–20, 52]. To give an impression of the performance for even larger clusters we add that we observed the cube-based structural motif at least up to the size of 30 atoms within our DFTB-based search,

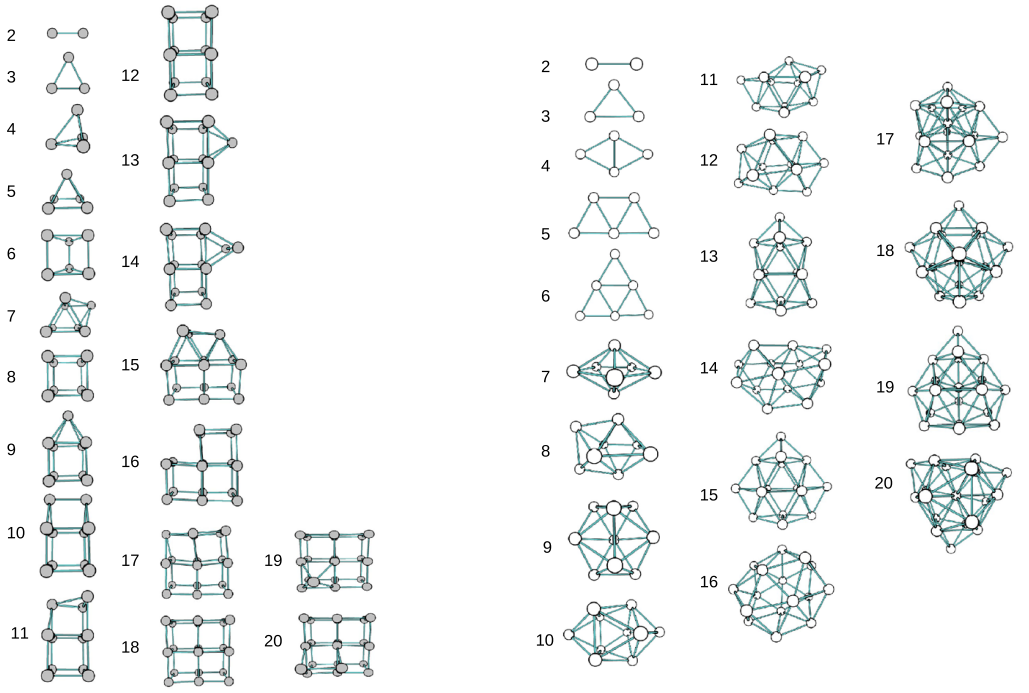

Fig. 1 The ground state structures of Rh_n (left) and Ag_n (*right*) obtained in this study (the *white spheres* represent the silver atoms while the *grey ones* correspond to rhodium

Table 4 Point groups, PG, effective coordination numbers, ECN, average bond lengths, d_{av}, total magnetic moments, m_t, and binding energies E_b (without BSSE correction) of Rh_n clusters calculated with PBE and a DZP basis set

Rh_n	PG	ECN	d_{av} (Å)	m_t (μ_B)	E_b (eV/atom)
2	$C_{\infty h}$	1.00	2.24	4.0	1.49
3	C_{2v}	1.97	2.47	5.0	2.11
4	C_{2v}	2.72	2.53	4.0	2.55
5	C_{4v}	3.17	2.51	5.0	2.84
6	D_{3h}	2.99	2.48	6.0	3.00
7	C_{2v}	3.69	2.53	9.0	3.15
8	O_h	3.01	2.43	12.0	3.38
9	C_s	3.52	2.49	13.0	3.40
10	C_{2v}	3.37	2.46	12.0	3.48
11	C_s	3.44	2.47	11.0	3.52
12	D_{4h}	3.34	2.43	8.0	3.68
13	C_s	3.66	2.47	9.0	3.68
14	C_s	3.56	2.45	8.0	3.73
15	C_s	4.06	2.50	9.0	3.75
16	C_{2v}	3.52	2.45	10.0	3.81
17	C_{2v}	3.76	2.47	7.0	3.84
18	D_{4h}	3.67	2.45	4.0	3.92
19	C_s	3.87	2.48	5.0	3.91
20	C_1	3.79	2.46	6.0	3.85

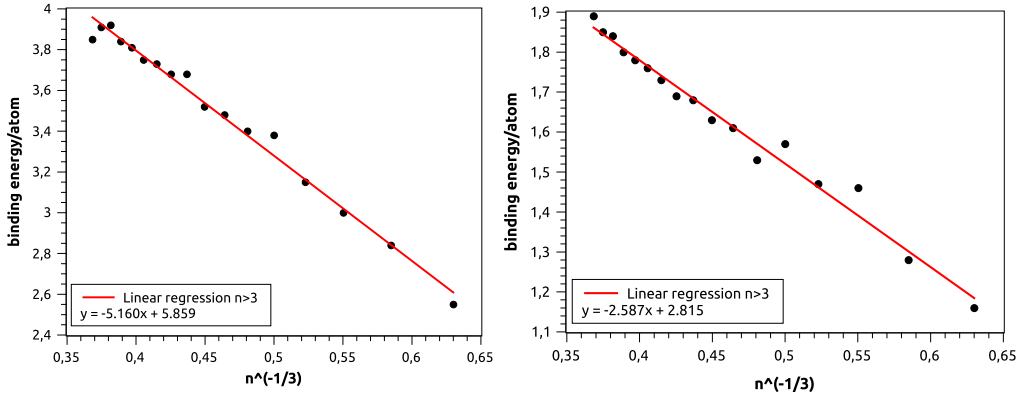

Fig. 2 Estimation of the bulk cohesive energy for rhodium (*left*) and silver (*right*) from the calculated binding energies of the clusters

while Bae et al. [17] reported a transition to more compact structure for sizes greater than 27 atoms.

From a graphical representation of the binding energy per atom as a function of $n^{-1/3}$, cf. Fig. 2, we can estimate the bulk cohesive energy for rhodium to be 5.85 $\pm$ 0.07 eV/atom which is very close to the cohesive energy, 5.75 eV/atom, reported for bulk rhodium [53].

To calculate the effective coordination number (ECN) and average bond lengths (d_{av}) we use an approach described in [54] and tested for example by Chou et al. for clusters [20]. According to this, the average bond length for atom i is defined as

$$d^i_{\mathrm{av}} = \frac{\sum_{j=1}^{N} d_{ij} e^{[1-(d_{ij}/d^i_{\mathrm{av}})^6]}}{\sum_{j=1}^{N} e^{[1-(d_{ij}/d^i_{\mathrm{av}})^6]}} \tag{14}$$

with N being the total number of atoms in the studied cluster. It is seen that d_{av} has to be determined iteratively. Thereby, d^i_{av} is initially taken as the shortest bond length for atom i and the final value obtained self consistently using a convergence criterion of 10^{-4} Å. Finally, the effective coordination number ECN of atom i is given by

$$\mathrm{ECN}(i) = \sum_{j=1}^{N} e^{[1-(d_{ij}/d^i_{\mathrm{av}})^6]}. \tag{15}$$

Averages of ECN and d_{av} for a given cluster can then be obtained by summing up each property for each atom and divide this number by the number of atoms of the cluster.

While our results (see Fig. 1 for the obtained structures and for a summary of all other calculated properties Table 5) for the structures of smaller silver clusters with up to seven atoms agree with studies of Gamboa et al., [55] Fournier, [56] and Jin et al., [57] we find differences for the larger clusters, especially when comparing with the structures of the most recent study. For Ag_8 we identified the C_s structure with our

Table 5 Point groups, PG, effective coordination numbers, ECN, average bond lengths, d_{av}, total magnetic moments, m_t, and binding energies E_b (without BSSE correction) of Ag_n clusters calculated with PBE and a DZP basis set

Ag_n	PG	ECN	d_{av} (Å)	m_t (μ_B)	E_b (eV/atom)
2	$C_{\infty h}$	1.00	2.62	0.0	0.87
3	D_{3h}	2.00	2.68	1.0	0.84
4	D_{2h}	2.47	2.77	0.0	1.16
5	C_{2v}	2.79	2.77	1.0	1.28
6	D_{3h}	2.98	2.76	0.0	1.46
7	D_{5h}	4.54	2.85	1.0	1.47
8	C_{2v}	4.47	2.84	0.0	1.57
9	C_{2v}	5.02	2.87	1.0	1.53
10	D_{4d}	4.77	2.86	0.0	1.61
11	C_s	4.85	2.86	1.0	1.63
12	C_s	5.10	2.86	0.0	1.68
13	C_{2v}	5.05	2.86	1.0	1.69
14	C_2	5.18	2.86	0.0	1.73
15	C_{2v}	5.44	2.86	1.0	1.76
16	C_2	5.41	2.86	0.0	1.78
17	C_1	6.33	2.89	1.0	1.80
18	C_{2v}	6.16	2.88	0.0	1.84
19	C_s	6.05	2.87	1.0	1.85
20	C_3	6.34	2.88	0.0	1.89

DFTB/GA search, but a PBE re-optimization of the T_d structure confirmed the T_d cluster to be about 0.09 eV lower in energy. The same is true for Ag_9–Ag_{16} where our structures agree more with those of the works of Gamboa et al. and Fournier, but Jin et al. demonstrated that the total-energy differences between several larger isomers are often smaller than 0.05 eV, for instance for Ag_9, Ag_{11}, Ag_{13}, and Ag_{14}, indicating a complicated and floppy potential energy surface and implying that small differences in the computational approach may have dramatic consequences for the predictions of the global total-energy-minima structures. Despite this, a linear fit of our calculated binding energies per atom versus $n^{-1/3}$, shown in Fig. 2 gives an estimate of 2.82 $\pm$ 0.04 eV/atom for the bulk cohesive energy of silver, which is in good agreement with the experimental determined value of 2.95 eV/atom [53].

Structure, Stability, and Magnetism of $Ag_{n-1}Rh$ and $AgRh_{n-1}$ Clusters

According to the PBE calculations for the AgRh dimer, the bond length equals 2.602 Å and the electronic ground-state structure is a triplet ($M = 3$). The bond is much longer than the distance calculated for Rh_2 (2.242 Å, $M = 5$) and close to the bond length for Ag_2 (2.625 Å, $M = 1$). A positive reaction enthalpy of 0.26 eV/atom for the reaction $Ag_2 + Rh_2 \rightarrow 2$ AgRh suggests that it is unlikely that a dimer of these two elements will be observed in experiment.

For the larger mixed clusters we show in Fig. 3 the ground-state structures and in Tables 6 and 7 a summary of all calculated properties for each cluster that was

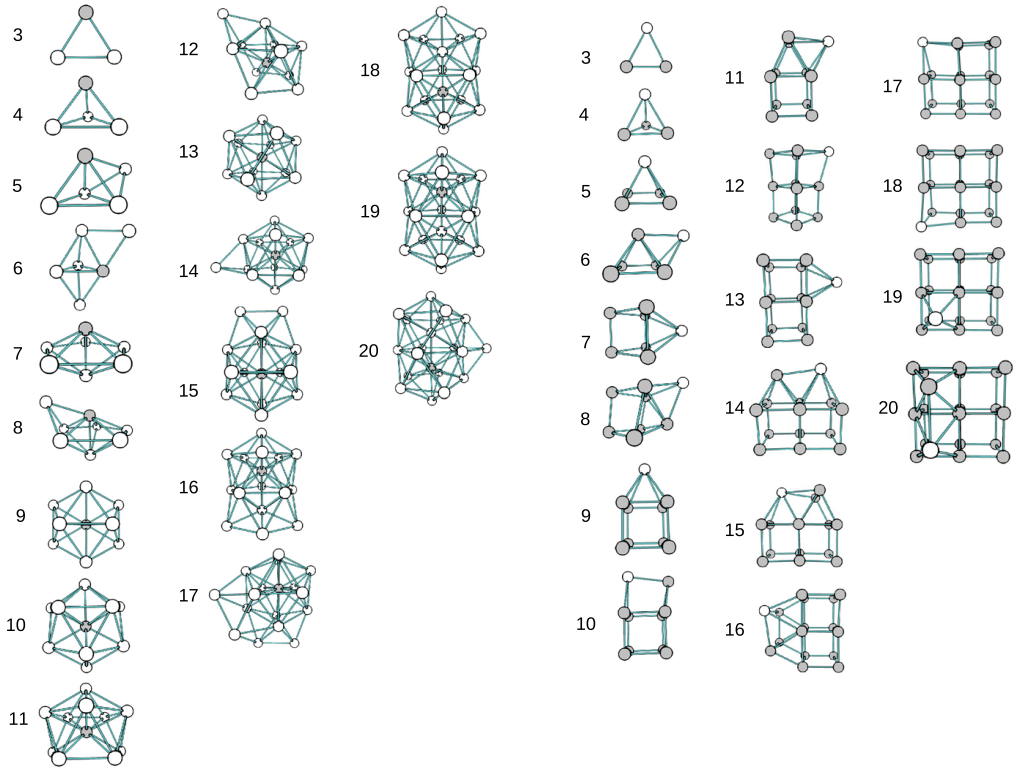

Fig. 3 The lowest minimum energy structures of $Ag_{n-1}Rh$ (*left*) and $AgRh_{n-1}$ (*right*) obtained in this study. The *white* (dark) spheres represent Ag (Rh) atoms

investigated in this work. In contrast to the pure silver clusters, replacing one silver atom by a rhodium atom leads to three-dimensional structures throughout the complete series. From the effective coordination numbers and average bond lengths it can be seen in Fig. 3 that rhodium occupies positions with a larger number of neighbouring atoms than silver does. This trend was also reported by Christensen et al. [58] who showed that a single impurity of rhodium has a high tendency to migrate away from the top-most atomic layer into the surface of Ag(111). Such a behaviour was also observed for other doped silver clusters, where an impurity transition metal atom tends to occupy higher-coordinated positions inside the cluster [30, 59, 60]. For a simple pairwise potential to capture at least the basic features of a chemical bond, namely repulsive and attractive interactions in dependency of a bonding distance r_{ij}, one can use the well-known Lennard–Jones (LJ) potential,

$$V_{ij}(r) = 4\epsilon_{ij}\left[\left(\frac{\sigma_{ij}}{r_{ij}}\right)^{12} - \left(\frac{\sigma_{ij}}{r_{ij}}\right)^{6}\right], \tag{16}$$

where ϵ describes the depth of the potential well and σ controls the equilibrium interatomic distance. By comparing the shape and the effective coordination number of our calculated Ag_{n-1} Rh_1 clusters with results from such a simple LJ potential with σ_{BB}/σ_{AA} = 1.185 (which equals the ratio of the atomic radii of Ag and Rh) [6]

Table 6 Point groups, PG, effective coordination numbers, ECN, average bond lengths, d_{av}, and total magnetic moments, m_t, of the lowest energy $Ag_{n-1}Rh$ cluster calculated with PBE and a DZP basis set. For ECN and d_{av}, we consider also the average values for the two types of atoms, separately

n	PG	ECN	d_{av}	ECN (Ag)	d_{av} (Ag) (Å)	ECN (Rh)	d_{av} (Rh) (Å)	m_t (μ_B)
2	$C_{\infty h}$	1.00	2.60	1.00	2.60	1.00	2.60	2.00
3	C_{2v}	1.96	2.69	1.93	2.71	2.00	2.65	1.00
4	C_{3v}	2.81	2.76	2.75	2.80	3.00	2.65	0.00
5	C_{2v}	3.51	2.79	3.39	2.82	3.98	2.71	1.00
6	C_s	3.59	2.78	3.31	2.80	4.99	2.71	0.00
7	C_{5v}	4.49	2.83	4.24	2.85	5.99	2.74	1.00
8	C_s	4.35	2.81	3.98	2.83	6.92	2.73	0.00
9	C_{2v}	4.99	2.84	4.61	2.86	7.97	2.73	1.00
10	C_{3v}	4.86	2.85	4.40	2.87	8.99	2.68	0.00
11	C_{2v}	5.49	2.86	5.04	2.87	9.99	2.75	1.00
12	C_s	5.48	2.87	5.08	2.88	9.89	2.73	0.00
13	C_s	5.89	2.87	5.47	2.88	10.90	2.77	1.00
14	C_{3v}	6.35	2.89	5.92	2.90	11.96	2.79	2.00
15	C_{2v}	6.35	2.89	5.96	2.90	11.70	2.79	1.00
16	C_s	6.43	2.89	6.09	2.90	11.62	2.79	0.00
17	C_2	6.51	2.89	6.20	2.90	11.59	2.79	1.00
18	C_{2v}	5.92	2.87	5.64	2.87	10.71	2.81	0.00
19	C_{5v}	6.96	2.91	6.71	2.92	11.48	2.79	1.00
20	Cs	6.94	2.91	6.70	2.91	11.34	2.79	0.00

and $\epsilon_{AB}/\epsilon_{AA} = 1.01$ we find a surprisingly similar trend, cf. Fig. 4, and conclude accordingly that these compact structures result mainly because of a size effect, although we add that a small stabilization of hetero-atomic versus homo-atomic interactions is required to get highly-coordinated Rh atoms at this cluster size and this Ag:Rh ratio.

To get information about the relative stabilities of the clusters the stability function $\Delta^2 E$ is a useful quantity. For the pure Ag_n clusters it is defined as

$$\Delta^2 E(n) = E(Ag_{n+1}) + E(Ag_{n-1}) - 2E(Ag_n) \tag{17}$$

and a similar expression for the pure Rh clusters. Here, $E(Ag_pRh_q)$ is the total energy of the Ag_pRh_q cluster. As reference for the discussion below on the mixed clusters, we show the stability function for the pure clusters in Fig. 5. In this figure, we recognize particularly stable clusters [i.e., clusters for which $\Delta^2 E(n)$ has maxima] for $n = 8$, 12, 18, and 19 for Rh_n and for $n = 6$, 8, and 12 for Ag_n.

For the mixed clusters, the stability function becomes

$$\Delta^2 E(n) = E(Ag_nRh) + E(Ag_{n-2}Rh) - 2E(Ag_{n-1}Rh) \tag{18}$$

Table 7 Point groups, PG, effective coordination numbers, ECN, average bond lengths, d_{av}, and total magnetic moments, m_t, of the lowest energy $AgRh_{n-1}$ clusters calculated with PBE and a DZP basis set. For ECN and d_{av}, we consider also the average values for the two types of atoms, separately

n	PG	ECN	d_{av} (Å)	ECN (Ag)	d_{av} (Ag) (Å)	ECN (Rh)	d_{av} (Rh) (Å)	m_t (μ_B)
2	$C_{\infty h}$	1.00	2.60	1.00	2.60	1.00	2.60	2.00
3	C_{2v}	1.73	2.52	2.00	2.72	1.59	2.42	3.00
4	C_{3v}	2.87	2.69	3.00	2.77	2.82	2.58	4.00
5	C_{4v}	2.86	2.53	4.00	2.79	2.58	2.47	3.00
6	C_s	3.48	2.60	3.00	2.81	3.57	2.55	8.00
7	C_{2v}	3.48	2.57	4.00	2.85	3.39	2.53	9.00
8	C_{3v}	3.62	2.57	3.00	2.81	3.71	2.54	10.00
9	C_{4v}	3.29	2.50	4.00	2.89	3.20	2.45	11.00
10	C_s	3.30	2.50	3.05	2.77	3.33	2.47	12.02
11	C_s	3.65	2.51	3.99	2.84	3.62	2.48	11.00
12	C_s	3.40	2.49	2.99	2.76	3.44	2.47	10.00
13	C_s	3.51	2.48	3.99	2.88	3.47	2.45	7.00
14	C_s	3.90	2.51	4.92	2.89	3.82	2.48	8.00
15	C_s	3.89	2.50	6.00	2.91	3.74	2.47	7.01
16	C_1	3.89	2.51	4.04	2.80	3.88	2.49	8.01
17	C_{2v}	3.67	2.49	4.01	2.85	3.65	2.47	9.03
18	C_s	3.63	2.47	3.07	2.72	3.67	2.45	6.00
19	C_s	3.78	2.48	3.98	2.88	3.77	2.46	3.07
20	C_1	4.04	2.50	4.94	2.88	3.99	2.48	4.00

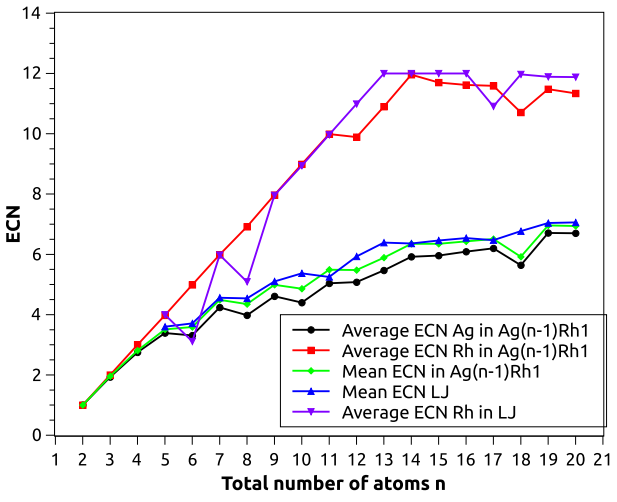

Fig. 4 ECN of doped $Ag_{n-1}Rh_1$ cluster obtained in this study compared to results for the LJ potential ($\sigma_{BB}/\sigma_{AA} = 1.185$, $\epsilon_{AB}/\epsilon_{AA} = 1.01$)

for the $Ag_{n-1}Rh$ clusters and a similar expression for the $AgRh_{n-1}$ clusters. Moreover, we may also define an excess energy, E_{ex}, that compares the total energy of a given cluster with that of the sum of fractions of the pure clusters of equal size,

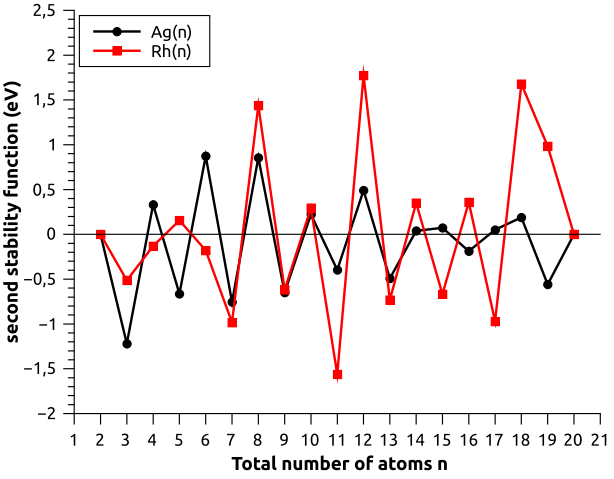

Fig. 5 The second stability function for Ag_n and Rh_n clusters as a function of the total number of atoms, n

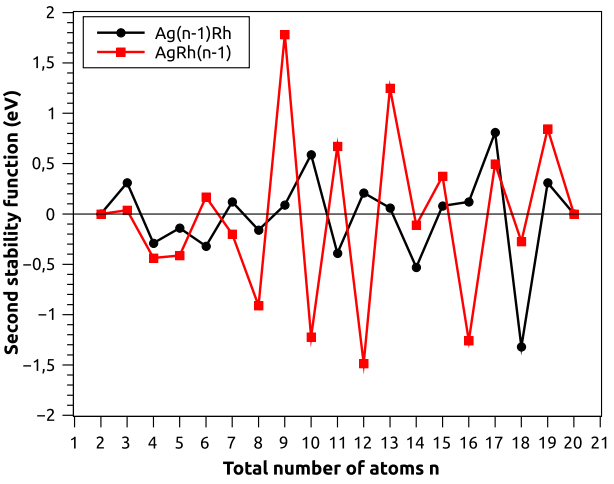

Fig. 6 The second stability function for $Ag_{n-1}Rh$ and $AgRh_{n-1}$ clusters as a function of the total number of atoms, n

$$E_{\mathrm{ex}} = E(\mathrm{Ag}_p\mathrm{Rh}_q) - \frac{p}{p+q}E(\mathrm{Ag}_{p+q}) - \frac{q}{p+q}E(\mathrm{Rh}_{p+q}). \tag{19}$$

$\Delta^2 E(n)$ for the mixed clusters is shown in Fig. 6. We identify an increased stability for Ag_9Rh and $Ag_{16}Rh$, and whereas the stability of the former could possibly be explained by a closed-shell-stability effect (18 electrons), it remains unclear why the latter is more stable compared to its neighbouring clusters. Also any other combination of elements in this series leading to a total of 18 valence electrons (or 8 if only the *s*-electrons are taken into account) are not particularly stable. The already mentioned preference of rhodium to form cube-based motifs is not interrupted by replacing a single rhodium atom by silver. The low coordination number of approximately 4 that can be seen in Fig. 7 for both elements over the whole series of clusters indicates (at least at the DFT-GGA level) their preference for non-compact structural motifs. However, from the plots of the excess energy and the stability function, Figs. 6 and 8, we see that from an energetic point of view, it is very beneficial to form a complete cube of rhodium without having a silver atom

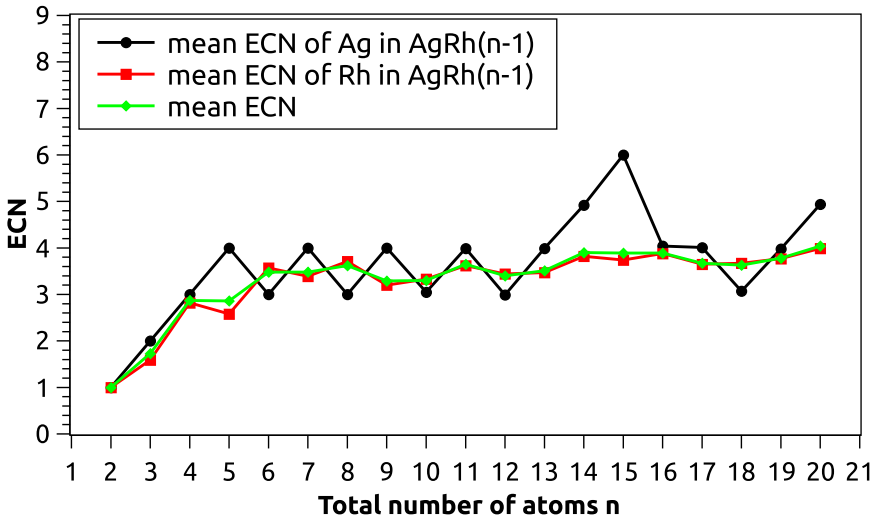

Fig. 7 Effective coordination numbers of Ag and Rh atoms in mixed $AgRh_n$ clusters

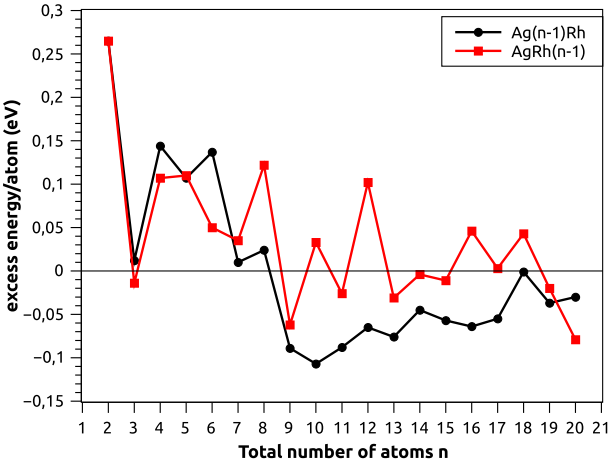

Fig. 8 The excess energy for $Ag_{n-1}Rh$ and $AgRh_{n-1}$ clusters as a function of the total number of atoms, n

occupying a corner. The same trend can be observed in the stability function of pure Rh_n. The particularly stable clusters compared with their neighbours in this series are accordingly $AgRh_8$, $AgRh_{10}$, $AgRh_{12}$, and $AgRh_{18}$. Only for the cases of undistorted structures we also observe a negative mixing energy that could imply that such clusters can be observed in experiment.

For the larger $Ag_{n-1}Rh$ clusters, E_{ex} is negative for all n, which suggests that for these clusters, an additional Rh atom added to a pure Ag cluster is energetically favourable. While there is no tendency towards mixing of Rh and Ag for clusters with up to a total of 8 atoms, we see a gain in energy compared to the pure clusters because of mixing for effective coordination numbers greater than 7. Rhodium has a binding energy per atom in the bulk nearly twice that of silver (5.75 eV/atom vs. 2.95 eV/atom) [53], so a larger coordination number for Rh, that is easiest realized for a core-shell-like structure, could be the driving force behind the negative mixing enthalpy in this system. For $AgRh_{n-1}$ the situation is less clear. However, for

instance the fact that there is a larger excess energy for $n = 12$ may also be related to the fact that the pure Rh cluster of the same size is particularly stable as can be seen from Fig. 5.

For the total magnetic moment m_t of the $Ag_{n-1}Rh$ clusters, cf. Fig. 9, we observe an odd-even oscillation between zero and one μ_B with an exception for the cluster with 14 atoms that has a total magnetic moment of 2 μ_B. It can also be seen that the local magnetic moment calculated from Mulliken population analysis on Rh decreases for an increase of its effective coordination number, a effect that was also observed in Ag_nFe clusters [30]. In contrast to the Ag_nFe cluster, systems for which an anti-ferro or ferro-magnetic behaviour for the silver host depends on the size of the cluster, we conclude that for the present systems the silver atoms contribute to the small ferro-magnetism and they carry a small net magnetic moment observable in the larger clusters. This can also be recognized from the spin densities for spin-up and spin-down electrons in $Ag_{10}Rh$ and $Ag_{13}Rh$ shown in Fig. 10 and 11 that show the de-localization of the magnetic moments over both elements in both spin channels whereas for the dimer in Fig. 12, the spin is largely localized to the rhodium atom. Janssens et al. [28] reported a quenching of the magnetic moment in cobalt doped silver clusters resulting in the loss of a net total magnetic moment for the studied clusters. However Harb et al. [61] observed for small Ag–Ni clusters

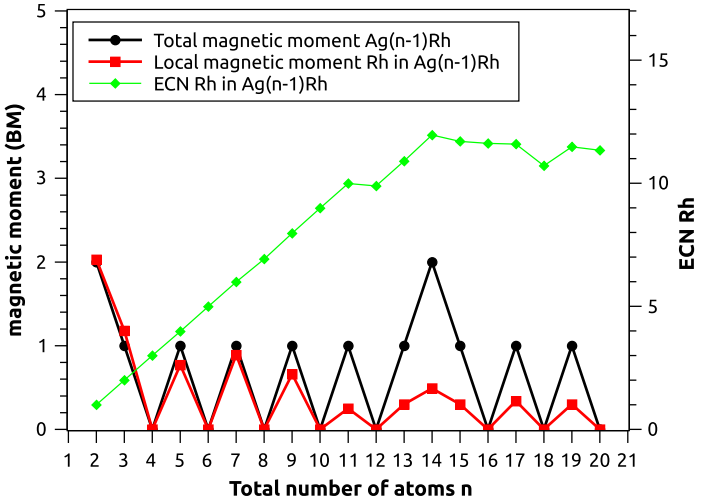

Fig. 9 Local magnetic moments and the influence of the effective coordination number on the total magnetic moment observed in $Ag_{n-1}Rh$ clusters

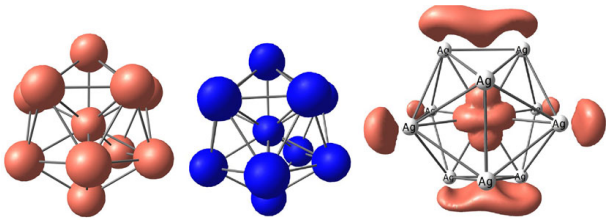

Fig. 10 Spin-up (*red*, *left*) and spin-down (*blue*, *middle*) densities and their difference (*red*, *right*) in $Ag_{10}Rh$ for an isovalue of 1.0 (left and middle) and 0.012 (right) (Color figure online)

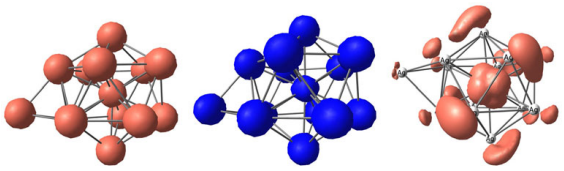

Fig. 11 Spin-up (*red*, *left*) and spin-down (*blue*, *middle*) (*left*) and their difference (*red*, *right*) in $Ag_{13}Rh$ for an isovalue of 1.0 (left and middle) and 0.012 (right) (Color figure online)

Fig. 12 Difference between spin-up and spin-down densities in AgRh for an isovalue of 0.02

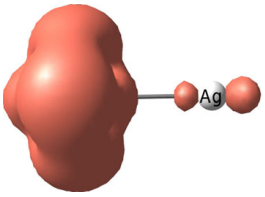

Fig. 13 The local magnetic moment on silver and the total magnetic moment in the $AgRh_{n-1}$ cluster compared with the total magnetic moment of the Rh_n cluster

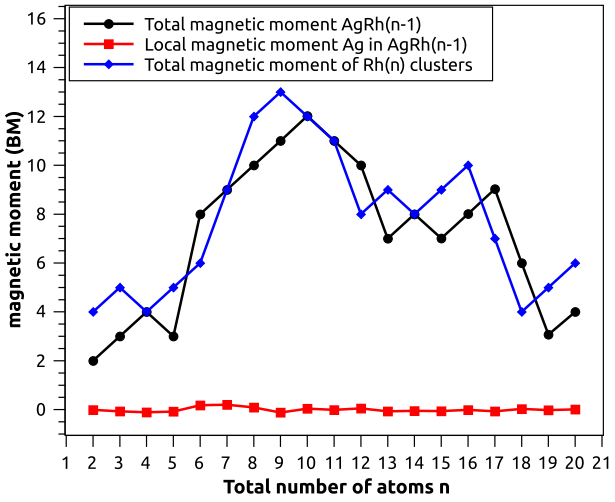

also a small magnetic moment located on the silver atoms and a larger contribution of the nickel atom to the calculated total magnetic moments.

In contrast to $Ag_{n-1}Rh$ where rhodium contributes most to the total magnetic moment, a single silver atom in $AgRh_{n-1}$ carries virtually no local magnetic moment as predicted by a Mulliken population analysis (cf. Fig. 13). An interesting case is that of $n = 8$ for which the pure Rh_8 cluster and the mixed $AgRh_7$ cluster have closely related structures. The substitution of a single rhodium by a silver atom in Rh_8 leads to a degenerate highest occupied molecular orbital (HOMO) resulting in a distortion of the cube after relaxation without changing its point group symmetry of C_{3v}. Therefore, we attribute this effect to be an accidental degeneracy and no Jahn–Teller based distortion of the cluster. Instead, the silver atom is simply too large to fit into the corner of the cube. A plot of the difference in the spin densities in $AgRh_7$ (Fig. 14) confirms the results from the Mulliken population analysis and shows the de-localization of the spin mainly over the rhodium atoms.

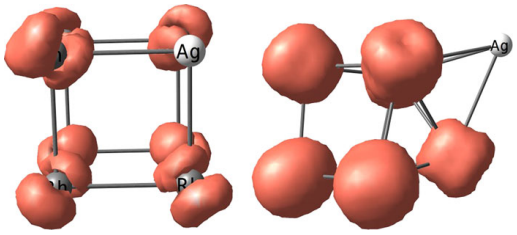

Fig. 14 Difference in the spin-densities before (*left*) and after structural relaxation (*right*) in $AgRh_7$ for an isovalue of 0.25

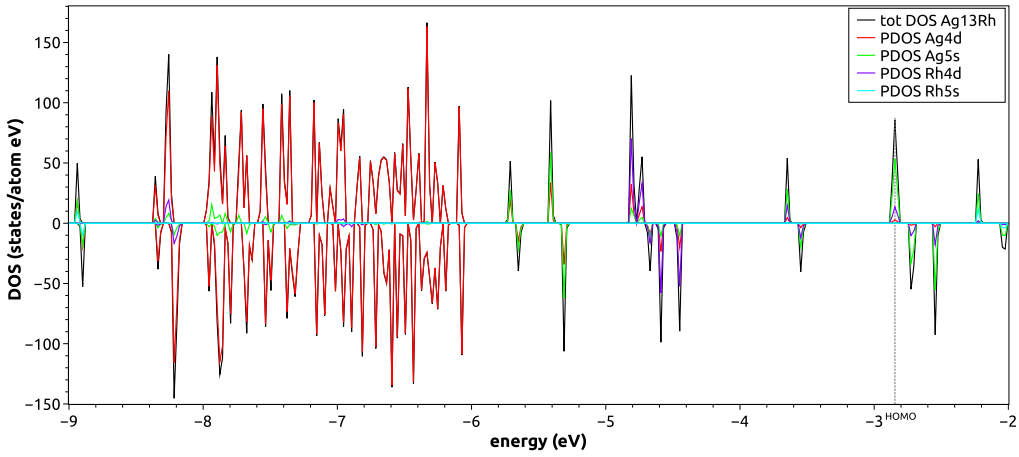

Fig. 15 The calculated density of states (DOS) and partial density of states (PDOS) for the cluster $Ag_{13}Rh$

Compared to the pure clusters we do not find any simple relationship between the observed magnetic moments and neither the position of the silver atom nor their effective coordination numbers as they are very similar in the pure Rh_n and mixed $AgRh_n$ clusters (cf. Fig. 13).

To get a more in-depth view of the influence of the doping of rhodium into a silver cluster we calculated the Density of States (DOS) and the partial density of states (PDOS) for the cluster with the largest observed total magnetic moment, $Ag_{13}Rh$. Additionally, we replaced the rhodium atom in the center of $Ag_{13}Rh$ by a silver atom without any further relaxation and calculated the DOS and PDOS to see the effect of the different atomic sizes on the total magnetic moment. We found that the non-relaxed cluster Ag_{14} has a total magnetic moment of 4 μ_B and that its magnetic properties do not alter when the structure is relaxed. This is in agreement with what was reported by Pereiro et al. [62] for the face-capped icosahedral Ag_{14} cluster. They attributed this enhanced magnetism to a charge transfer from the outer silver atoms to the inner one resulting in a small loss of the spin-up DOS at the Fermi-level of the inner atom. This leads to an enhancement of the magnetism of the outer atoms compared to the central silver atom and an overall increase in the total magnetic moment. Therefore, we also calculated the charge transfer via a Hirshfeld population analysis and found a contrary result to this assumption. In Ag_{14} the central atom carries almost no additional charge (partial charge: +0.08) while a rhodium atom in the core is found to have a partial negative charge of −0.24.

However the net magnetic moment was found to be smaller in the mixed cluster than for the pure Ag_{14} cluster despite a larger charge flow to the atom in the center. The DOS and PDOS in (cf. Fig. 15) shows that the HOMO is mainly formed from the 5*s* silver and the 4*d* rhodium orbitals with only minor contributions from the 4*d* levels of silver. Additionally, one can identify a relative shift of the spin-up and spin-down DOS in the HOMO and LUMO that results from the charge transfer to the central atom leading to a HOMO–LUMO spin-splitting that was essentially formed from the 5*s* orbitals of silver. This large contribution to the HOMO of the 5*s*-orbitals from silver is in agreement with the fact that silver contributes to the overall magnetic moment. However, it does not explain the smaller total magnetic moment of $Ag_{13}Rh$ compared to Ag_{14}.

Conclusions

In this work, we have studied the structural and magnetic properties of mixed $AgRh_{n-1}$ and $Ag_{n-1}Rh$ clusters and ompared with those of pure Ag_n and Rh_n clusters. The theoretical calculations were performed using density functional theory with the PBE functional for structures that were relaxed after a preceding global-optimization search using simpler total-energy methods. For the $Ag_{n-1}Rh$ series we found that Rh prefers to occupy higher-coordinated positions inside the clusters resulting in compact core-shell like structures that possess large similarities with the structural motifs of Lennard–Jones clusters. For smaller clusters, the magnetism is mainly localized to the the single rhodium atom and influenced by its effective coordination number, while in larger clusters, there is some ferro-magnetic contributions to the total magnetic moment from the silver atoms. In the $AgRh_{n-1}$ series we found a different behaviour, i.e., the clusters retain their cube-based motif as it can be seen from the effective coordination numbers, and it is energetically not beneficial for these systems to incorporate a silver atom into such a cube-like configuration of atoms. Mulliken population analyses suggest that there is no significant contribution from the single silver atom to the total magnetic moment in all of these clusters, even if one forces the atom to sit on the corner of an undistorted cube. However the relation between the observed total magnetic moments and the influence of a single silver atom remains unclear as we could not identify a clear correlation between geometric descriptors and the observed magnetic moment of a given $AgRh_{n-1}$ cluster.

Acknowledgments Stephan Kohaut would like to thank Prof. Dr. H. P. Beck for helpful discussions and N. Louis for computational support. Moreover, the authors would like to thank C3MSaar for providing the computational resources.

References

1. H. Rossler (1900). *Chem. Ztg*. **2**, 733.
2. R. W. Drier and H. L. Walker (1933). *Lond. Edinb. Dublin Phil. Mag. J. Sci.* **16**(104), 294 (1933).
3. A. A. Rudnitskii and A. N. Khotinskaya (1959). *Russ. J. Inorg. Chem*. **4**, 1053.
4. A. R. Miedema, P. F. de Châtel, and F. R. de Boer (1980). *Phys. B+C* **100**, 1.

5. A. Debski, R. Debski, and W. Gasior (2014). *Arch. Metal. Mater*. **59**, 1337.
6. J. C. Slater (1964). *J. Chem. Phys*. **41**, 3199.
7. K. Janghorban, J. Kirkaldy, and G. Weatherly (2001). *J. Phys. Condens. Matter* **13**(38), 8661.
8. K. Kusada, M. Yamauchi, H. Kobayashi, H. Kitagawa, and Y. Kubota (2010). *J. Am. Chem. Soc*. **132**, 15896.
9. S. Garcia, L. Zhang, G. W. Piburn, G. Henkelman, and S. M. Humphrey (2014). *ACS Nano* **8**, 11512.
10. D. H. Seo, H. Shin, K. Kang, H. Kim, and S. S. Han (2014). *J. Phys. Chem. Lett*. **5**, 1819.
11. A. Yang, O. Sakata, K. Kusada, T. Yayama, H. Yoshikawa, T. Ishimoto, M. Koyama, H. Kobayashi, and H. Kitagawa (2014). *Appl. Phys. Lett*. **105**, 153109.
12. M. Gracia-Pinilla, D. Ferrer, S. Mejia-Rosales, and E. Perez-Tijerina (2009). *Nanoscale Res. Lett*. **4**, 896.
13. M. N. Blom, D. Schooss, J. Stairs, and M.M. Kappes (2006). *J. Chem. Phys*. **124**, 244308..
14. D. Schooss, M. N. Blom, J. H. Parks, B. v. Issendorff, H. Haberland, and M. M. Kappes (2005). *Nano Lett*. **5**, 1972 (2005).
15. D. Reinhard, B. D. Hall, D. Ugarte, and R. Monot (1997). *Phys. Rev. B* **55**, 7868.
16. Y. C. Bae, H. Osanai, V. Kumar, and Y. Kawazoe (2004). *Phys. Rev. B* **70**, 195413.
17. Y. C. Bae, V. Kumar, H. Osanai, and Y. Kawazoe (2005). *Phys. Rev. B* **72**, 125427.
18. J. P. Chou, H. Y. T. Chen, C. R. Hsing, C. M. Chang, C. Cheng, C. M. Wei, *Phys. Rev. B* **80**, 165412 (2009).
19. M. J. Piotrowski, P. Piquini, and J. L. F. Da Silva (2010). *Phys. Rev. B* **81**, 155446.
20. J. P. Chou, C. R. Hsing, C. M. Wei, C. Cheng, C. M. Chang (2013). J. Phys. Condens. Matt. **25**, 125305.
21. J. L. F. Da Silva, M. J. Piotrowski, F. Aguilera-Granja (2012). *Phys. Rev. B* **86**, 125430.
22. M. R. Beltrán, F. Buendía Zamudio, V. Chauhan, P. Sen, H. Wang, Y. Ko, and K. Bowen (2013). *Eur. Phys. J. D*. **67**, 63.
23. D. J. Harding, P. Gruene, M. Haertelt, G. Meijer, A. Fielicke, S. M. Hamilton, W. S. Hopkins, S. R. Mackenzie, S. P. Neville, T. R. Walsh (2010). *J. Chem. Phys*. **133**, 214304.
24. D. J. Harding, T. R. Walsh, S. M. Hamilton, W. S. Hopkins, S. R. Mackenzie, P. Gruene, M. Haertelt, G. Meijer, and A. Fielicke (2010). *J. Chem. Phys*. **132**, 011101.
25. M. A. Mora, M. A. Mora–Ramrez, and M. F. Rubio-Arroyo (2010). *Int. J. Quant. Chem*. **110**, 2541.
26. M. Mora and M. Mora–Ramirez (2014). *J. Mol. Mod*. **20**, 2299.
27. E. Janssens, T. V. Hoof, N. Veldeman, S. Neukermans, M. Hou, P. Lievens (2006) (2006). *c Spectrometry* **252**(1), 38 (2006). doi:10.1016/j.ijms.2006.01.009. URL http://www.sciencedirect.com/science/article/pii/S1387380606000248
28. E. Janssens, S. Neukermans, H. M. T. Nguyen, M. T. Nguyen, and P. Lievens (2005). *Phys. Rev. Lett*. **94**, 113401. doi:10.1103/PhysRevLett.94.113401. URL http://link.aps.org/doi/10.1103/PhysRevLett.94.113401
29. X. J. Hou, E. Janssens, P. Lievens, and M. T. Nguyen (2006). *Chem. Phys*. **330**, 365.
30. R. Dong, X. Chen, H. Zhao, X. Wang, H. Shu, Z. Ding, and L. Wei (2011). *J. Phys. B* **44**, 035102.
31. E. Janssens, S. Neukermans, X. Wang, N. Veldeman, R. E. Silverans, and P. Lievens (2005). *Eur. Phys. J. D*. **34**(1–3), 23 (2005). doi:10.1140/epjd/e2005-00106-9. URl http://dx.doi.org/10.1140/epjd/e2005-00106-9
32. V. Bonačić-Koutecký, J. Burda, R. Mitrić, M. Ge, G. Zampella, and P. Fantucci (2002). *J. Chem. Phys*. **117**(7), 3120 (2002). doi:10.1063/1.1492800. URL http://scitation.aip.org/content/aip/journal/jcp/117/7/10.1063/1.1492800.
33. G. Rossi, R. Ferrando, A. Rapallo, A. Fortunelli, B. C. Curley, L. D. Lloyd, and R. L. Johnston (2005). *J. Chem. Phys*. **122**(19), 194309 (2005). doi:10.1063/1.1898224. URL http://scitation.aip.org/content/aip/journal/jcp/122/19/10.1063/1.1898224
34. R. Ismail and R. L. Johnston (2010). *Phys. Chem. Chem. Phys*. **12**, 8607. doi:10.1039/C004044D. URl http://dx.doi.org/10.1039/C004044D
35. M. Molayem, V.G. Grigoryan, and M. Springborg (2011). *J. Phys. Chem. C* **115**(45), 22148. doi:10.1021/jp2050417. URL http://dx.doi.org/10.1021/jp2050417.
36. M. Molayem, V. G. Grigoryan, and M. Springborg (2011). *J. Phys. Chem. C* **115**(15), 7179. doi:10.1021/jp1094678. URL http://dx.doi.org/10.1021/jp1094678
37. R. P. Gupta (1981). *Phys. Rev. B* **23**, 6265.
38. F. Cleri and V. Rosato (1993). *Phys. Rev. B* **48**, 22.

39. J.M. Soler, E. Artacho, J.D. Gale, A. Garcia, J. Junquera, P. Ordejon, and D. Sanchez-Portal (2002). *J. Phys. Condens. Matter* **14**, 2745.
40. D. M. Deaven and K. M. Ho (1995). *Phys. Rev. Lett*. **75**, 288.
41. R. L. Johnston (2003). *Dalton Trans*. 4193–4207.
42. G. Seifert, D. Porezag, and T. Frauenheim (1996). *Int. J. Quant. Chem*. **58**, 185.
43. P. Koskinen and V. Mkinen (2009). Comput. Mater. Sci. **47**, 237.
44. S. R. Bahn and K. W. Jacobsen (2002). Comput. Sci. Eng. **4**, 56.
45. G. G. Rondina and J. L. F. D. Silva (2013). J. Chem. Inf. Model. **53**, 2282.
46. R. Gehrke and K. Reuter (2009). *Phys. Rev. B* **79**, 085412.
47. M.D. Wolf and U. Landman (1998). *J. Phys. Chem. A* **102**, 6129.
48. D. Porezag, T. Frauenheim, T. Köhler, G. Seifert, and R. Kaschner (1995). *Phys. Rev. B* **51**, 12947. doi:10.1103/PhysRevB.51.12947. URL http://link.aps.org/doi/10.1103/PhysRevB.51.12947
49. V. Rosato, M. Guillope, and B. Legrand (1989). *Philos. Mag. A* **59**, 321.
50. M. Jamal, S. J. Asadabadi, I. Ahmad, H. A. R. Aliabad (2014). Comput. Mater. Sci. **95**, 592.
51. M. Jamal, S. J. Asadabadi, I. Ahmad, H. A. R. Aliabad (2013). *J. At. Mol. Sci*. **4**, 235.
52. F. Aguilera-Granja, J. L. Rodríguez-López, K. Michaelian, E. O. Berlanga-Ramírez, A. Vega (2002). *Phys. Rev. B* **66**, 224410.
53. C. Kittel, *Introduction to Solid State Physics 8th Edition* (Wiley, Hoboken, 2005).
54. R. Hoppe and Z. Kristallogr (1979). **150**, 224410.
55. G.U. Gamboa, A.C. Reber, and S.N. Khanna (2013). *New J. Chem*. **37**, 39283935.
56. R. Fournier (2001). *J. Chem. Phys*. **115**, 21652177.
57. Y. Jin, Y. Tian, X. Kuang, C. Zhang, C. Lu, J. Wang, J. Lv, L. Ding, and M. Ju (2015). *J. Phys. Chem. A* **119**, 6738.
58. A. Christensen, A. V. Ruban, P. Stoltze, K. W. Jacobsen, H. L. Skriver, J. K. Nørskov, and F. Besenbacher (1997). *Phys. Rev. B* **56**, 5822.
59. E. Janssens, X. J. Hou, M. T. Nguyen, and P. Lievens (2006). *J. Chem. Phys*. **124**(18), 184319 (2006). doi:10.1063/1.2191495.
60. W. Li, and F. Chen (2013). *J. Nanopart. Res*. **15**, 1809.
61. M. Harb, F. Rabilloud, and D. Simon (2007). *J. Phys. Chem. A* **111**(32), 7726. doi:10.1021/jp072207l. URL http://dx.doi.org/10.1021/jp072207l. PMID: 17637046
62. M. Pereiro, D. Baldomir, and J. E. Arias, *Phys. Rev. A* **75**, 063204. doi:10.1103/PhysRevA.75.063204. URL http://link.aps.org/doi/10.1103/PhysRevA.75.063204.

14 Summary

In this work, we have studied the growth of several cluster systems including monometallic, bimetallic and mixed semiconductor clusters with our genetic algorithm coupled to the density functional tight-binding method followed by a re-optimization with accurate density functional theory methods with GGA(PBE) functionals. A new growth pattern for small to medium sized cadmium clusters with sizes up to 60 atoms was proposed in our work and we showed that they are not disordered Marks decahedra as earlier assumed by other authors. Up to a size of around 36 atoms the growth was dominated by a process in which the atoms are added to a smaller core that was built around two fused tricapped-trigonal prisms. The first atomic shell was observed to be complete at the highly symmetrical Cd_{34} cluster with point group T_d and further addition of atoms leads to clusters with relatively low symmetry but overall spherical shape. By analyzing the results of a bond-angle analysis on all clusters we concluded that the inner atoms in the core are arranged similarly to what is found in the hcp bulk structure with a maximum number of bulk-like atoms found in the already mention Cd_{34} cluster. Although we observed that the next shell was completed at a size of 44 atoms, we found that further growth does not proceed in exactly the same way. The shell-like growth continued up to a cluster with 52 atoms and then the earlier proposed distorted Marks decahedra could become important as candidates for the global total-energy minimum. Clusters with 53 atoms and an overall decahedral motif became energetically comparable with those obtained in our study and it may be difficult to uniquely identify the correct lowest total-energy structure state in an experiment. For sizes greater than 54 atoms we identified clusters with an oThe trend towards the formation of a core-shell system could be identified from an analysis of the average effective coordination numbers and the bond orders in the mixed structures, especially in almost pure clusters. For clusters with about equal ratios of both elements we found a preference for disorderly mixed or onion-like structures. Finally, we could not prove that the electronic properties in small to medium sized mixed Si m Ge n clusters are the result from a single structural property or the composition alone. Thus, we conclude that the electronic properties depend in a non-trivial way on the shape, composition and structural properties (e.g. coordination numbers and bond lengths).verall low symmetry but a tendency to maximize the number of hcp-like atoms in the core of the clusters as predicted by the bond-angle analysis. The relative stabilities of the obtained clusters were compared with experimental abundance patterns from mass spectroscopic measurements and we concluded that the stability of certain clusters is the result of strong electron shell closing effects and a beneficial geometric packing that leads to highly symmetric clusters at certain sizes. The chemical bonds of these clusters as found from an interpretation

of the partial density of states are dominated by s and p contributions as in bulk hcp cadmium and d-s hybridization seemed to be of minor importance.

In the second system, mixed Si_mGe_n clusters with $m + n \leq 30$, we showed that the stability correlates with the shape of the clusters with the most stable structures being found for prolate clusters with an average content of 32% silicon. From a comparison of all obtained clusters with the pure clusters of equal size through a calculation of a similarity index we found that the larger mixed clusters are neither similar to the corresponding pure clusters of silicon nor to the motifs found for pure germanium clusters, especially if the silicon to germanium ratios were close to one. However we could show that silicon is the shape dominating element in clusters with larger Si contents. The trend towards the formation of a core-shell system could be identified from an analysis of the average effective coordination numbers and the bond orders in the mixed structures, especially in almost pure clusters. For clusters with about equal ratios of both elements we found a preference for disorderly mixed or onion-like structures. Finally, we could not prove that the electronic properties in small to medium sized mixed Si_mGe_n clusters are the result from a single structural property or the composition alone. Thus, we conclude that the electronic properties depend in a non-trivial way on the shape, composition and structural properties (e.g. coordination numbers and bond lengths).

Singly doped silver and rhodium clusters with up to 20 atoms where the last cluster systems that were studied in this work. We investigated the structural and magnetic properties of mixed $AgRh_{n-1}$ and $Ag_{n-1}Rh$ clusters and compared them with those of pure Ag_n and Rh_n clusters. In clusters of the series $Ag_{n-1}Rh$ series we found that Rh prefers to occupy higher-coordinated positions inside the cores of the clusters resulting in compact core-shell like structures that possessed large similarities with the structural motifs known for Lennard-Jones clusters. The size difference between the silver and rhodium atoms thereby seemed to be the driving force for the formation of icosahedral core-shell clusters. The net magnetic moments in smaller $Ag_{n-1}Rh$ clusters are mainly localized to the single rhodium atom in the core and it was found that they depend on its effective coordination number. In larger clusters, however, we proved that there are some ferro-magnetic contributions to the total net magnetic moment from the silver atoms. The clusters of the series AgR_{n-1} showed a different behavior, i.e., the clusters retain their cube-based motif and it is energetically not beneficial for these systems that a silver atom sits at a position that was formerly occupied by a rhodium atom. This is mainly due to strain effects, silver does simply not fit into the rhodium positions and therefore the silver atoms migrate to the surface of the clusters. Mulliken population analyses suggested that there is no significant contribution from the single silver atom to the total magnetic moment in all of these clusters, even if the atom was forced to sit at a rhodium position

(e.g. on the corner of an undistorted cube). However the relation between the observed total magnetic moments and the influence of a single silver atom remains unclear and we were not able to identify any correlations between geometric descriptors and observed magnetic moments in $AgRh_{n-1}$ clusters.

List of Publications

1. S. Kohaut and M. Springborg: *"Growth patterns and structural motifs of cadmium clusters with up to 60 atoms: disordered or not?"*, Phys. Chem. Chem. Phys. (2016) **18**:28524

2. S. Kohaut, P. Thiel, M. Springborg: *"Growth patterns, shapes, and electronic properties of mixed Si_mGe_n clusters with $n + m = 30$"* Computational & Theoretical Chemistry (2016), Accepted

3. S. Kohaut and M. Springborg:*"Structural, Energetic, and Magnetic Properties of Ag_{n-m} Rh_m and Ag_mRh_{n-m} Clusters with $n \leq 20$ and $m = 0, 1$"*, J. Clust. Sci. (2016) **27**:913933

4. H.P. Beck and S. Kohaut: *"A DFT study on the correlation between topology and Bader charges: Part II, effects of compression and dilatation of V2O5"*, Solid State Sciences (2015) **43**:1-8

5. M. Springborg, S. Kohaut, Y. Dong, K. Huwig:*"Mixed Si-Ge clusters, solar-energy harvesting, and inverse-design methods"*, Computational & Theoretical Chemistry (2016), Accepted

6. N. Kunkel, A.D. Sontakke, S. Kohaut, B. Viana, P. Dorenbos: *"Thermally Stimulated Luminescence and First-Principle Study of Defect Configurations in the Perovskite-Type Hydrides $LiMH_3$:Eu^{2+} (M = Sr, Ba) and the Corresponding Deuterides"*, J. Phys. Chem. C (2016), Accepted

7. S.Kohaut and M. Springborg: *"An unbiased global optimization of nano-alloyed Pd_mRh_n clusters with $n + m \leq 20$"*, in preparation

8. S.Kohaut, G. Lefevre and M. Springborg: *"Structure, stability and magnetism of mixed Pt_mAu_n clusters with $n + m \leq 20$"*, in preparation